Biological and Biomechanical Effects of Direct Perturbation of Tissue Structure in the Cirrhotic Liver

by

Ben D. Leaker
BASc, University of Toronto (2017)

Submitted to the Harvard-MIT Program in Health Sciences and Technology, in partial fulfillment of the requirements for the degree of

Doctor of Philosophy in Medical Engineering and Medical Physics

at the

Massachusetts Institute of Technology

February 2024

Authored by: _____

Ben D. Leaker
Harvard-MIT Program in Health Sciences and Technology
January 15th, 2024

Certified by: _____

R. Rox Anderson, MD
Professor of Dermatology, Harvard Medical School
Thesis Supervisor

Accepted by: _____

Collin M. Stultz, MD, PhD
Director, Harvard-MIT Program in Health Sciences and Technology
Nina T. and Robert H. Rubin Professor in Medical Engineering and Science
Professor of Electrical Engineering and Computer Science

Biological and Biomechanical Effects of Direct Perturbation of Tissue Structure in the Cirrhotic Liver

by

Ben D. Leaker

Submitted to the Harvard-MIT Program in Health Sciences and Technology on January 15th, 2024 in partial fulfillment of the requirements for the degree of Doctor of Philosophy in Medical Engineering and Medical Physics

Abstract

Cirrhosis is the scarring that occurs as the common final stage of chronic liver diseases. Although our understanding of the disease has improved substantially over the past several decades, there has been little progress in the treatment of cirrhosis. Drug development has been unsuccessful largely because it is difficult to reverse profound structural changes with a pharmaceutical approach. Consequently, there is a need for innovative new approaches to the treatment of cirrhosis that can exert greater influence on tissue architecture. This thesis explores three innovative treatment strategies, each aimed at directly perturbing tissue structure through a distinct mechanism.

First, we investigate microinjury perturbation using a fractional laser. This work revealed an exacerbated injury response in the cirrhotic liver. Through investigating the mechanism of this response, we revealed a novel ischemic susceptibility related to the microvascular architecture.

We then investigate lytic perturbation through interstitial infusion of collagenase clostridium histolyticum and mechanical perturbation through shockwave disruption. With both techniques we were able to show significant reductions in fibrosis with minimal toxicity.

Direct perturbation methods have been underexplored in the search for a treatment for cirrhosis and fibrosis of internal organs in general. Our findings highlight the potential of such an approach and may pave the way for new therapeutic options.

Thesis Supervisor: R. Rox Anderson, MD
Title: Professor of Dermatology, Harvard Medical School

Acknowledgements

I am grateful for the contributions of so many people who made this work possible.

First, I would like to thank my supervisor Dr. Rox Anderson. I love telling people the story of the first time we met. Rox was 45min late for a 30min meeting (he was treating a child with burn wounds, so he had a pretty good excuse). We ended up talking for over an hour, first about my general interests and then about random questions like 'why can some lizards regenerate a limb but still scar from a myocardial infarction'. I knew from that meeting that this was exactly the kind of person I wanted to do science with. Thank you for your guidance and wisdom.

I also would like to thank everyone on my thesis committee: Dr. Dan Anderson, Dr. Yury Popov, and Dr. Ken Tanabe. As a graduate student working on a liver project in a lab that mostly specializes in skin, your guidance has been invaluable. Thank you for all your advice.

I also need to thank Dr. Josh Tam, who I have talked to about this work almost every week since we started. Josh is the first person I would go to with any result or problem, and he has fundamentally shaped this thesis. This work could not have been done without him.

Thank you to all of the Anderson Lab members who contributed many things big and small over the years, particularly Dr. Ying Wang, Bill Farinelli, Dr. Nashwa Cheema, Katherine Stalnaker, Carina Thomas, Namrata Ghag, Dr. Brandon Law, and Emma Wise. Thank you also to Dr. Jie Zhao, Jermaine Henderson, Neema Kumar, and Lingxian Wu of the Wellman Photopathology Core.

Thank you to Dr. Mozhdeh Sojoodi, who taught me pretty much all my in vivo research skills, and to Dr. Christiane Fuchs, who did the same for in vitro. Thank you to Dr. Yongtao Wang for his assistance particularly in the precision-cut liver slice work.

Thank you also to Dr. Bryan Fuchs, who was the first person I spoke to outside of my lab about studying cirrhosis. His expertise with liver research greatly shaped the beginning of my thesis work. He also connected me to Mozhdeh, which on its own is a huge contribution.

Thank you to Dr. Chris Capelli and George Frangineas of AbbVie for helping us set up the shockwave project and for their contributions to the data collection and experimental design of that work. Thank you also to Jed Palmer and Aidan Curry of Emphysys for their assistance in running the shockwave device.

I am fortunate to have had many research mentors before starting my PhD who shaped me as a scientist and encouraged me to pursue this path. Thank you to Dr. Yue Li, Prof. Hani Naguib, and Dr. Tilak Dutta. A special thank you also to Gordon Wong for making me think research is fun.

Finally, thank you to my family and friends. I couldn't have done this without your support.

Contents

List of Figures

List of Tables

Chapter 1

Introduction

1.1 Cirrhosis

Cirrhosis refers to the structural abnormalities that arise as the common final stage of chronic liver diseases such as viral hepatitis, alcoholic liver disease, and metabolic associated fatty liver disease (formerly non-alcoholic steatohepatitis, NASH). It is an often underappreciated global health concern. Cirrhosis ranks 13th in disability-adjusted life years (a common measure of disease burden) – ahead of malaria, lung cancer, breast cancer, drug use, and dementia[1] (**Figure 1-1**) – and accounts for over 1 million deaths per year, more than 2% of the global total[2]. The only current treatment option is liver transplant, which is severely limited by short supply of donors and stringent exclusion criteria – in the US, the annual number of liver transplants across all indications would

account for only 5% of patients with decompensated cirrhosis based on 2014 data[3] – as well as the need for potentially lifelong immunosuppression.

Cirrhosis develops as a result of persistent injury over many years. The injury can take a variety of forms, such as an immune response to a virus or ingesting a hepatotoxin. Frequent injury causes death of hepatocytes (the cell responsible for the bulk of the liver's synthetic and metabolic functions) and collapse of the extracellular matrix they had occupied[4]. This causes hepatic stellate cells to adopt a myofibroblast phenotype[4]. These cells remodel the collapsed matrix into dense bands of collagen called fibrous septa that segment the liver into nodules up to several millimeters in diameter[4]. This process causes gradual increase in tissue stiffness, a metric which is often used clinically to estimate disease stage[5]. New blood vessels also form within the septa that shunt blood past the liver capillaries, causing poor oxygenation of hepatocytes[6, 7]. This is accompanied and exacerbated by defenestration of the specialized liver capillaries called sinusoids[6, 8]. Advanced cirrhosis can result in liver failure as well as a wide range of other complications, including ascites, jaundice, coagulopathy, portal hypertension, variceal bleeding, and hepatocellular carcinoma[7, 9].

It is well established that the liver is capable of spontaneous recovery if the underlying injury is resolved early enough[10, 11]. For this reason, many researchers and pharmaceutical companies are developing drugs to cure specific diseases or halt progression before substantial damage has occurred. While this is clearly important work, 40% of cases are asymptomatic until cirrhosis has developed[4] so many patients will not be identified early enough for these treatments to be effective. As such, there is also a significant need for treatments targeted to patients with established cirrhosis.

The exact cause of the functional deficiencies associated with cirrhosis is difficult to identify, but there is evidence suggesting a direct link to the abnormal structure. Many

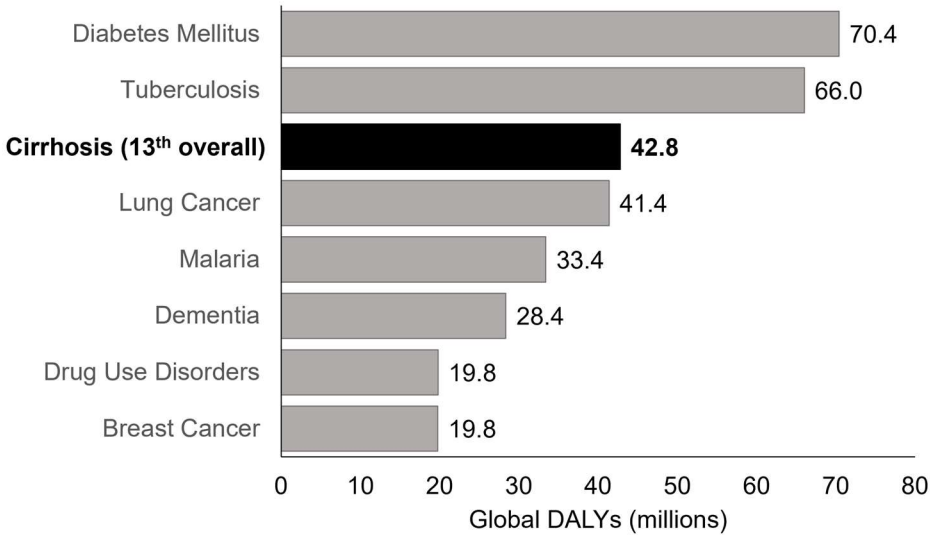

Figure 1-1: Global Disease Burden of Cirrhosis. Select list of diseases ranked by disability-adjusted life years (DALYs), a common measure of disease burden. Cirrhosis is 13th overall. Data from World Health Organization Global Health Estimates 2020: Disease burden by Cause, Age, Sex by Country and by Region, 2000-2019[1].

liver fibrosis patients will not experience any symptoms until a late stage of the disease[4], after severe structural alterations have accrued. Hepatocytes in a stiff environment exhibit suppressed albumin production[12], downregulation of cytochrome p450[13] and HNF4α[14] (two markers of hepatocyte differentiation and liver-specific function), as well as changes in a range of genes associated with normal epithelial function[15]. Hepatocyte senescence is also thought to contribute to liver dysfunction in cirrhosis[16]. The cause of this senescence is typically attributed to repetitive injury[17]; however, there is some evidence in age-associated senescence research demonstrating a link with tissue stiffness[18, 19], suggesting the mechanical environment may also play a role in hepatocyte senescence.

Although our understanding of the disease has improved substantially over the past several decades, there has been little progress in the treatment of cirrhosis. Overall mortality has improved slightly relative to the total population but this has been attributed to better management of key risk factors, such as alcohol use, rather than any substantial improvements in treatment[3]. Drug development for fully established cirrhosis has thus far been unsuccessful in large part because it is difficult to significantly change tissue architecture with a pharmaceutical approach. Consequently, there is a need for innovative new approaches to the treatment of cirrhosis capable of exerting greater influence on tissue architecture.

1.2 Thesis Approach

Fibrotic disorders can occur anywhere in the body, but skin scars have the unique property of being easily accessible. As a result, the history of development of skin scar therapies has focused on more direct intervention rather than drugs, as is the case for fibrosis of other organs. Examples of this include z-plasty[20], where incisions are made along tension lines in the scar, and complete excision of the wound for replacement with

an autograft[21]. This philosophy of directly perturbing the scar has been applied to the development of a variety of treatments for skin scars that directly and immediately alter tissue structure. This is a fundamentally different approach from the typical drug development philosophy that dominates research into therapies for internal organs.

The approach of this thesis was based on the idea that the direct perturbation approach favoured in dermatology has been under-investigated in the search for treatments for cirrhosis. Indeed, it has been under-investigated for fibrosis throughout the body and demonstrating efficacy in cirrhosis – a disease with massive burden and limited pharmaceutical progress – may open the door for similar applications in other organs.

Three novel methods are discussed in this thesis, each aimed at directly perturbing tissue structure through a different mechanism.

First, we investigate microinjury perturbation. This approach uses a fractional laser to create an array of very small injuries in the tissue that stimulate remodeling. Microinjury treatment has shown great success for inducing remodeling of skin scars and is now commonplace in dermatology clinics. We will discuss differences in how this treatment is tolerated in the healthy and cirrhotic liver, with a particular focus on the influence of the cirrhotic microvasculature.

Next, we investigate lytic perturbation using interstitial infusion of purified collagenase clostridium histolyticum (CCH). This mixture of enzymes has been used as a potent tool for tissue degradation for many years. Recently however, it was shown that direct injection of a purified version can effectively and rapidly degrade a dense, highly crosslinked collagen cord that causes a fibrotic condition called Dupuytren's Contracture. We will discuss the distribution of a macromolecule delivered via interstitial infusion, toxicity from the enzyme, and efficacy as a treatment for cirrhosis.

Finally, we investigate mechanical perturbation from extracorporeal shockwave treatment. Shockwaves have been used to cause non-invasive mechanical disruption for many years, most notably in the destruction of kidney stones. Research has also shown that shockwave disruption possesses a mechanical selectivity, whereby more stiff substrates are more susceptible to disruption. This is a very attractive property in a prospective cirrhosis treatment, as the stiff fibrous septa encircle the remaining functional tissue. Because of this property, shockwave treatment may be able to disrupt the septa while leaving the parenchyma unharmed. As part of this study, we also worked on validating an ex vivo tissue culture model that will support higher throughput testing of structural perturbation therapies like the ones presented here. We will discuss toxicity and efficacy of shockwave treatment along with the potential clinical implications of our findings.

The research presented in this thesis has yielded promising results; nonetheless, we acknowledge that these treatments are still in an evolving phase and are far from providing a definitive solution. The following chapters will discuss the next steps in development that will be necessary to eventually translate into meaningful clinical advancements. However, one of the main goals of this work is to showcase the viability of a more direct approach in addressing liver cirrhosis. We hope that our findings will encourage more researchers to consider similar avenues of investigation as we continue the search for a treatment.

Parts of this thesis have been adapted from the following publications:

- Leaker BD, Fuchs C, Tam J. When Wounds Are Good for You: The Regenerative Capacity of Fractional Resurfacing and Potential Utility in Chronic Wound Prevention. Adv Wound Care (New Rochelle). 2019 Dec 1;8(12):679-691.

- Leaker BD, Sojoodi M, Tanabe KK, Popov YV, Tam J, Anderson RR. Increased susceptibility to ischemia causes exacerbated response to microinjuries in the cirrhotic liver. FASEBJ. (In revision). https://www.biorxiv.org/content/10.1101/ 2023.07.18.549420v1
- Leaker BD, Fuchs C, Wise E, Tam J, Anderson RR. Interstitial infusion of purified collagenase clostridium histolyticum in the cirrhotic liver causes rapid reduction in fibrosis with minimal liver injury. (In preparation)
- Leaker BD*, Wang Y*, Tam J, Anderson RR. Analysis of culture and RNA isolation methods for precision-cut liver slices from cirrhotic rats. Sci Rep. (Under review)

Related publications not included in this thesis:

- Wang Y*, Leaker BD*, Qiao G*, Sojoodi M, Eissa IR, Epstein ET, Eddy J, Dimowo O, Mullen AC, Lauer GM, Chung RT, Qadan M, Lanuti M, Fuchs BC, Tanabe KK. Precision-cut liver slices as an ex vivo model to evaluate antifibrotic therapies for liver fibrosis and cirrhosis. (In preparation)

Chapter 2

Microinjury Perturbation via Fractional Laser Ablation

2.1 Introduction

One of the most recent and effective methods of scar treatment in Dermatology is based on microinjury regeneration. While large injuries cause skin to heal by scarring, sufficiently small injuries (nominally <500μm in diameter) induce a wound healing response that leads to healing with normal tissue[22, 23]. This property is maintained even in fibrotic skin, and it was found that creating dense patterns of microinjuries in a skin scar using a tool called a fractional laser leads to dramatic improvements and normalization of tissue structure and function. This includes a few clinical reports of the return of

complex structures such as hair follicles and sweat glands, which are typically permanently lost in skin scars [22, 24, 25]. Microinjury ablation has shown remarkable clinical efficacy, with particularly dramatic results for scars over joints where the stiff, contracted tissue had restricted movement. Tissue stiffness decreases within days of treatment, as shown by substantial improvements in range of motion[26]. There is then continued tissue remodeling lasting several months that results in significant improvements in appearance, texture, pliability, pain, and pruritis[22, 26-29]. Histology shows neovascularization, reduced density of collagen, and a more organized fibril arrangement [29].

In the skin, the fractional laser enables macrophages and neutrophils to infiltrate the densely packed, highly cross-linked collagen fibrils that make scar tissue resistant to degradation[30, 31]. This induces expression of a range of MMPs that cause a potent, short-term matrix remodeling phase[32-34], leading to a significant reduction in scar stiffness within a few days of treatment[35]. As a result, the critical positive feedback loop between fibrosis and tissue stiffness is disrupted[31], enabling long-term remodeling towards normal tissue. This will be discussed in greater detail in section 2.2 Mechanisms of Laser Resurfacing & Microinjury Regeneration.

Microinjury ablation is a unique concept that relies on the creation of finely controlled injuries to treat a condition caused by uncontrolled injury. It is unknown how other tissues respond to microinjury ablation. If the treatment can stimulate remodeling of the cirrhotic septa, it may be a powerful new tool in the management of chronic liver disease. It is first necessary to understand how the liver responds to microinjuries. In this study, we aimed to characterize the tissue response to microinjury ablation in the healthy and cirrhotic liver. We then investigated the underlying cause for the differences in response to ablation, with a particular focus on the influence of the liver microvascular architecture.

2.1.1 Microinjuries in Dermatology

Outside of early gestation, human skin wounds mostly heal by scarring, which is characterized by disorganized microanatomy, absence of dermal appendages, and myriad other structural and functional defects[36]. There is one notable exception to this generalization: small (nominally 500 μm or less in diameter) wounds can regenerate completely, without scarring, even when total tissue loss is substantial – up to 50% of skin tissue within a treatment area can be removed in the form of microinjuries, and the subsequent remodeling process can not only replace the tissue normally but in some cases actually lead to better quality skin (**Figure 2-1**)[37-39]. Various clinical modalities have been developed to take advantage of this phenomenon (outlined in **Figure 2-2**), whereby arrays of microinjuries are produced by thermal (lasers and radiofrequency) or mechanical (microneedling) means, to induce tissue remodeling via a process known as fractional resurfacing. Two types of laser treatments are commonly used. Ablative fractional laser (AFL) treatment vaporizes a small column of tissue (**Figure 2-2 A**), while non-ablative fractional laser (NAFL) treatment thermally denatures a column of tissue without vaporizing (**Figure 2-2 B**). The significance of this difference in the mechanism of fractional resurfacing remains unclear.

Fractional resurfacing is a popular procedure to "rejuvenate" skin by reducing the visible signs of photoaging, such as rhytids and dyschromia[39], but beyond cosmetic enhancements, the treatment also leads to broad improvements in skin quality, including increased dermal thickness, synthesis and remodeling of extracellular matrix (ECM) components, reduced atypical keratinocytes, increased vascularity, improved rete ridge formation, reduced senescent fibroblast population, and restoration of proper response to ultraviolet light[40-42]. Of greatest interest for this work, fractional resurfacing also has a unique ability to induce dramatic and lasting functional improvements in skin scars, including normalizing scar thickness, reducing pain and pruritus (suggesting resolution

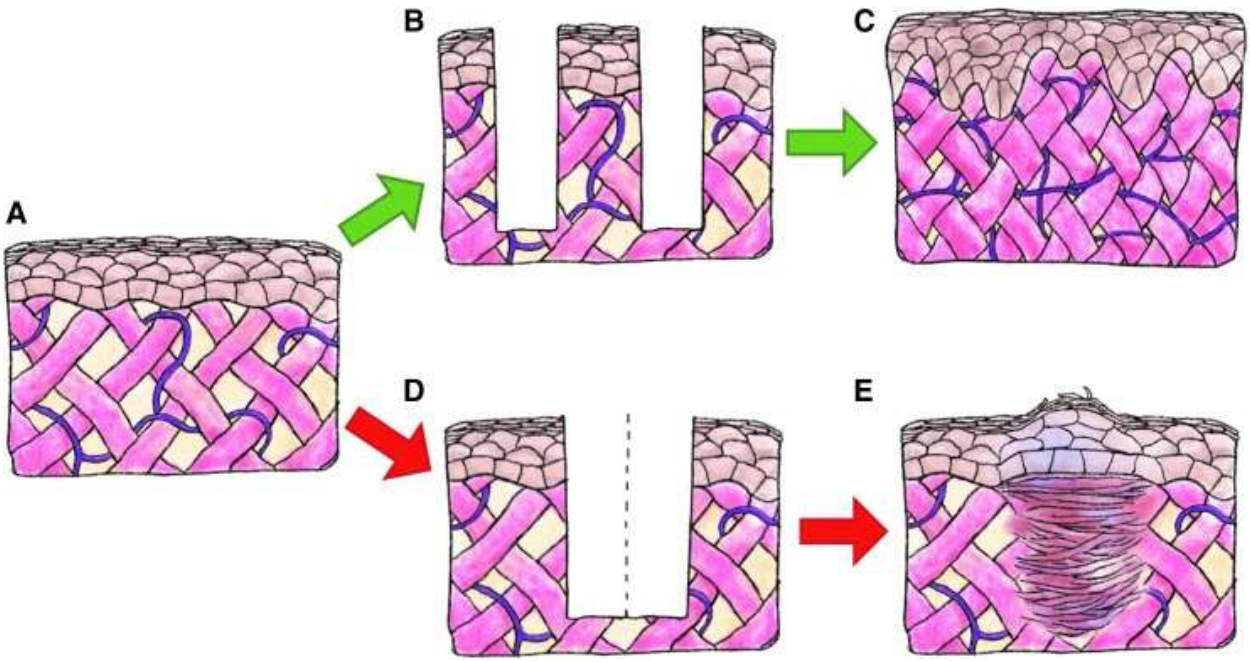

Figure 2-1: Size-dependent dichotomy in healing response of skin. Untreated skin tissue is depicted in (A), with keratinocytes shown in brown, dermal collagen fibers shown in pink, and elastin fibers in purple. When skin is injured by a series of nonconnecting small wounds (B), the tissue heals by completely regenerating the composition and architecture of normal tissue and can even bring about improvements in tissue quality (C). In contrast, when the wound is large in any one dimension (even if there is equal or less total tissue loss-(D) depicts a wound that is the exact combination of the two small wounds in (B), with the dotted line denoting where the edges of the two small wounds would be if they remained discrete injuries), the wound heals by scarring (E).

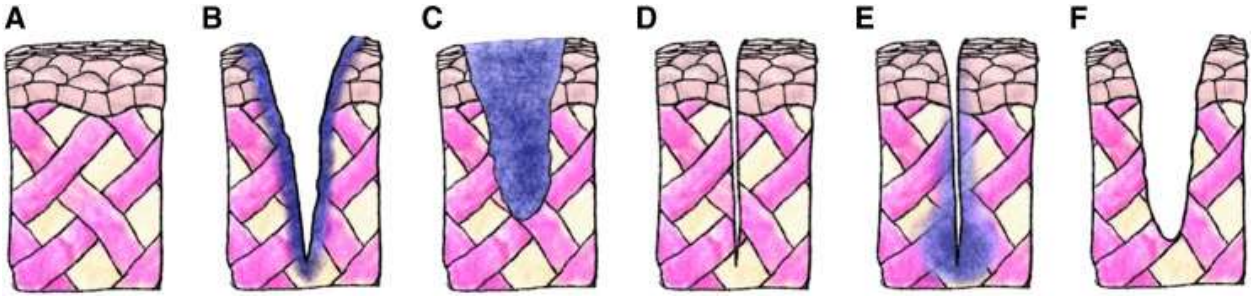

Figure 2-2: Current clinical options for producing microinjuries. (A) Untreated skin tissue. (B) Ablative fractional laser: laser microbeam vaporizes a thin column of tissue, and also leaves behind a zone of thermal damage in the adjacent tissue (depicted in purple). (C) Nonablative fractional laser: tissue is heated and denatured in a fractional pattern, but not vaporized. (D) Microneedling: piercing injury made by small needles, no tissue is removed. (E) Radiofrequency microneedling: in addition to piercing injury, radiofrequency heating is used to cause thermal damage in the surrounding tissue. (F) Fractional tissue harvesting: small harvesting needles are used to extract tissue, causing tissue loss without thermal damage.

of underlying inflammation), increasing tissue pliability and range of motion, and improving overall quality of life[27-29, 43, 44]. There have even been anecdotal reports of functional hair follicles and sweat glands regenerating in scars that had been devoid of these structures[25, 45].

Fractional resurfacing seems to stimulate different remodeling responses in different defects. In hypertrophic scars consisting of dense, thick, disorganized collagen bundles, AFL induces looser but more organized collagen[29, 46, 47]. Conversely, atrophic scars – characterized by a paucity of collagen leading to depressions in the skin – respond to AFL by thickening of the epidermis and increasing dermal collagen deposition[48]. These findings suggest that, rather than inducing a constant set of effects, fractional resurfacing elicits a homeostatic response that induces remodeling towards a more normal state. Consistent with this view, healthy skin showed no histological evidence of fractional resurfacing after 3 months[37, 49] (whereas beneficial effects on scar remodeling persist for years[28]), and pretreatment of normal skin in a large animal model provided no benefit towards the subsequent surgical scarring response[50].

2.2 Mechanisms of Microinjury Regeneration

Of the treatment modalities proposed in this thesis, microinjury perturbation has by far the most complex and least understood mechanism. This section provides a detailed review of the reported and putative mechanisms involved. Subsections 2.2.1 to 2.2.6 provide a literature survey for important components of the response to microinjuries in skin. Subsection 2.2.7 synthesizes this information and describes a general mechanism for the reduction of fibrosis through microinjury regeneration.

2.2.1 TGFβ

TGFβ is important for normal wound healing, and a key regulator of fibrosis and scarring as it promotes expression of type I collagen and tissue inhibitors of metalloproteinases (TIMPs)[51]. TGFβ is secreted by immune cells during wound healing to stimulate fibroblast differentiation and collagenesis[52]. Latent TGFβ is stored in the ECM and can later be activated by matrix turnover, thereby coupling collagenesis to the mechanical properties of the ECM[52]. There are three TGFβ isoforms with distinct functions. TGFβ1 and TGFβ2 promote both wound healing and scar formation, while TGFβ3 inhibits scar formation and is considered particularly important for scarless healing of the fetus[53]. TGFβ signaling is often suppressed in chronic wounds[54]. TGFβ is also an important chemokine for macrophages and neutrophils following acute injury[51].

In photodamaged skin, TGFβ is upregulated 3 days post-AFL and expression decreases over 30 days[55]. Studies in burn scars using more frequent timepoints found biphasic TGFβ expression after fractional resurfacing. TGFβ1 and TGFβ3 are transiently upregulated 1hr post-op[56]. TGFβ1 returns to baseline at 24-48hrs while TGFβ3 and TGFβ2 are downregulated compared to baseline[56, 57]. TGFβ1 and TGFβ3 expression increases again 96 and 168hrs post-op[56]. One study on long-term TGFβ expression, using immunohistochemistry at baseline and 6 months post-op, found that staining intensity for TGFβ1 is reduced at 6 months post-op compared to pre-treatment, and that TGFβ1 is primarily found in fibroblasts and in the ECM[47].

Interestingly, neutralization of TGFβ1 and TGFβ2 reduces scarring but inhibition of just one of these has no effect[58], highlighting the need to understand changes in each TGFβ isoform. However, the three TGFβ isoforms are frequently not distinguished in the literature, and TGFβ2 is often neglected even when individual isoforms are investigated.

A better understanding of how each isoform is affected by fractional resurfacing, especially in the long term, is needed.

2.2.2 Heat Shock Proteins (HSPs)

HSPs can be activated by many forms of stress, including heat, trauma, toxins, and hypoxia[59]. Classically, HSPs act as chaperones and promote cell survival by correcting stress-induced protein misconformations[59, 60]. More recently, HSPs have been recognized as regulators of the wound healing response[61]. Dysregulation of HSPs is involved in a number of fibrotic conditions and different HSPs can either promote or inhibit TGFβ signaling[62-66]. HSPs have also been investigated as potential therapeutic targets for fibrosis, either through inhibition (e.g. HSP90 inhibition reduces hepatic[67] and renal fibrosis[68]) or induction (e.g. HSP70 induction reduces hepatic[69] and pulmonary fibrosis[70]). These findings indicate competing roles for HSPs, and the relative importance of HSPs in fibrosis and wound healing is an area of ongoing research.

HSP47 is a chaperone involved in collagen processing and its expression correlates with collagen synthesis and fibrosis progression in many organs[62, 71]. The HSP70 family, primarily consisting of the constitutively expressed HSP73 and inducible HSP72, has also been studied in some detail. In photodamaged skin, AFL causes HSP70 upregulation from 1hr post-op through day 14[72]. NAFL showed similar results[73]. The pattern of HSP expression has been further studied in healthy skin. NAFL caused upregulation of HSP47 and HSP70 in tissue immediately surrounding the microinjury at 1 day post-op[74, 75]. At day 7, HSP47 and HSP70 are expressed inside the treatment zone as well as more diffusely throughout the dermis[75]. NAFL and fractional radiofrequency microneedling have both been reported to induce HSP70 expression[76, 77], which is severely attenuated in diabetic skin[78], with an expression time course that correlates with delayed healing[79]. Long-term upregulation of HSPs has been reported after large-area ablative laser

resurfacing[49]. If a similar response occurs after fractional resurfacing it could account for the ongoing remodeling of scars for months after treatment, though experimental confirmation is needed.

2.2.3 Collagen Synthesis and Degradation

In healthy tissue there is a balance between collagen synthesis and degradation[80]. Tipping that balance either way is pathologic – excessive collagen synthesis leads to hypertrophic scarring, while excessive degradation is characteristic of both skin aging and chronic wounds. Collagen degradation is commonly estimated through MMP expression, but many factors influence MMP activity – most notably TIMPs and synthesis in an inactive proenzyme form – and the more accurate method for determining collagen degrading activity is zymography[81]; however, such studies have yet to be performed for laser resurfacing techniques. MMPs are a large group of enzymes with varying activities for the many components of the ECM (collagens, fibronectin, laminin, etc.). In photoaged skin, MMP-1, MMP-3, MMP-9, MMP-10, MMP-11, and MMP-13 are upregulated between day 7 and 14 post-AFL. MMP-1, MMP-3, and MMP-13 expression drops off after day 14 while MMP-9, MMP-10, and MMP-11 expression continues to increase through day 21[82]. Similar effects have been reported for other modalities. NAFL caused upregulation of MMP-1, MMP-3, and MMP-9 at day 1 post-op, with significant decay at day 7[73]. It was also found that MMP-1 and MMP-3 were localized to the treatment zone, while MMP-9 was dispersed throughout the dermis[73]. It is likely that there are similar patterns of MMP expression across the modalities, though with varying magnitudes. Far fewer MMPs have been investigated for AFL in scar tissue. One study reported MMP-1 upregulation at 48hrs post-op and no significant change in MMP-13[57].

Collagen synthesis is typically approximated by collagen mRNA levels. In scars, collagen mRNA exhibits a biphasic response to AFL in line with TGFβ expression. Both COL1A1

(type I collagen) and COL3A1 (type III collagen) are upregulated at 1hr post-op, fall below or near baseline at 24-48hrs, then are again upregulated at 168hrs[56, 57]. NAFL in photodamaged skin reduced COL1A1 and COL3A1 at 1 day post-op, followed by upregulation from day 14 through 28, with procollagen I protein levels following the same trend[83]. Immunohistochemical investigation of NAFL in healthy skin showed gradual increase in type III collagen staining inside the treatment zone until 1 week post-op[74]. In a healthy mouse model, AFL caused increased protein levels of type III collagen from day 3 through 56 post-op and type I collagen from day 28 through 56[84].

These findings are not altogether surprising – as with any acute injury, laser resurfacing promotes matrix turnover in the short-term. While the remodeling phase of wound healing can continue for over a year after injury[85], this on its own does not fully explain why there is continued scar regression in the months following treatment. Long-term measurements are required to determine how fractional resurfacing changes the balance between collagen synthesis and degradation.

2.2.4 Apoptosis

Fractional resurfacing causes tissue damage through thermal and/or mechanical injury. Apoptosis is an essential component of the biological responses to tissue damage. Once viewed as a largely cell-autonomous process, there is now increasing understanding that apoptosis has significant impact on the local milieu, inducing proliferation and remodeling of adjacent cells and tissue, at least in part via ectopic expression of Wnt and induction of p53[86]. Apoptosis plays a key role in wound healing by inducing mitogenic signals that drive regeneration[87, 88], but there is currently little data on how apoptosis may be involved in the regenerative effects of fractional resurfacing. Apoptosis was observed within 24h of AFL and steadily declined over 7 days. The authors concluded that apoptosis induces a paracrine cascade that leads to cell proliferation and stimulates stem

or progenitor cells to participate in tissue regeneration[89]. Another study compared five different laser devices using TUNEL assay. Thermal tissue damage and penetration depth differed widely, as did the extent of apoptosis and necrosis[90], and it is unclear whether clinical outcomes correlate with the extent, location, or distribution of apoptosis. It has been proposed that apoptosis can alter local tissue tension, induce remodeling in nearby tissue, and influence the behavior of neighboring cells through paracrine signaling[86]. Given that scars are characterized by increased stiffness that can be substantially improved by fractional resurfacing, apoptosis could play a role in treatment-induced tension relief in fibrotic tissues. Wnt proteins, which are often secreted by apoptotic cells, can regulate the cytoskeleton[91] and are also important signaling molecules in epidermal skin stem cells[92]. Whether those two mechanisms merely co-exist or act in concert is unclear[86].

2.2.5 Other Findings

Where overlap exists in the literature, cytokine expression between the different laser resurfacing modalities is generally similar. The pro-inflammatory cytokines IL-1β, IL-6, TNFα, and MCP-1 are all upregulated shortly after treatment. IL-6 and MCP-1 return to baseline in 96hrs and 24hrs, respectively[56]. TNFα expression significantly decays within 1 week[73]. IL-1β upregulation is longer-lived, with expression sustained up to 14 days post-op[73]. One study reported bFGF expression decreased at 48hrs[57], while another found increased expression at 3 and 30 days post-op[55].

VEGF is a key regulator of angiogenesis and vascular permeability in the early stages of the response to injury. AFL caused significant upregulation of VEGF at day 1 and 3 post-op in a murine model, with no significant difference from controls after day 7[84], while mild upregulation of VEGF up to 30 days post-op was reported in photodamaged human skin[55]. These findings are consistent with reports of increased vascularity after fractional

resurfacing[42, 93]. It has also been reported that VEGF can influence MMP activity and collagen deposition[94] and there is some evidence that it may promote scar formation in later stages of wound healing[95]. Further investigation of VEGF is required to better understand its role in scar remodeling.

Qu *et al* showed that miR-18a and miR-19a expression is increased after AFL in scars[57]. These miRNAs belong to the miR-17/92 cluster which has been shown to suppress TGFβ signaling[96]. Most research to date has focused on the role of miR-17/92 in cancer, but a few studies have also indicated a potential protective role in fibrosis[97, 98].

Kim *et al* performed the only transcriptome level study to date for fractional laser resurfacing, although their analysis of the dataset was limited to a handful of genes[99]. This study looked at AFL in healthy skin and emphasized Wnt5a, an anti-apoptotic gene and fibroblast mitogen, and CYR61, which has been shown to inhibit type I collagen synthesis and promote degradation. It was also shown that CYR61 expression was upregulated throughout the dermis, rather than isolated to the injury sites.

2.2.6 Findings in Other Modalities used for Fractional Resurfacing

Microneedling is another common method for producing microinjuries. It is generally not as effective as laser resurfacing but also has lower risk of negative outcomes, so it has achieved some popularity as a treatment for individuals seeking minor improvements. Microneedling involves a drum covered in fine needles (usually 0.5-1.5mm in length) repeatedly rolled over the skin to create hundreds of punctures per square centimeter[100, 101]. It is most commonly used for treatment of atrophic scars from acne, as it has shown limited success for hypertrophic scars[102].

The mechanism of microneedling has received even less attention than that of laser resurfacing. At one point a theory for microneedling was proposed based on the needles creating electrical field perturbations to stimulate proliferation and release of growth

factors[102]. However, recent publications suggest that microneedling functions similarly to fractional laser resurfacing. Microinjuries induce a minor acute immune response, with associated release of inflammatory cytokines. TGFβ and FGF promote fibroblast proliferation and differentiation, increased matrix turnover, and angiogenesis. The result is normalization of the matrix architecture with increased deposition of collagen and elastin[101, 103].

Fractional radiofrequency irradiation is another common microinjury method. Similar to NAFL, this technique creates small, isolated columns of thermal injury. The main benefits of radiofrequency over laser resurfacing are less disruption of the epidermis, lower risk of dyspigmentation, and avoidance of side effects caused by light absorption by melanin in darker skin types[104]. Broadly speaking, fractional radiofrequency causes similar effects to laser resurfacing, with upregulation of HSPs, MMPs, TGFβ, and pro-inflammatory cytokines leading to increased collagen type I, collagen type III, and elastin in the dermis[105, 106].

2.2.7 General Mechanism of Microinjury Regeneration

A summary of the putative mechanisms involved is depicted in **Figure 2-3**.

There remains a crucial missing link between the short-term response and long-term results of fractional resurfacing. The sequence of events immediately following treatment and the eventual histological changes are both well described, but the mechanism by which one leads to the other is poorly understood. Through speculation and bringing in elements from general fibrosis research, the pieces can be connected to formulate a general mechanism of microinjury regeneration. For scar remodeling, mechanical changes in the ECM likely play a crucial role. Microinjuries enable infiltration of the densely packed, highly cross-linked collagen fibrils which are resistant to degradation[107, 108]. The acute inflammatory response recruits a population of cells (macrophages and

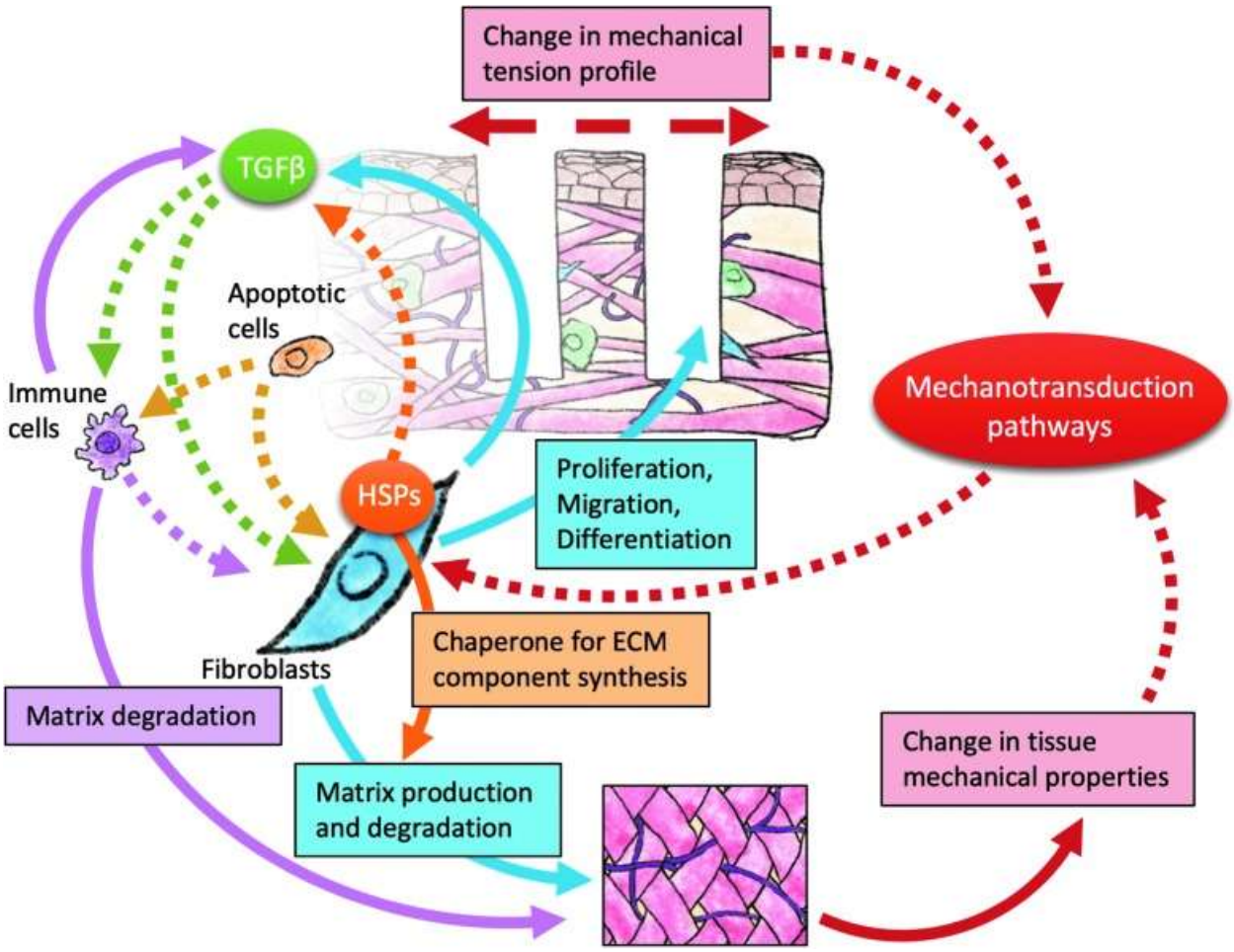

Figure 2-3: Putative mechanisms involved in fractional resurfacing-induced remodeling. Solid arrows denote direct involvement in specific processes, dotted arrows denote regulatory roles. The TGFβ pathway regulates fibroblast function both directly and indirectly through effects on immune cells. Both fibroblasts and immune cells also produce TGFβ. Paracrine signaling from apoptotic cells stimulates proliferation and differentiation of neighboring cells, and modulates the inflammatory response. HSPs interact with TGFβ signaling and also serve as chaperones for the production of ECM components. Tissue biomechanics may be altered by both the microinjuries from fractional resurfacing and the ECM remodeling process, resulting in feedback regulation of fibroblast functions through mechanotransduction pathways.

neutrophils) that strongly promote matrix turnover as a part of the normal wound healing process. This short but potent response is sufficient to significantly reduce scar stiffness, as shown by immediate clinical improvements (e.g. patient showing improved range of motion in 3 days[44]). But improvements continue long after resolution of inflammation. The long-term response could be initiated by the precipitous drop in tissue stiffness provided by the short-term activity. Collagen deposition and degradation is a dynamic process, even in long-healed scars[109-111]. Furthermore, tissue stiffness forms a crucial positive feedback loop with fibrosis; greater stiffness promotes collagen deposition and inhibits degradation, therefore promoting further increases in tissue stiffness[31]. A reduction in stiffness could tip the balance to be less in favor of collagen deposition, enabling long term remodeling towards normal ECM. The importance of other factors discussed above, such as HSPs, Wnt, and CYR61, and how they may fit into a potential mechanism needs to be addressed by future research.

2.3 Methods

2.3.1 Animals

All animal work was approved by the Massachusetts General Hospital Institutional Animal Care and Use Committee and performed in compliance with the US National Research Council's Guide for the Care and Use of Laboratory Animals and US Public Health Service's Policy on Humane Care and Use of Laboratory Animals. Our experiments used male Wistar rats purchased from Charles River Laboratories. Animals were housed in a controlled environment with food and water ad libitum. For cirrhosis experiments, rats received biweekly injections of thioacetamide at 200mg/kg for 12 weeks followed by a 1 week wash out period.

2.3.2 Surgery protocol

Animals were anesthetized with isoflurane and prepared for surgery by clipping fur on the abdomen and disinfecting with 10% povidone-iodine. A laparotomy was performed with a 1-2 inch midline incision beginning from the xyphoid. The left lobe of the liver was exposed using sterile swabs. The UltraPulse fractional CO2 laser (Lumenis, Yokneam, Israel) with sterile spacer was brought to the liver surface. The laser ablates a 9x9 array of microinjuries in an approximately $50mm^2$ area, with each microinjury receiving two pulses of 15mJ. The majority of animals were treated with the laser in 4 areas, but 2-3 areas were occasionally used depending on the size of the liver. Once bleeding stopped, the muscle and skin were closed with absorbable sutures. Animals were euthanized via cardiac puncture at 0hr, 2hr, 4hr, 6hr, 3d, 7d, and 14d after surgery.

2.3.3 Histology

Tissue for histological analysis was collected at the time of euthanasia. Samples for hematoxylin & eosin (H&E) and terminal deoxynucleotidyl transferase dUTP nick-end labeling (TUNEL) staining were fixed in 4% formaldehyde, embedded in paraffin blocks, and cut into 5μm sections. TUNEL staining was performed using the DeadEnd Fluorometric TUNEL kit (ProMega, Madison, USA), according to the manufacturer's instructions. Samples for nitro blue tetrazolium chloride (NBTC; Thermo Fisher Scientific, Waltham, USA) and immunofluorescence staining were embedded in OCT and snap-frozen on dry ice. 10μm (for NBTC) or 5μm (for immunofluorescence) sections were cut in a cryostat at $-20^{o}C$. NBTC viability staining was performed by incubating the sections with NBTC for 15 min, followed by counterstaining with eosin. For immunostaining, primary antibodies against alpha-smooth muscle actin (SMA, marker of activated hepatic stellate cells; diluted 1:500; Abcam, Cambridge, UK, Cat# ab124964, RRID:AB_11129103), hepatic nuclear factor 4 alpha (HNF4a, hepatocyte marker; 1:100; Abcam Cat# ab41898,

RRID:AB_732976), and phosphorylated c-Jun (pcJun, immediate early liver regeneration marker[112]; 1:400; Abcam Cat# ab30620, RRID:AB_726902) were used. The sections were then stained with Alexa Fluor 488 or 594 conjugated secondary antibody (Thermo Fisher Scientific) and DAPI (Thermo Fisher Scientific). Slides were imaged with a Nanozoomer 2.0 HT slide scanner (Hamamatsu, Hamamatsu City, Japan).

2.3.4 RNAseq

Tissue for RNAseq analysis was collected at the 4hr euthanasia timepoint from healthy and cirrhotic rats. Two roughly 25mg samples were collected from each animal – one from an ablated region, and one from an untreated region in the same lobe to be used as a control – and placed in RNA*later* (Thermo Fisher Scientific). Samples were stored at 4°C overnight and then at -20°C until use. RNA extraction was performed using the RNeasy midi kit with proteinase K digestion and on-column DNase digestion according to the manufacturer's instructions (Qiagen, Hilden, Germany). The samples were then sent to Admera Health for quality control, library preparation, and sequencing. Libraries were prepared using NEBNext Ultra II (New England Biolabs, Ipswich, USA) with poly(A) selection and sequenced on a NovaSeq 6000 (Illumina, San Diego, USA) with 40M 150bp paired-end reads per sample.

Sequencing data quality was assessed with FastQC[113] and trimmed with Cutadapt[114]. Transcript abundance was quantified with the Salmon quasi-mapping tool[115]. Differential expression analysis was performed using DESeq2 (RRID:SCR_015687) in R[116]. We used a difference-in-differences model to identify genes that responded differently between the ablated cirrhotic and ablated non-cirrhotic liver, while controlling for the differences between the unablated samples. The model also accounted for sample pairing (i.e., ablated and control samples taken from the same animal). Over-representation analysis (ORA) and gene set enrichment analysis (GSEA) for gene ontology gene sets were

performed with the clusterProfiler (RRID:SCR_016884) package[117]. ORA was run on the list of differentially expressed genes (DEGs) with FDR<0.05. GSEA was performed on the list of all genes ranked by $\log_2$(fold change). Fold change was calculated using the apeglm method for log fold change shrinkage[118]. Gene sets were enriched if FDR<0.05 with Benjamini-Hochberg correction. ORA and GSEA figures were generated with the enrichplot package[119].

2.3.5 Hyperspectral imaging

Hyperspectral imaging is a technique for measuring the spectra of a pixel over a range of wavelengths by dividing it into many contiguous spectral bands. It can be used with reflectance spectroscopy to non-invasively measure concentrations of oxy- and deoxyhemoglobin and generate a 2D spatial map of tissue oxygen saturation[120].

Hyperspectral images were acquired with the HyperView Imaging System (HyperMed Imaging, Memphis, USA). The camera was held at a fixed distance from the surface of the exposed left lobe, as marked by a laser distance gauge incorporated in the device. Images were acquired immediately before ablation to establish baseline and again at the time of euthanasia. Image acquisition took approximately 1 second. Oxygen saturation maps were generated using the software included on the device.

2.3.6 Tomato lectin vascular perfusion

Tomato lectin is a common tool for staining perfused vessels. It is most commonly used in mice and delivered via tail vein injection to circulate throughout the body. We found it was not feasible to intravascularly inject enough compound in rats to sufficiently stain the liver. Consequently, we used retrograde perfusion of the left lobe after euthanasia. The hepatic artery and splenic portal vein were clamped shut. 4-0 sutures were used to tie the portal vein shut as well as the branches of the portal vein leading to the medial

lobe, right lobe, and caudate lobe. The branch of the hepatic vein coming from the left lobe was cannulated with a 19G needle connected to a short length of silicone tubing, and sutures were tied around the vessel and needle to limit backflow. Fluorescently labelled tomato lectin (Vector Labs, Newark, USA) was diluted to 50μg/mL in PBS immediately prior to injection. 15mL of the tomato lectin solution was injected over approximately 2 minutes. After a further 2 minute incubation period, swabs were gently rolled over the left lobe to help distribute the solution. The portal vein was then cut to allow efflux and another 15mL was injected. Tissue samples were collected for formalin fixation and TUNEL staining.

2.4 Results

2.4.1 Parameter sweep of fractional laser treatment intensity

As the fractional laser has not previously been used in the liver, we performed a parameter sweep with healthy rats to determine the appropriate treatment settings. The laser variables are pulse energy, number of pulses per microinjury, and density of microinjuries. Our objective was to identify a combination of settings that produced distinct microinjuries, each less than 500μm in diameter and at least 2mm in depth. These results are shown in **Appendix Figure A-1**. Excessive pulse energy or density of microinjuries causes collateral damage to the tissue between ablation sites. Treatment with 15mJx2, 5% density produced microinjuries approximately 300μm in diameter and 2mm deep. This treatment intensity was used for all subsequent experiments.

2.4.2 Microinjuries are well tolerated in the healthy liver but cause large zones of cell death in the cirrhotic liver

We first investigated the tissue response to fractional laser ablation from 3 days post-ablation up to 14 days. At the 3 day timepoint in the healthy liver, the microinjuries were faintly visible on the surface of the liver (**Figure 2-4 A**). Both grossly and histologically, the injuries appeared uniform in size and spacing, and there was no evidence of additional damage beyond the microinjuries (**Figure 2-4 A, C, E**). By 7 days, we were no longer able to find any gross or histological evidence of the microinjuries. The cirrhotic liver showed a vastly different response. At 3 days post-ablation, the ablated regions were clearly visible (**Figure 2-4 B**). In addition, the injuries were enlarged and distorted. On histology, it was difficult to discern any pattern of the injuries or identify where the individual microinjuries initially were (**Figure 2-4 D, F**). There are enlarged and heterogeneous zones of injury that vary greatly in size and shape, with some measuring several millimeters across. HNF4a staining shows there were no hepatocytes within these zones (**Figure 2-4 F**). The ablation sites and associated tissue damage were still apparent through 14 days post-ablation. Unablated immunofluorescence reference images are provided in **Appendix Figure A-2**.

To better understand the time course of this response, we looked at earlier timepoints from immediately after ablation up to 6hrs. TUNEL staining immediately after ablation showed a small circle of TUNEL positive cells at each microinjury site where the laser coagulated tissue (**Figure 2-5 A**). Little change was observed at 2hrs (**Figure 2-5 B**). After 4hrs, cell death was observed beyond the initial ablation sites (**Figure 2-5 C**). At 6hrs the enlarged and heterogeneous injury pattern observed at the 3 day timepoint was fully established (**Figure 2-5 D**). At this timepoint, the laser injury appears as a bright and dense region of coagulation on TUNEL staining and is easily distinguished from

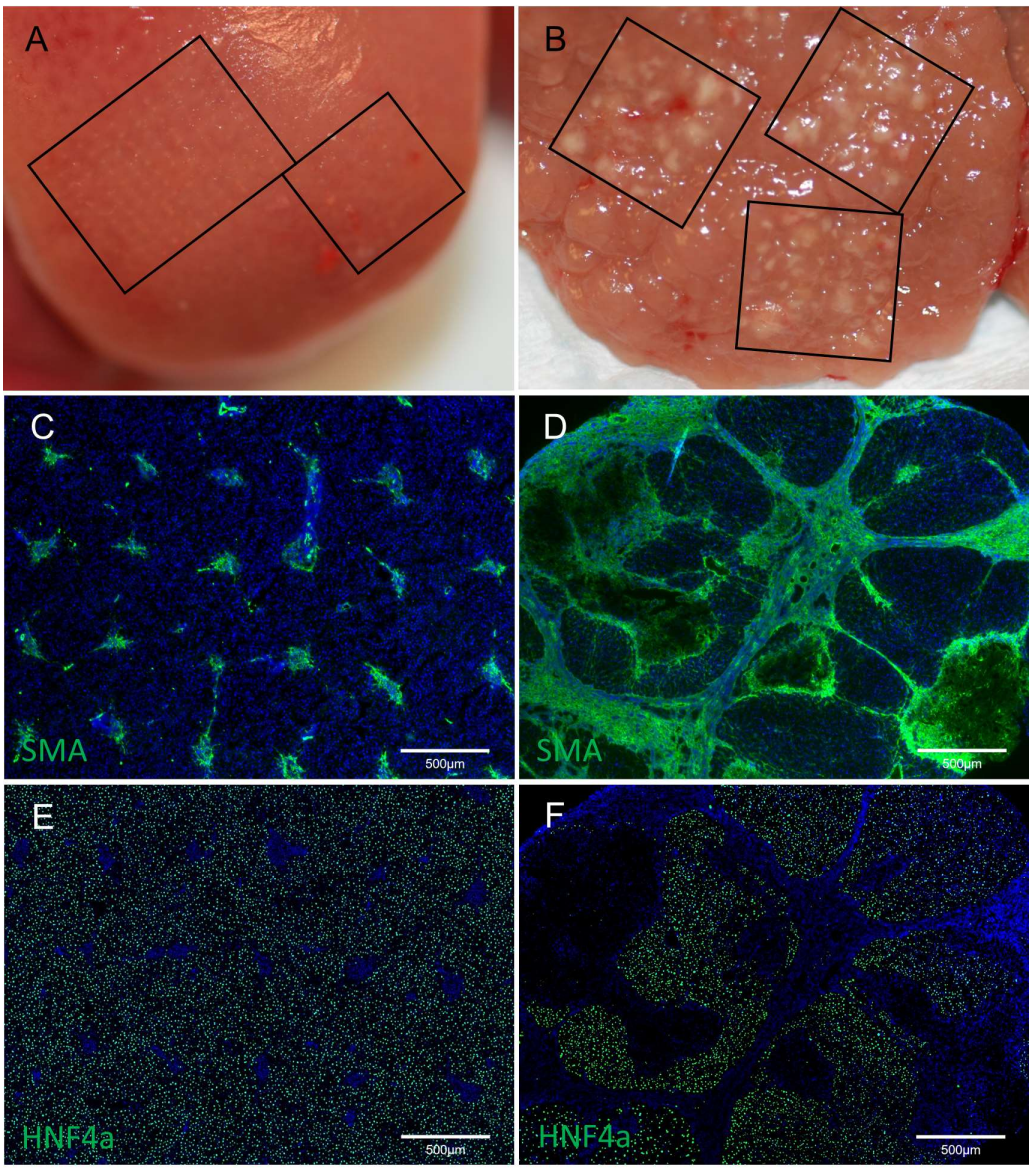

Figure 2-4: Representative images comparing response to fractional laser ablation in the healthy (A, C, E) and cirrhotic (B, D, F) liver 3 days after treatment. (A, B) Gross images. Treated regions are outlined with black boxes. The microinjuries in the healthy liver (A) are faintly visible and appear uniform and regular. Injuries in the cirrhotic liver are clearly visible and appear enlarged and misshapen. (C, D) SMA stain showing activated stellate cells recruited to the injuries. Similar to the gross images, the injuries in the healthy liver are small, regular, and uniformly spaced. The injuries in the cirrhotic liver are enlarged and heterogeneous, and the original laser ablation pattern is no longer discernible. (E, F) HNF4a stain for hepatocytes. Hepatocytes are absent from the zones of injury. (n=4 healthy, n=6 cirrhotic)

subsequent cell death. These results show that the laser initially produces the expected uniform size and spacing of microinjuries, and the heterogeneous injury zones develop as a response in the hours after ablation.

2.4.3 Zones of cell death are heterogenous and influenced by local vasculature

There was heterogeneity in the tissue damage pattern, even between adjacent microinjuries. For the majority of injuries, the zone of cell death spreads throughout the cirrhotic nodule containing the microinjury (**Figure 2-6 A**). The injury did not spread to adjacent nodules, i.e., there was no cell death in nodules that did not contain a microinjury. This was observed in both small and large nodules. Importantly, we also observed that there was almost always a band of cells next to the septa that survived (**Figure 2-6 A**). The band of surviving cells may be more easily seen on the NBTC viability stain (**Appendix Figure A-3**). This was the case even when the microinjury occurred close to the septa and the zone of cell death spread throughout the rest of the nodule (**Figure 2-6 B**). Less frequently, we observed injuries that did not spread – even when there were multiple microinjuries within the nodule (**Figure 2-6 C**) – or that would only spread out in one direction from the microinjury (**Figure 2-6 D**). These patterns of injury were uncommon and were found within the same sections as the more typical injury pattern described above. In the healthy liver, cell death was limited to the region immediately surrounding the laser ablation site, and there was no change from 2 to 6hrs after treatment (**Appendix Figure A-4**).

In one section we observed a unique injury pattern of a small island of viable cells surrounded by TUNEL positive cells (**Figure 2-6 E**). By comparing this to H&E staining of a serial section (**Figure 2-6 F**), we found that the viable cells bordered a larger vessel

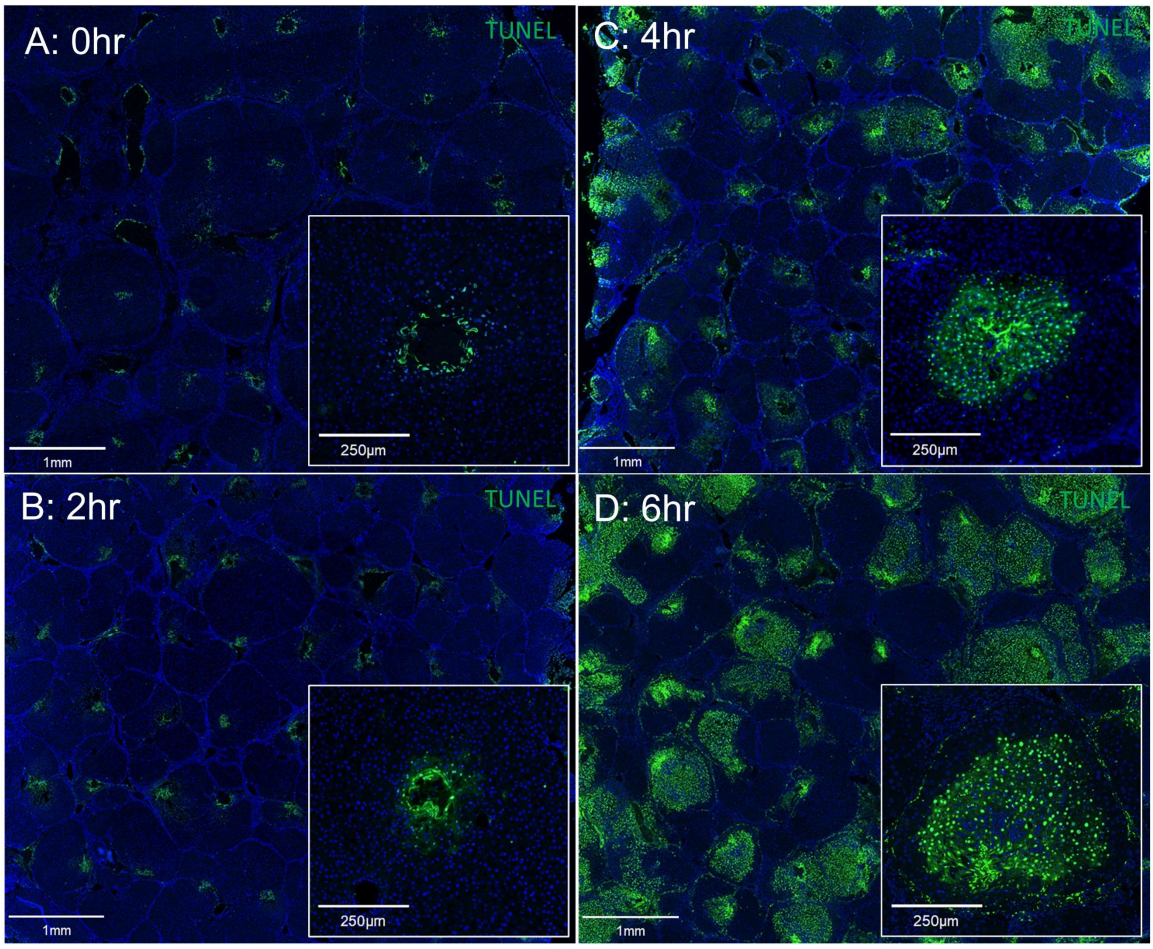

Figure 2-5: Development of the zones of cell death over the first 6hrs after fractional laser ablation. (A-D) Representative TUNEL stain of the cirrhotic liver at 0hr, 2hr, 4hr, and 6hr after fractional laser ablation, respectively. At 0hr and 2hr, there is little cell death beyond the initial injury from the laser. At 4hr, some zones of cell death begin to develop. The initial injury appears as bright, TUNEL positive coagulated nuclei (cluster of bright green elongated and distorted ribbons). Subsequent cell death is shown by TUNEL positive nuclei with the normal spherical morphology. By 6hr, the exacerbated and heterogeneous injury pattern observed at 3 days is established. (n=3 per timepoint)

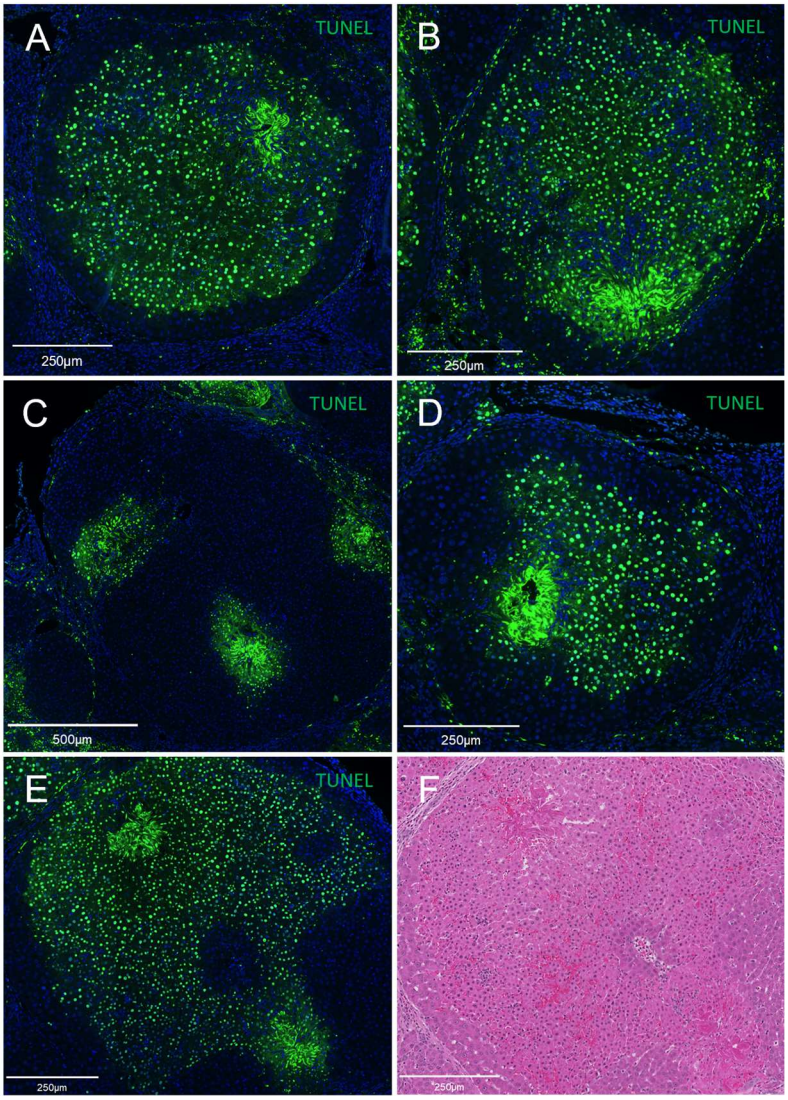

Figure 2-6: Heterogeneity of response to microinjuries at 6hrs after fractional laser ablation in the cirrhotic liver. (A) The most common nodule injury pattern. The zone of cell death encompasses the entire nodule, except for a band of surviving cells near the septa. (B) Even injuries far to one side of a nodule can cause cell death throughout the majority of the nodule, while cells close to the microinjury but near the septa still survive. (C) Some nodules can contain multiple microinjuries but have very little cell death. (D) Some zones of cell death appear to spread in only one direction from the microinjury. (E) Observation of an island of surviving cells surrounded by TUNEL positive cells. (F) H&E staining of a serial section showed that these surviving cells are near a blood vessel running through the middle of the nodule.

running through the middle of the nodule – an uncommon anatomical feature at this stage of cirrhosis due to the way the septa form. Although few cases of this were observed, when considered in addition to the observation of the band of viable cells next to the septa – which contain many perinodular vessels – it raised the suspicion that cells are spared by proximity to blood vessels.

2.4.4 Gene sets related to ischemia, hypoxia, and angiogenesis are enriched after microinjury ablation in the cirrhotic liver

To further characterize the short-term response, we performed RNAseq differential expression analysis with samples from the 4hr timepoint. For our analysis we used a difference-in-differences model to identify genes that responded differently between the ablated cirrhotic and ablated non-cirrhotic liver, while controlling for the differences between the unablated samples. Direct comparison of the ablated cirrhotic and ablated healthy liver would return a list of DEGs dominated by expression differences between healthy and cirrhotic liver unrelated to the microinjury response. The difference-in-differences model allowed us to focus specifically on DEGs underlying the different response to microinjuries between the two tissue states. We identified 520 DEGs with FDR<0.05. ORA of this list of DEGs returned enrichment of gene sets related to ischemia, hypoxia, and angiogenesis, including: response to hypoxia, cellular response to decreased oxygen levels, response to starvation, and regulation of vasculature development (**Figure 2-7 A, B**). The DEGs contributing to the enrichment of these gene sets included well-known ischemia related genes such as HIF1a and VEGFA (**Figure 2-7 C**). GSEA, which identified enriched gene sets on a ranked list of all genes rather than specifically the DEGs, returned similar results (**Appendix Figure A-5**).

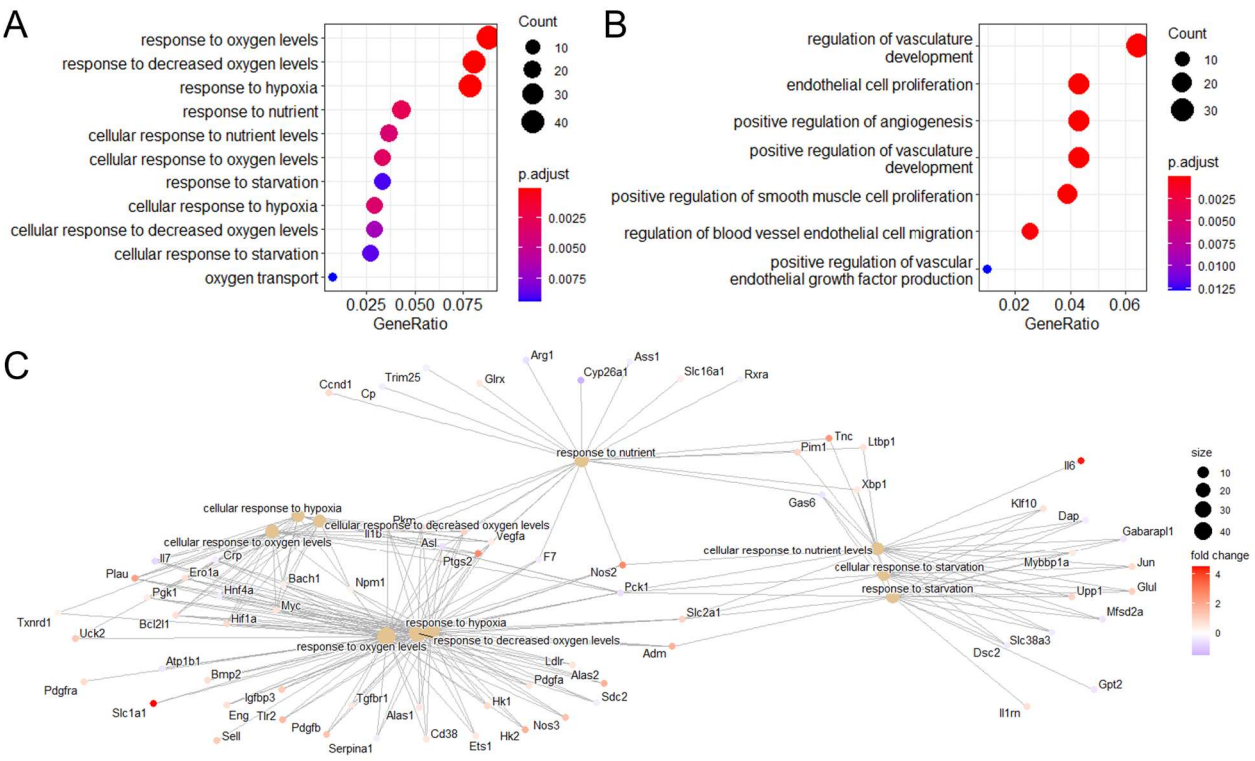

Figure 2-7: Over-representation analysis (ORA) of RNAseq results comparing healthy and cirrhotic liver at 4hrs after fractional laser ablation. (A) Dotplot of selected enriched gene sets related to ischemia and hypoxia. (B) Dotplot of selected enriched gene sets related to angiogenesis. (C) Concept network plot showing the DEGs contributing to enrichment of select ischemia and hypoxia related gene sets. (n=4 healthy, n=4 cirrhotic)

2.4.5 Microinjury ablation reduces tissue oxygen saturation and disrupts perfusion in the cirrhotic liver but not the healthy liver

The RNAseq analysis supported our hypothesis that the exacerbated response to microinjury ablation in the cirrhotic liver was a result of ischemia. To further examine this, we directly investigated the two components of ischemic injury – reduced tissue oxygenation and disrupted blood supply.

Spatial maps of oxygen saturation were acquired with hyperspectral imaging. At the 2hr timepoint in the cirrhotic liver, there was clearly visible decreased tissue oxygen saturation in the areas subjected to microinjury ablation (**Figure 2-8 A**). By 6hrs, the ablated regions still had lower oxygen saturation, but it was less apparent (**Figure 2-8 B**). This is likely due to rebalancing of supply and demand. We have shown that a large percentage of cells in these areas are undergoing apoptosis at the 6hr timepoint (**Figure 2-5 D**), so the oxygen demand would be significantly decreased. There was no apparent decrease in tissue oxygen saturation at 2hrs or 6hrs in the ablated areas of the healthy liver (**Figure 2-8 C, D**).

The integrity of the blood supply was investigated using tomato lectin perfusion. At the 2hr timepoint in the cirrhotic liver, prior to the development of the zones of cell death on TUNEL staining, large regions of tissue in the ablated areas were not perfused (**Figure 2-9 A**; **Figure 2-10 A**). We can also identify similar features to the injuries that later develop: many nodules are not perfused at all, some are entirely perfused except around the immediate vicinity of the injury, and some are partially perfused. By 6hrs the tomato lectin stain had the same features as at the 2hr timepoint, but the zones of cell death had now developed on TUNEL staining (**Figure 2-9 B**; **Figure 2-10 B**). There was no overlap between the tomato lectin and TUNEL staining, i.e., the unperfused regions matched the

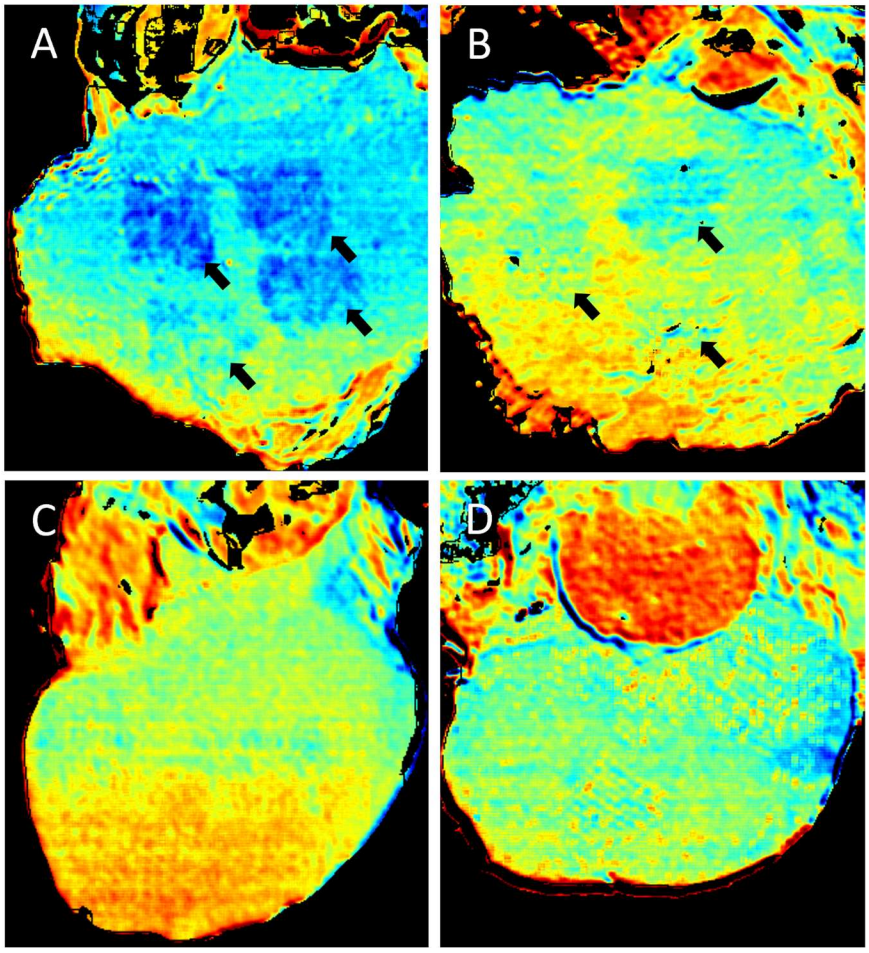

Figure 2-8: Relative tissue oxygen saturation measured via hyperspectral imaging. (A, B) Representative images of the cirrhotic liver at (A) 2hrs and (B) 6hrs after fractional laser ablation. At both timepoints, there is clearly reduced oxygen saturation in the regions treated with the laser (indicated with black arrows). This is most distinct at the 2hr timepoint. Representative images of the healthy liver at (C) 2hrs and (D) 6hrs after fractional laser ablation. Neither timepoint shows a noticeable change in oxygen saturation in the laser treated regions. (n=4 per timepoint)

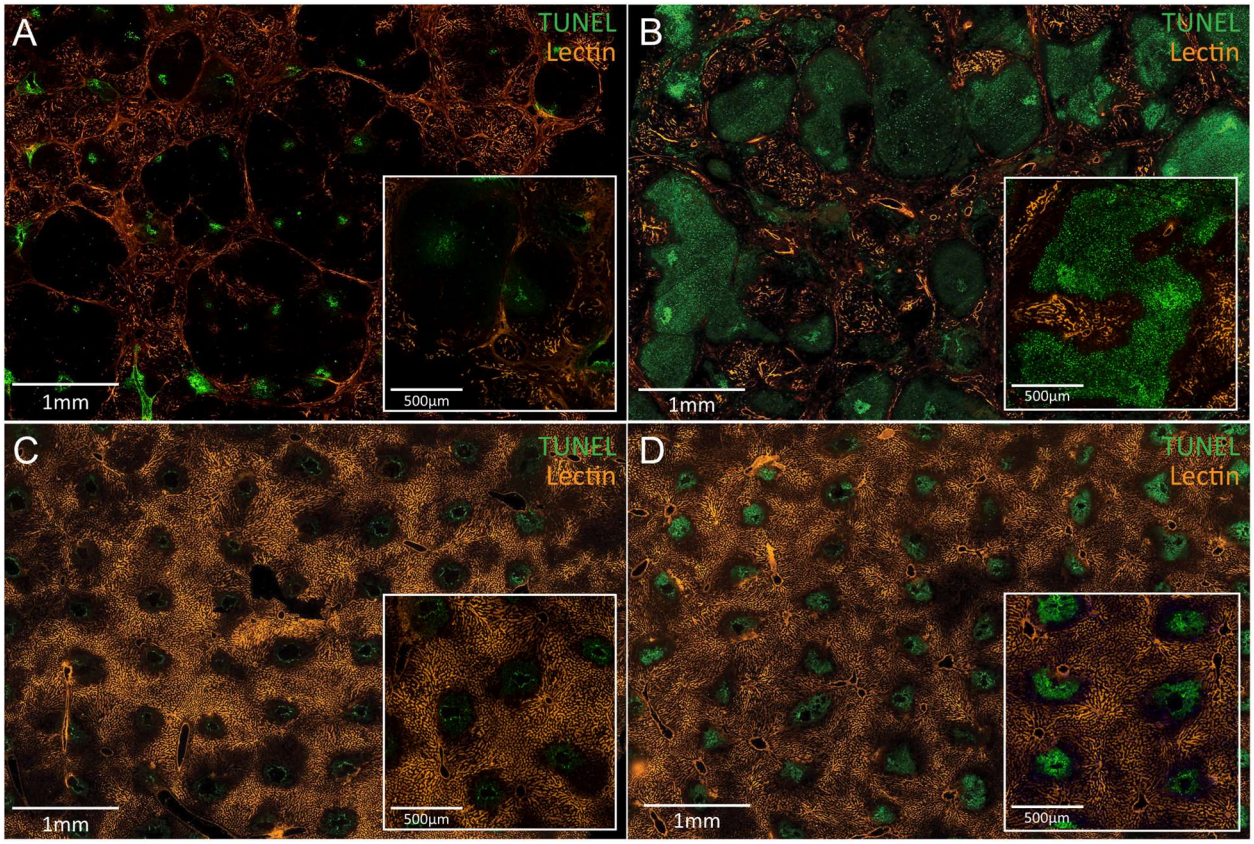

Figure 2-9: TUNEL and tomato lectin perfusion staining. Representative images of the cirrhotic liver at (A) 2hrs and (B) 6hrs after fractional laser ablation. At 2hrs, the injuries are still small and uniform, but many nodules are either partially or entirely not perfused. At 6hrs, the enlarged and heterogenous injuries have developed. The injuries align with the unperfused regions of tissue. Representative images of the healthy liver at (C) 2hrs and (D) 6hrs after fractional laser ablation. At both timepoints, the tissue surrounding the microinjuries remains perfused. (n=4 per timepoint)

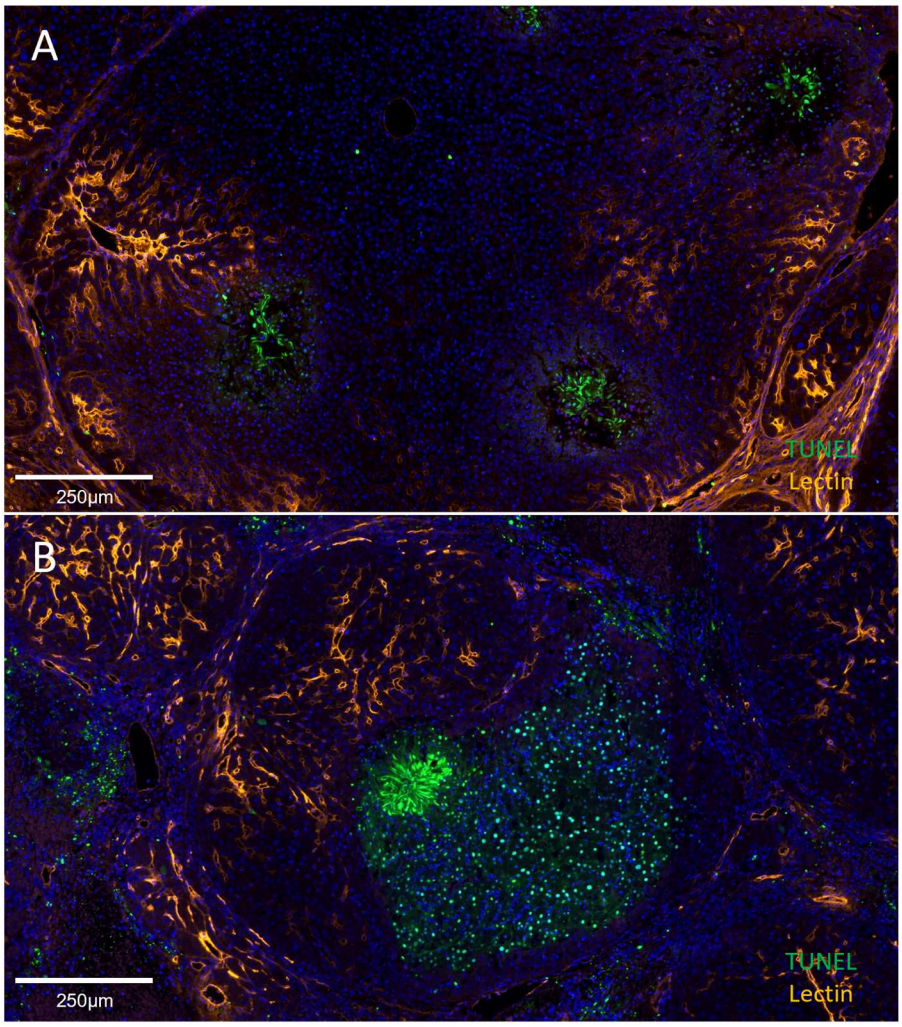

Figure 2-10: Higher magnification TUNEL and tomato lectin perfusion staining at (A) 2hrs and (B) 6hrs after fractional laser ablation with DAPI counterstain. (A) Small regions of the nodule are perfused, but the majority is not. Cell death is limited to the regions directly ablated by the laser. (B) At 6hrs, the zone of cell death fills the unperfused region of the nodule. The perfused region has no TUNEL positive cells.

regions of cell death. The healthy liver maintained perfusion between the individual laser injuries (**Figure 2-10 C, D**). An unablated reference image is provided in **Appendix Figure A-6**.

A summary of the timeline of the response to microinjuries in the healthy and cirrhotic liver is provided in **Figure 2-11**.

2.5 Discussion

In this chapter, we aimed to characterize the tissue response to fractional laser-induced microinjuries in the healthy and cirrhotic liver to determine whether microinjury ablation can be used to induce scar remodeling in the liver. This technique relies on creating small, finely controlled microinjuries to stimulate remodeling; however, our results showed that the cirrhotic liver instead developed enlarged and heterogeneous injuries. Using RNAseq, hypoxia imaging, and perfusion studies, we have shown that this unexpected pattern of injury is the result of increased susceptibility to ischemia from microvascular damage in the cirrhotic liver.

2.5.1 Ischemic Susceptibility and the Microvasculature

The liver microvasculature is an essential component of cirrhosis. Liver fibrosis develops through repeated microvascular injuries that cause large regions of hepatocytes to die and be replaced by scar tissue in a process termed parenchymal extinction[7, 121]. This progresses over time to the characteristic nodular architecture with the formation of an extensive network of perinodular vessels within the septa[122, 123]. These vessels include intrahepatic shunts that allow blood to bypass the parenchyma[124, 125]. Capillarization of sinusoids and perisinusoidal fibrosis impair oxygen delivery to hepatocytes, while vascular remodeling and endothelial dysfunction increase intrahepatic resistance and further limit perfusion[6, 126-129]. All these factors combine to create a hypoxic environment that makes the cirrhotic

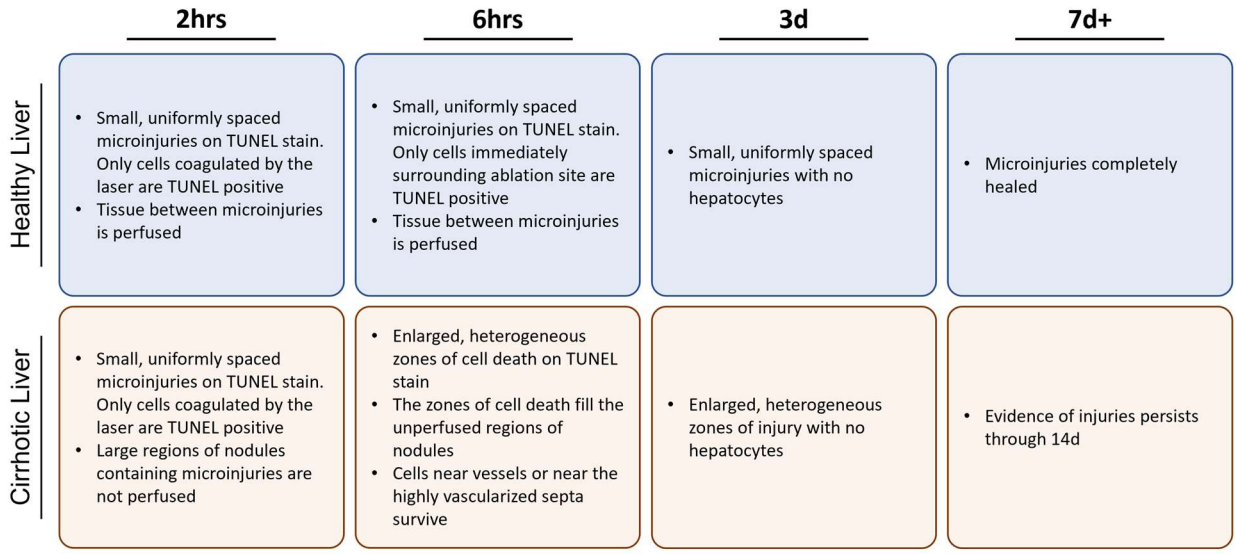

Figure 2-11: Summary timeline of the response to microinjuries in the healthy and cirrhotic liver.

liver more susceptible to ischemic injury in the event of reduced blood flow (e.g., ischemic hepatitis[130]). It is important to note that this is distinct from the ischemic susceptibility demonstrated here. Our results show that a nodule is susceptible to an obstruction at the microvascular level (i.e., a laser microinjury) broadly disrupting perfusion.

The ability of a vascular network to maintain perfusion after an obstruction is determined by the extent of collateralization and intra-tree anastomoses[131]. These are anastomoses between arterioles that normally have little to no flow across them. Obstruction causes pressure to drop in the affected arteriole, allowing blood to flow through the anastomosis and maintain perfusion[131, 132]. These connections can occur between arterial trees (collaterals) or within the same tree (intra-tree anastomoses), though they serve the same role in the event of obstruction[131, 133]. In this study, vascular perfusion was maintained post-injury in the healthy liver, indicating sufficient connections to compensate for the damage to the vascular network. In the cirrhotic liver, the changes in the vasculature that occur during the progression of cirrhosis – potentially including changes in collateralization – appear to have significantly reduced the ability to maintain perfusion after a disruption.

In addition, the pattern of injury observed in the cirrhotic liver after laser treatment matches some of the features of the nodule microvasculature. Cells at the edges of the nodule survive even when all sinusoids are not perfused because of the perinodular vasculature, and injuries spreading only within a nodule is consistent with the microvascular network being separate from neighboring nodules[134]. The heterogeneity of the injury pattern may reflect differing placement of the microinjury within the microvascular network. If the microinjury hits a critical branching point then perfusion throughout the nodule may be impacted (e.g., **Figure 2-6 A**), but if it hits a part of the network with few downstream branches – or where downstream tissue can be fed by a collateral pathway – then the impact would be less severe (e.g., **Figure 2-6 C, D**).

2.5.2 Compartment Syndrome

Compartment syndrome could also play a role in these ischemic injuries. Compartment syndrome is most commonly seen in muscle, where the parenchyma is divided into compartments by inelastic fascia. Increased pressure within a compartment, e.g. due to hemorrhage, can collapse the microvasculature to prevent perfusion and cause ischemic injury[135]. Under this hypothesis, hemorrhage from the microinjury increases the pressure within the compartment formed by the septa. In compartment syndrome, capillaries collapse when the compartment pressure exceeds the perfusion pressure. It is unlikely that either perfusion pressure or compartment pressure to one side of a microinjury would be significantly different from the other, so this explanation alone does not account for cases where perfusion was restricted in one direction extending from the microinjury (e.g., **Figure 2-6 D**), which can be more easily explained by a disruption to the microvascular network obstructing flow to downstream branches. However, in some nodules the ischemic injury may result from a combination of direct disruption of the microvascular network and compression of the remaining microvasculature by subsequent hemorrhage. This effect would not be seen in the healthy liver because the parenchyma is not compartmentalized, so excess fluid is more free to flow interstitially. Interestingly, a compartment syndrome-like effect has been proposed as a mechanism for cirrhosis pathogenesis[136]. This model involves a feedback loop of congestion, ischemia, and parenchymal extinction, leading to further congestion. It was suggested that the compartmentalization in this case arises from a nested cone angioarchitecture, where each cone is drained by a branch of the hepatic vein, and there is little collateral circulation between cones. However, they speculated that this effect would not be observed in animal models of cirrhosis because of differences in the hepatic venous tree.

2.5.3 Relevance of Ischemic Susceptibility Findings Beyond Microinjury Treatment

Hypoxic injury is an important topic in cirrhosis. The cirrhotic liver is more susceptible to a number of ischemic conditions than the healthy liver, such as ischemia-reperfusion injury during transplantation [137] or ischemic hepatitis from congestive heart failure[130]. These types of ischemic injuries are related to pre-existing hypoxia and hepatocellular dysfunction rather than obstruction at the microvascular level. However, there are other ischemic conditions that do involve liver microvascular obstruction, such as sinusoidal obstruction syndrome (SOS). SOS has various causes, including hematopoietic stem cell transplantation and chemotherapy toxicity. It involves damage to the sinusoid endothelium, which causes randomly dispersed plugs of erythrocytes that obstruct blood flow[138]. Our findings suggest that SOS would cause much greater tissue damage in the setting of cirrhosis, not only due to pre-existing hypoxia but also because the obstructions would disrupt perfusion to a larger tissue volume. A similar effect would be seen with microinfarctions in the liver, which can be caused by cirrhotic coagulopathy[139].

2.5.4 Fractional Laser Causes Negligible Bulk Heating

It is worth noting that the exacerbated injuries were not a result of heat. It is relatively straightforward to mathematically model the temperature change around a microinjury. The equation for thermal diffusion from a pulsed laser is[140]:

$$T(r,t) = T_{max}\left(\frac{t_0}{t}\right)^{3/2} exp\left(-\frac{r^2}{4Dt}\right)$$

where r is distance from the center of the laser pulse, t is time, t_0 is the laser pulse width, D is thermal diffusivity, and T_{max} is the maximum initial temperature increase induced by the laser. Using this model, the peak temperature increase 100μm from the edge of the

coagulated tissue is 2.20°C, and at 200μm the peak temperature increase is just 0.57°C. A precise threshold for thermal damage is difficult to determine due to the influence of both intensity and duration, varying tissue sensitivities, and heat stress processes activated over a range of temperatures[141]. One method for quantifying thermal damage is cumulative equivalent minutes at 43°C (CEM43), where any heat dose is converted to an equivalent number of minutes at a tissue temperature of 43°C[142]. 9 CEM43 (i.e., 9 minutes at a temperature of 43°C, a temperature increase of approximately 6°C) has been suggested as a general threshold for safe thermal exposure, and the lowest reported CEM43 value for thermal damage in the liver is 9.9[142-144]. Given the peak temperature increase 100μm from the coagulated tissue is estimated to be just 2.20°C for a duration measured in milliseconds, the bulk heating effect of the laser is negligible.

2.5.5 Future Directions

The exacerbated injuries limit the applicability of the current fractional laser tool for inducing scar remodeling in cirrhosis. Alterations to the fractional laser tool could help avoid this issue. Femtosecond lasers can create extremely small injuries, potentially on the size of a single cell. Such a laser would have limited treatment depth, but repetitive pulse stacking with precise targeting may provide sufficient treatment volume. A similar effect could be achieved by focusing the laser to a smaller spot size. A balance would have to be struck between creating small enough injuries to avoid significantly disrupting the microvascular network while still eliciting a sufficiently strong response to drive scar remodeling.

There are numerous fibrotic conditions occurring throughout the body that would not have the same limitations we discovered in the liver. For example, a fractional laser tool combined with an endoscope may be a promising option for the treatment of gastrointestinal strictures – fibrous bands that can progressively contract over time and

cause blockages. Another potential use case is pulmonary fibrosis. Similar to cirrhosis, transplantation is the only curative treatment option for pulmonary fibrosis. It may be possible to combine a fractional laser with a bronchoscope to perform minimally invasive microinjury treatment. There is a multitude of fibrotic conditions occurring throughout the body, many of which have high morbidity and limited treatment options. The remarkable results of microinjury treatment in the skin warrant further investigation for other applications.

Our study also introduces a novel controlled method for creating microvascular injuries which can be used to examine functional consequences of the cirrhotic vasculature that would be difficult to obtain through imaging studies or vascular casts alone. Future studies could investigate the response to microinjury at various stages of fibrosis. Shunting vessels have been shown to develop as early as 4 weeks after CCl_4 exposure[125], when fibrosis is minimal. Investigating how the injury response to the laser changes over the various liver fibrosis states and at which point the ischemic susceptibility first appears could provide useful information about the time course of vascular derangement. It would also be interesting to investigate the response to fractional laser ablation during the regression of fibrosis. Certain animal models of cirrhosis exhibit reversible fibrosis, even after cirrhosis is established. However, the vascular changes are not reversible. Studying the response to microinjuries during regression of the septa may provide information about how perfusion changes over time and whether the ischemic susceptibility remains permanently.

2.5.6 Summary

We have demonstrated that fractional laser ablation is well tolerated in the healthy liver but causes enlarged and heterogeneous zones of cell death in the cirrhotic liver. These exacerbated injuries result from disrupted perfusion of the cirrhotic nodule. The

increased susceptibility to ischemia from microvascular damage is likely related to the vascular derangements that occur during the progression of liver fibrosis to cirrhosis. Modifications to the fractional laser tool, such as using a femtosecond laser or reducing the spot size, may prevent large disruptions of perfusion and enable further development of a laser-induced microinjury treatment for cirrhosis.

Chapter 3

Lytic Perturbation via Interstitial Infusion of Purified Collagenase Clostridium Histolyticum

3.1 Introduction

Another scar treatment method commonly used in dermatology is direct injection. Compared to other drug delivery methods, direct injection has the benefit of mostly confining the drug to the desired site of activity, allowing the use of higher doses without incurring systemic side effects. It also bypasses the challenge of getting the treatment to reach the desired location. Dermatologists routinely use injections of corticosteroids[145] to treat skin scars, but a number of other therapeutics are delivered with this method as well, including fat[146, 147], stem cells[148], and collagenase. Direct injection of collagenase

(specifically a purified collagenase clostridium histolyticum, CCH) has been successfully developed as a treatment for Dupuytren's Contracture (DC)[149], a localized fibrotic condition in the palmar fascia that causes forced flexion of one or more finger. DC shares a number of features with liver fibrosis, including excess collagen production, increased crosslinking, hypoxia, vascularization, and myofibroblast differentiation, proliferation and contraction[7, 9, 31, 150]. This disease progresses from a nodule – characterized by inflammation, myofibroblast proliferation, and matrix deposition – to a cord – which is hypocellular, crosslinked, and more similar histologically to mature scar tissue[151, 152]. It has also been shown that the stiffness and tension in the contracture cause reduced MMP and increased TIMP expression[153], again demonstrating the feedback loop between stiffness and fibrosis. The treatment typically involves an injection of CCH followed by manipulation of the affected fingers 1 day later to rupture the cord[149, 154]. Although the histologic features of DC would make the affected tissue resistant to enzymatic degradation – much like the septa in cirrhosis – these results show that a single concentrated dose can overcome that obstacle. There is a 35% 3 year recurrence rate[155], but for the majority of patients, rupturing the cord (and therefore removing the mechanical stimulus) leads to resolution. Purified CCH injection has also been successfully used in Peyronie's disease, a similar fibrotic condition occurring in the penis[156, 157].

3.1.1 Collagenase Clostridium Histolyticum (CCH)

CCH is a mixture of enzymes secreted by the clostridium histolyticum species of bacteria. Crude and partially purified preparations of CCH are routinely used for tissue digestion during isolation of primary cells. Crude CCH is a poorly defined mixture of enzymes including potent collagenases and a variety of other enzymes, such as clostripain and neutral proteases, which broadly digest non-collagenous proteins as well.

The commercial version of CCH used for DC is purified for two collagenase enzymes[158]. This purified mixture was reported to have strong activity against collagen types I and III[158], the two primary excess matrix components in both DC[151, 159] and cirrhosis[160]. Furthermore, the histologic features of the DC cord – namely densely packed and highly crosslinked collagen – should make it resistant to enzymatic degradation, similar to the fibrous septa in cirrhosis[108, 161]. The success of CCH treatment in DC shows that these potent enzymes can overcome this obstacle.

3.1.2 Prior Work with CCH for Liver Fibrosis

Expression of matrix degrading enzymes is a common preclinical metric for new drugs for liver fibrosis, and there are also a number of papers describing gene therapies for various MMPs[162-165]. However, the delivery of an exogenous matrix-degrading enzyme has not been thoroughly investigated. Jin *et al*, 2005[166] used a rabbit model of cirrhosis to perform biweekly injections of crude CCH through a portal vein catheter for 6-12 weeks. This study reported only 45% survival, which the authors attributed primarily to infection and surgical complications. However, it seems plausible that the presence of broad proteases in the infused enzyme mixture may have also contributed to the high mortality. Despite these complications, they were able to demonstrate significant histological improvements in the liver. El-Safy *et al*, 2020[167] used a mouse model of moderate liver fibrosis to compare triweekly intravenous injection of crude CCH either free or coupled to chitosan nanoparticles that bind collagen. 100% of animals receiving free CCH died before the second dose, albeit with a sample size of 2, while 100% of animals receiving the optimal nanoparticle formulation completed the 3-week schedule. The authors reported moderate histological improvements in the CCH nanoparticle mice compared to controls. In both cases, a crude CCH mixture was used, and it was injected directly into the bloodstream. To our knowledge, ours is the first study to investigate interstitial infusion of collagenase in the liver.

3.2 Methods

3.2.1 Crude and Purified CCH Analysis

Molecular weight analysis of the crude (Sigma Aldrich #C1639) and purified CCH (VitaCyte #001-1050) was performed using the capillary Western total protein assay[168] (Jess, ProteinSimple). Sample preparation was done as follows: in brief, protein was diluted to appropriate concentrations (0.5mg/mL for crude CCH, 0.03125mg/mL for purified CCH), mixed with a fluorescent standard (EZ Standard Pack # PS-ST01EZ), and boiled for 5 minutes at 95^{o}C. Samples were loaded onto respective wells in the cartridge. Loading of capillary cartridges with 12-230 kDa separation (ProteinSimple SM-W004-1) was performed according to the manufacturer's protocol (Total protein detection module for Chemiluminescence #DM-TP01). Run was set up using the instrument software (Compass for SW). Jess Total Protein data were analyzed using the Compass for SW software, Version 6.1.0, Build ID: 0111, Revision ID 7214faa from ProteinSimple. Total protein is depicted in graph form and lane view, which resembles a traditional western blot staining for total protein.

To assess substrate specificity, enzyme activity was measured against type I collagen and casein. Degradation of type I collagen was measured with the EnzChek Collagenase Assay kit (Thermofisher #E12055) with quenched fluorescent type I collagen (Thermofisher #D12060) according to manufacturer instructions. Degradation of casein was measured with the Pierce Colorimetric Protease Assay kit (ThermoFisher #23263) according to manufacturer instructions.

3.2.2 Animals

All animal work was approved by the Massachusetts General Hospital Institutional Animal Care and Use Committee and performed in accordance with all relevant

guidelines. Male C57BL/6 mice were purchased from Charles River Laboratories. Animals were housed in a controlled environment with food and water ad libitum. To induce cirrhosis, mice received intraperitoneal injections of thioacetamide three times per week for 15 weeks. The dose escalated from 50mg/kg for the first 2 doses, 100mg/kg for doses 3-5, 200mg/kg for doses 6-10, 300mg/kg for doses 11-15, then 400mg/kg until the end of the dosing schedule as established previously[169]. Animals underwent the infusion procedure 1 week after the final dose to allow washout of the chemical.

3.2.3 Ex vivo collagen degradation

Liver samples from cirrhotic mice were embedded in OCT, snap frozen on dry ice, and cut to 12μm sections in a cryostat. Sections were then incubated with 0.5μg/mL purified CCH in normal saline supplemented with 0.3mg/mL calcium chloride dihydrate (Sigma Aldrich #C7902). Control sections were incubated with normal saline supplemented with 0.3mg/mL calcium chloride dihydrate. After 1hr, 2hr, 3hr, 4hr, or 5hr, sections were rinsed with normal saline, fixed with fresh formaldehyde, and stained with picrosirius red as described below.

3.2.4 Surgical Protocol & Intrahepatic Infusion

Animals were anesthetized with isoflurane and prepared for surgery by clipping fur on the abdomen and disinfecting with 10% povidone-iodine. A laparotomy was performed with a short midline incision beginning from the xyphoid. The medial lobe of the liver was exposed using sterile swabs. The abdomen was then covered with a sterile Tegaderm film to protect the liver and limit water loss.

For the infusion, a 28G needle was connected to a 1mL syringe with a sterile silicone tube. For biodistribution experiments the syringe was filled with sterile-filtered fluorescent dextran tracer (ThermoFisher, #D1864 and #D1830) in normal saline at a concentration of

2mg/mL. For efficacy experiments, the syringe was filled with sterile-filtered purified CCH at varying concentration in normal saline supplemented with 0.3mg/mL calcium chloride dihydrate. Control animals for biodistribution experiments received sterile-filtered normal saline, and control animals for efficacy experiments received sterile-filtered normal saline supplemented with 0.3mg/mL calcium chloride dihydrate. The needle was inserted several millimeters into the medial lobe. Using a syringe pump, interstitial infusion was performed at a rate of 100μL/hr for 1 hour.

After the infusion, the muscle layer was closed with 5-0 absorbable sutures and the skin was closed with wound clips. For biodistribution experiments, animals were euthanized via cardiac puncture 1hr, 6hr, 1d, 2d, and 3d after the infusion. For efficacy experiments, animals were euthanized 1d and 5d after the infusion.

Blood collected at the time of euthanasia was left to coagulate at room temp for 30min-1hr, then centrifuged at 2000g for 15min to separate the serum. Serum samples were then stored at -20C until sent for analysis of AST, ALT, and creatinine levels.

3.2.5 Biodistribution

70kDa dextran conjugated to Texas Red (ThermoFisher, #D1864) was used to characterize the distribution of a macromolecule delivered via interstitial infusion in the liver. Distribution through the liver during infusion was measured with an IVIS Lumina Series III in vivo fluorescent imaging system (Caliper Life Sciences) at 10-minute intervals. The IVIS was also used to image fluorescence of the liver, kidneys, lungs, heart, and spleen after 1hr of infusion.

Lysine-fixable 70kDa dextran conjugated to Texas Red (ThermoFisher, #D1830) was used for histological assessment of the tracer distribution. After euthanasia, the medial and left lobes of the liver, as well as the kidneys and lungs, were embedded in OCT and snap frozen on dry ice. 10μm sections were cut in a cryostat and fixed with formalin. Slides

were imaged with an epifluorescence microscope and mean fluorescence intensity was quantified in ImageJ. Tissue from mice infused with saline was used to establish baseline fluorescence intensity in each organ.

3.2.6 Histology & Immunostaining

Tissue for histology was collected at the time of euthanasia. Samples of the medial and left lobes of the liver were embedded in OCT and snap frozen on dry ice. For picrosirius red staining, 12μm sections were cut in a cryostat and air dried for 30min. Sections were then rehydrated in an ethanol series and fixed with fresh formaldehyde. The slides were stained with picrosirius red for 30min, washed twice with acidified water, then dehydrated in an ethanol series, cleared in xylene, and coverslipped with Permount mounting medium (Fisher Scientific). For immunofluorescence staining, 5μm sections were cut in a cryostat. We used primary antibodies against alpha-smooth muscle actin (SMA, diluted 1:500; Abcam, #ab124964), phosphorylated YAP (diluted 1:400; Cell Signaling, #13008S), TAZ (diluted 1:100; MyBioSource, #MBS9613324), Ki-67 (diluted 1:400; Abcam, #ab15580), and HNF4a (diluted 1:100; Abcam, #ab41898). For staining with the HNF4a antibody from a mouse host, sections were additionally blocked with Anti-Mouse IgG (diluted 1:10; Abcam, # ab6668). Sections were then stained with Alexa Fluor 594 conjugated secondary antibody (Thermo Fisher Scientific) and DAPI (Thermo Fisher Scientific). Picrosirius red slides were imaged with a Nanozoomer 2.0 HT slide scanner (Hamamatsu, Hamamatsu City, Japan). Immunofluorescence slides were imaged with an epifluorescence microscope.

3.2.7 Image Quantification

For fibrosis assessment, 5x magnification images across the entire section were exported from the whole-slide scans captured with the Nanozoomer. All image names were then

masked and randomly ordered with the Blind Analysis tool in ImageJ. Collagen proportionate area (CPA) was calculated in ImageJ[170, 171].

3.3 Results

3.3.1 Characterization of Purified and Crude CCH

To ensure purity of the enzyme, molecular weight analysis was performed for both crude CCH and purified CCH with the capillary Western total protein assay (**Figure 3-1**). As expected, the crude CCH preparation demonstrated multiple peaks at a variety of molecular weights. The purified CCH showed one strong, distinct peak around 116 kDa, indicating high purity. A small peak was also observed around 230 kDa, however this peak was present at a similar level across a serial dilution of the purified CCH (**Error! Reference source not found.**), likely indicating this is an artifact rather than impurity in the CCH preparation.

To further assess purity as well as substrate specificity, enzyme activity was measured against type I collagen and casein, a protein easily degraded by the mixture of proteases in crude CCH (**Figure 3-2**). Crude CCH showed high casein degradation, while no casein degradation was observed with purified CCH at any concentration. Both mixtures efficiently degraded type I collagen, although the purified CCH exerted a greater rate of degradation.

The enzyme mixtures were then tested on frozen sections of cirrhotic mice livers to quantify collagen degradation ex vivo. Incubating sections with crude CCH led to severe

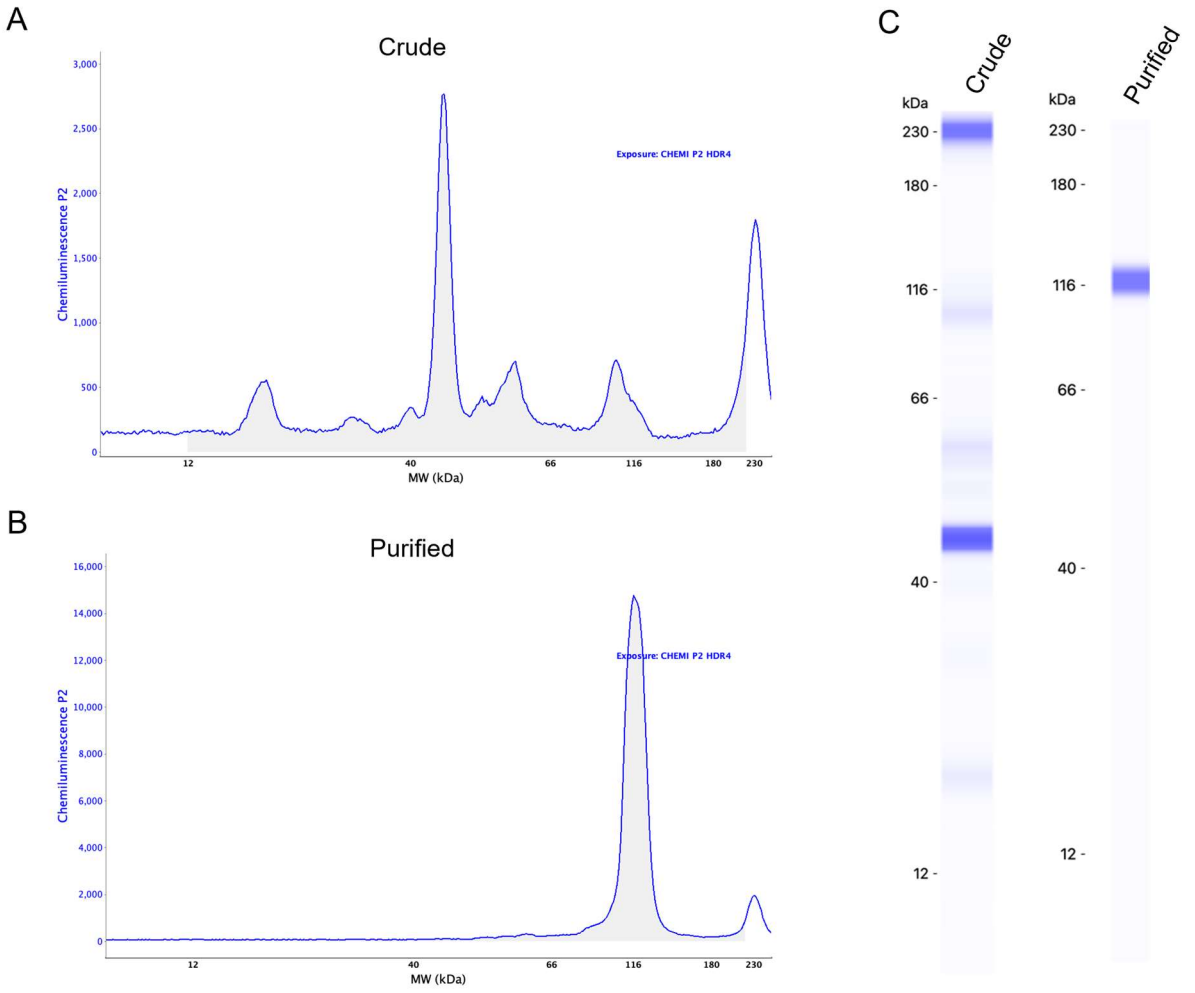

Figure 3-1: Molecular weight analysis of crude and purified CCH. (A,B) Molecular weight analysis of crude and purified CCH, respectively. Crude CCH has components at a variety of molecular weights, while the purified CCH only has one distinct peak at 116 kDa. (C) Western blot representation of the same data presented in A & B.

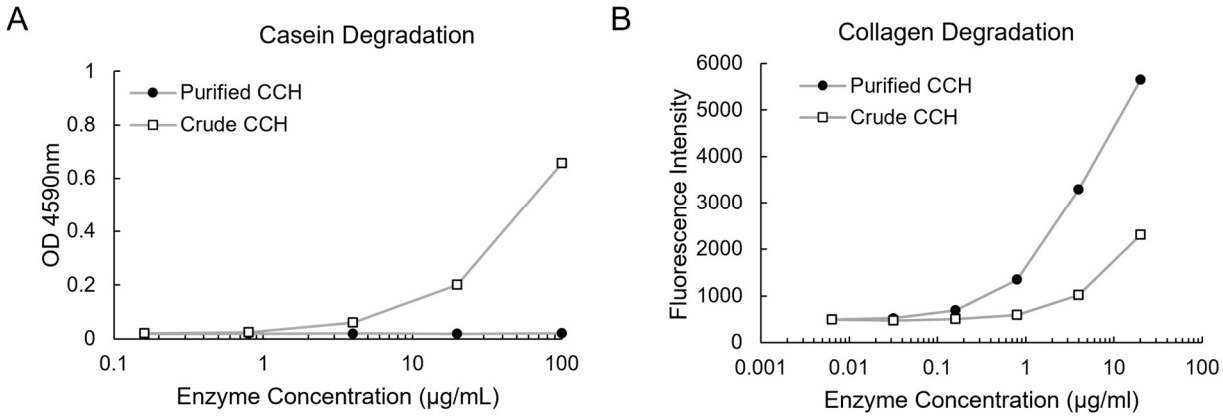

Figure 3-2: Substrate specificity of crude and purified CCH. (A) Enzyme activity against casein substrate. Crude CCH degrades casein rapidly due to the many proteases it contains. Purified CCH shows no degradation of casein. (B) Enzyme activity against type I collagen. Both crude and purified CCH efficiently degrade type I collagen, though purified CCH is more potent.

tissue dissociation, causing sections to fall apart during staining. Sections incubated with purified CCH showed no signs of tissue dissociation and had significantly reduced collagen proportionate area within 3hrs (**Figure 3-3**).

These results verify that the purified CCH is not significantly contaminated with non-collagenase enzymes, which may cause non-collagenous tissue damage and cell toxicity in vivo, and that it is capable of rapid degradation of type I collagen without broadly disrupting tissue integrity.

3.3.2 Biodistribution after Interstitial Infusion in the Liver

We next used a fluorescently labelled dextran to design an appropriate infusion protocol and determine how the enzyme will spread after infusion.

Using live imaging, we found that the entire liver was fluorescent after 60min at an infusion rate of 0.1mL/hr (**Figure 3-4**). We also used this system to image key organs after 1hr infusion (**Figure 3-5**). We observed strong fluorescence throughout the liver as well as the kidneys, with no significant signal in the lungs, heart, or spleen. These results show that the entire liver receives the infused material, but a significant amount also enters the bloodstream before being cleared out by the kidneys. It should be noted that clearance of CCH through the kidneys likely differs significantly from dextran, as will be discussed in section 3.4.1. Despite entering the blood, no detectible amount of dextran infiltrated the other organs. 1hr was determined to be the optimal infusion time as it minimizes off target exposure while still covering the entire liver.

Biodistribution after interstitial infusion in the liver was further characterized in mice up to 3 days after the infusion surgery. Fluorescence remained elevated and relatively stable in both the medial lobe of the liver, where the needle had been inserted, as well as the left lobe through 2 days after infusion (**Figure 3-6 A, B**). Similar results were seen in the renal cortex of the kidneys, though with weaker fluorescence intensity (**Figure 3-6 C**). By day

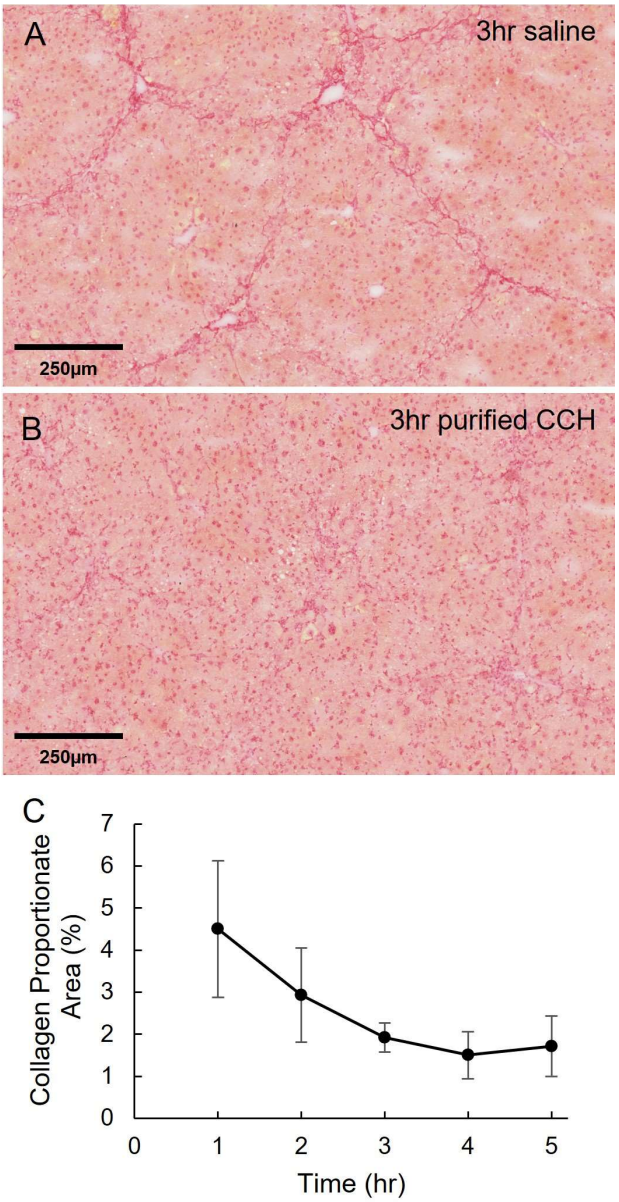

Figure 3-3: ex vivo collagen degradation in cirrhotic liver sections. (A) Sections incubated with saline show distinct fibrous bands. (B) After 3 hrs with 0.5µg/mL purified CCH, the fibrous bands are nearly completely dissolved, but there is no bulk tissue dissociation as found with crude CCH. (C) Quantified reduction in collagen over time with purified CCH shows rapid degradation. (n=3 per timepoint)

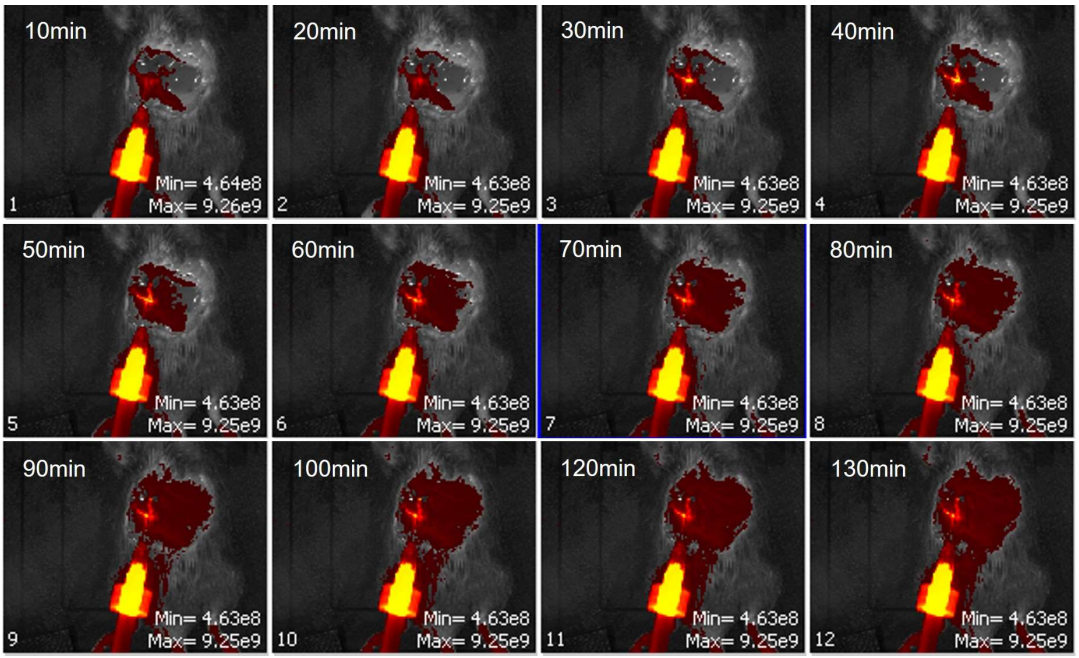

Figure 3-4: Live imaging of fluorescent dextran delivered via interstitial infusion of the liver. Fluorescent dextran is detected throughout the liver around 60mins of infusion. Beyond this time, the fluorescent signal in the liver is fairly consistent, while fluorescence of surrounding tissues gradually increases.

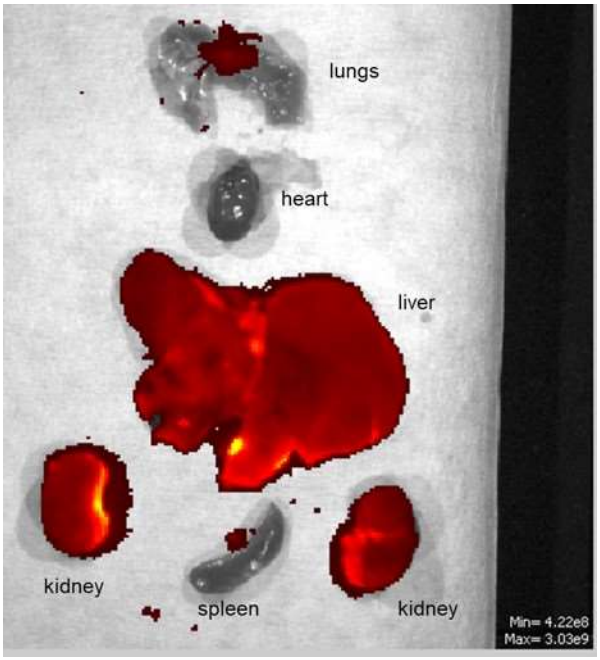

Figure 3-5: Whole organ imaging after interstitial infusion of fluorescent dextran in the liver for 60min. All lobes of the liver have a strong fluorescent signal, as well as both kidneys. The lungs, heart, and spleen show no significant signal.

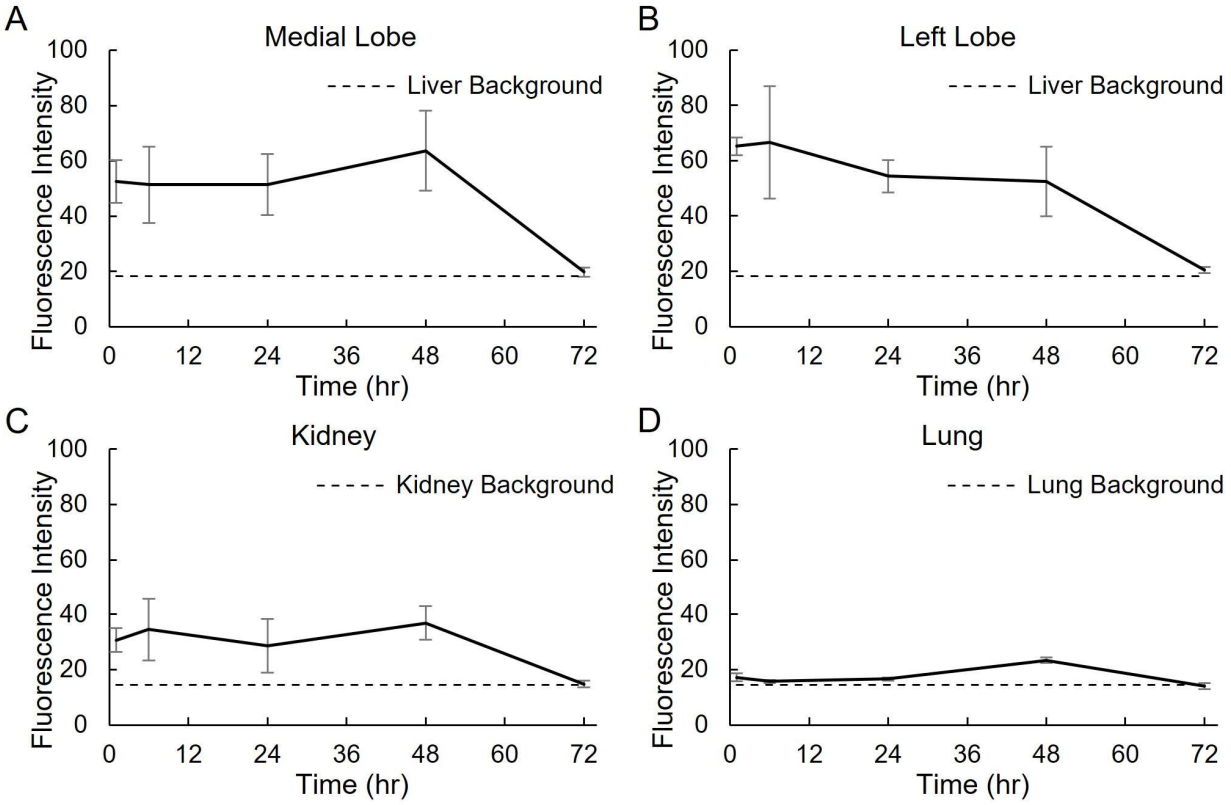
A
Medial Lobe
Liver Background
Fluorescence Intensity
Time (hr)
B
Left Lobe
Liver Background
Fluorescence Intensity
Time (hr)
C
Kidney
Kidney Background
Fluorescence Intensity
Time (hr)
D
Lung
Lung Background
Fluorescence Intensity
Time (hr)

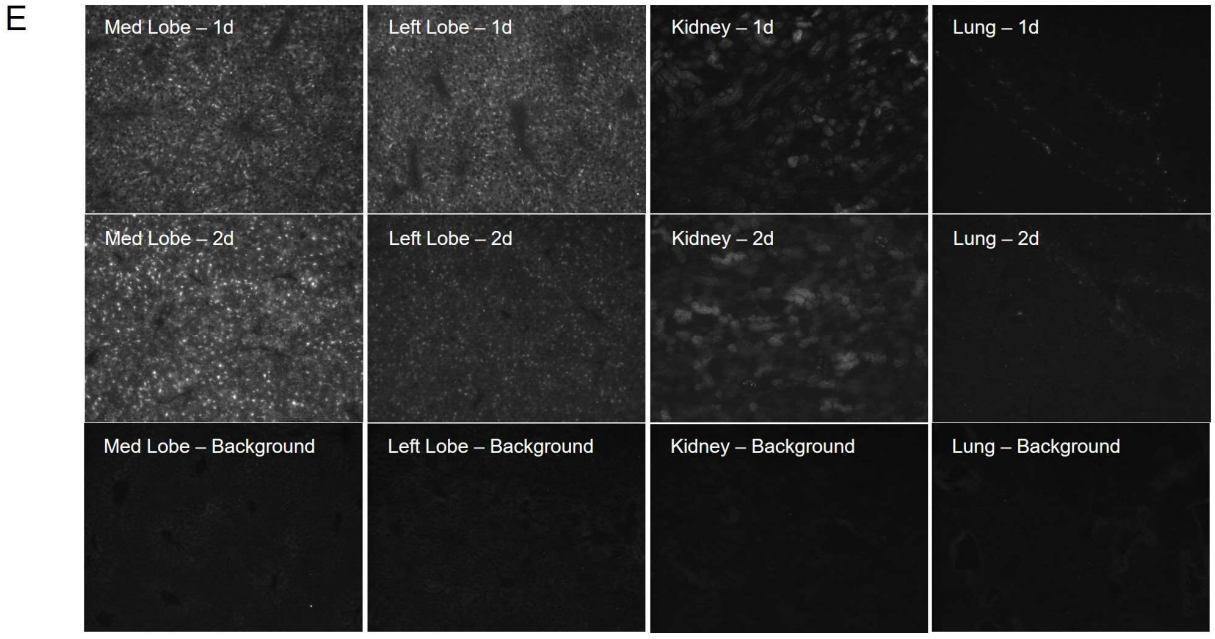
E
Med Lobe – 1d
Left Lobe – 1d
Kidney – 1d
Lung – 1d
Med Lobe – 2d
Left Lobe – 2d
Kidney – 2d
Lung – 2d
Med Lobe – Background
Left Lobe – Background
Kidney – Background
Lung – Background

Figure 3-6: Quantified fluorescence after 60min interstitial infusion of fluorescent dextran in the liver. (A) Fluorescence in the medial lobe of the liver (the lobe where the needle was inserted) showed consistently elevated fluorescence through 2 days after infusion. By 3 days, fluorescence returned to the background level. (B) The left lobe of the liver, which was not directly infused, showed similar results. (C) Fluorescence was also detected in the renal cortex of the kidneys. This signal followed a similar trend to the liver at lower intensity, with stable elevation through 2 days and returning to the background level by day 3. (D) Fluorescence of the lungs remained near background at all timepoints, though a slight but statistically significant increase was noted at day 2. (E) Representative images of dextran fluorescence. (n=3 per timepoint)

3, fluorescence of both organs returned to background level. Fluorescence of the lungs remained near background at all timepoints, although a slight but statistically significant increase over background was observed at 2 days.

3.3.3 Purified CCH in vivo Toxicity & Efficacy

Preliminary in vivo tests were performed on mice maintained under anesthesia for up to 5hrs after infusion to determine an appropriate concentration of the purified CCH. Through these experiments we found that concentrations greater than 1.25mg/mL were lethal. However, in our first experiments where anesthesia was ended after the 1hr infusion period we found that mice that received concentrations of 0.25mg/mL or greater died shortly after withdrawal of anesthesia – despite these doses being viable in animals maintained under anesthesia for 5hrs after infusion until euthanasia. A concentration of 0.1mg/mL was chosen for the remaining experiments.

Based on the biodistribution data, potential risk targets for toxicity were the liver and kidneys. Serum markers of liver injury (AST, ALT) and kidney injury (creatinine) were measured at 1d and 5d after infusion (**Figure 3-7**). AST and ALT were mildly elevated at 1d but fell to within normal range by 5d[172]. However, both markers showed similar

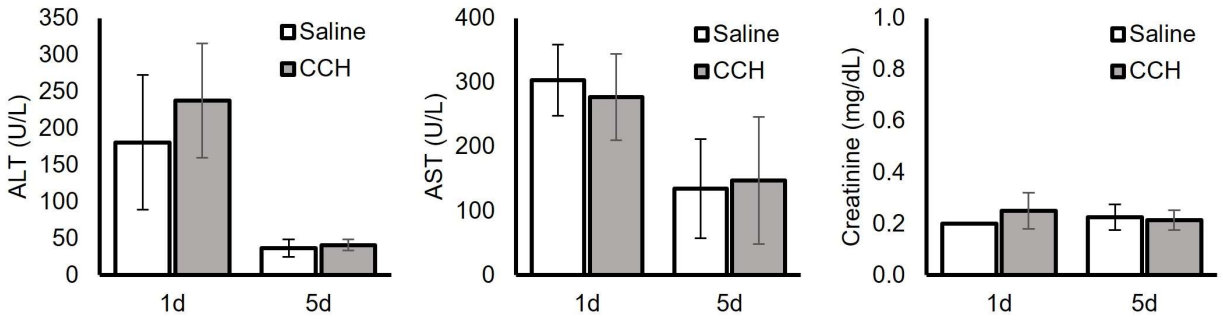

Figure 3-7: Serum injury markers at 1d and 5d after interstitial infusion of the cirrhotic liver with saline or purified CCH. Liver injury markers ALT and AST are elevated at 1d then return to within normal range by 5d. There is no significant difference between infusion with saline and purified CCH, suggesting these markers are not increased due to enzyme toxicity. Kidney injury marker creatinine is not elevated at any timepoint. Samples with creatinine below the 0.2mg/dL level of detection are not represented in this graph. (n=3 CCH and saline controls at 1d; n=4 saline controls at 5d; n=6 CCH treated mice at 5d)

elevations in mice infused with saline, suggesting this is related to liver injury from the procedure rather than the activity of the enzyme. There was no elevation in creatinine at any timepoint, indicating the enzyme does not cause acute kidney injury.

Treatment efficacy was assessed primarily by changes in fibrosis. Mice treated with purified CCH had significant reduction in hepatic collagen at the 5d timepoint (**Figure 3-8 A-C**). The same results were observed for the directly infused lobe (medial; **Figure 3-8**) and a non-infused lobe (left; **Appendix Figure B-2**) Mean CPA was reduced by 33% in CCH treated mice compared to saline controls. There was no change in SMA positive area at 5d (**Figure 3-8 D**).

Immunofluorescence staining was used to assess the cellular response to structural change in the infused lobe. There was a marginal increase in hepatocyte proliferation after CCH treatment (**Figure 3-9 A**), though it did not reach the threshold for statistical significance. No difference was observed in the mechanoregulated transcriptional co-activators YAP and TAZ (**Figure 3-9 B, C**), key effectors in the hippo pathway. These markers would be expected to decrease if tissue stiffness is reduced, however they are influenced by a variety of factors, including liver regeneration and response to injury, which may obscure stiffness-related changes at this timepoint.

3.4 Discussion

3.4.1 Biodistribution after Interstitial Infusion

Direct intrahepatic injection is a relatively common preclinical research tool used to seed cancer cells[173] and stem cells[174] in the liver. However, there is little prior work on the biodistribution of a macromolecule infused interstitially in the liver. Berraondo *et al*, 2006 tested intrahepatic injection for the delivery of an adeno-associated virus with a 50μL bolus injection[175]. They reported partial distribution within the injected lobe but not

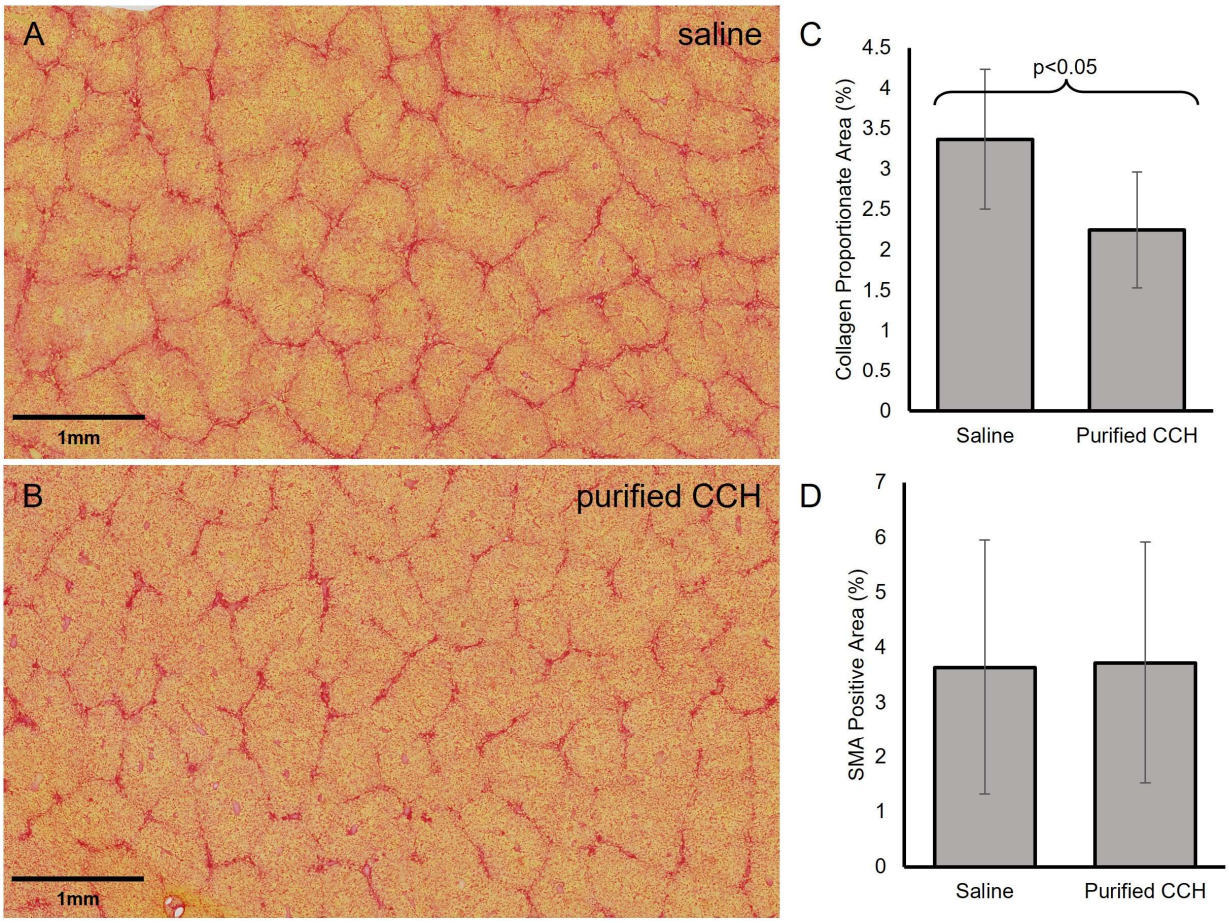

Figure 3-8: Changes in fibrosis in the infused (medial) lobe 5d after interstitial infusion of purified CCH in the cirrhotic liver. (A,B) Representative picrosirius red staining for liver samples 5d after infusion with saline or purified CCH, respectively. Fibrous bands in samples that received CCH are thinner and more disconnected. (C) Quantification of collagen in saline and CCH infused samples. Purified CCH caused a significant decrease in collagen proportionate area. (D) There was no significant change in SMA positive area between saline and CCH infused samples. (n=4 saline controls; n=6 CCH treated; p-value calculated with t-test)

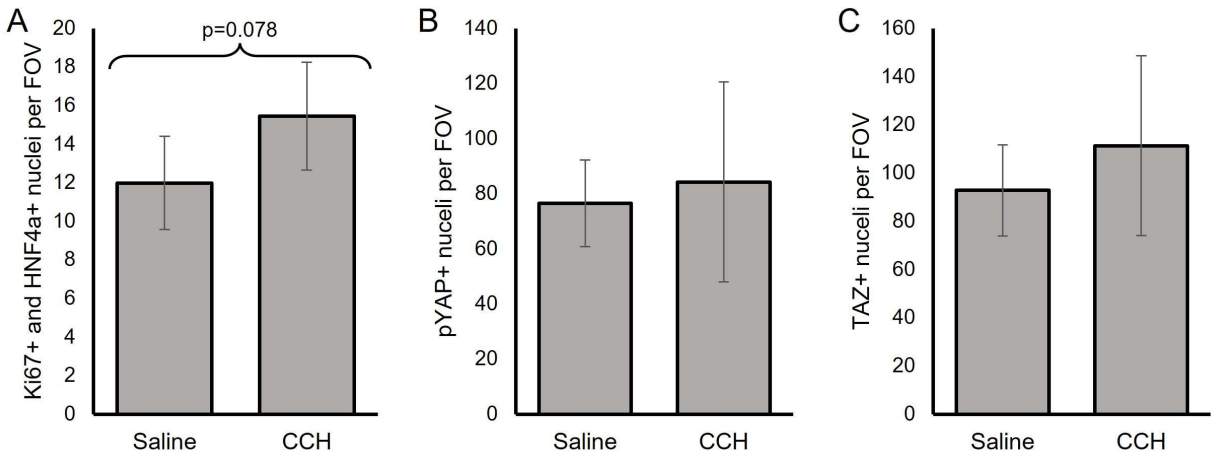

Figure 3-9: Quantified immunofluorescence markers in the infused (medial) lobe 5d after interstitial infusion with saline or purified CCH. (A) Hepatocyte proliferation measured by Ki67+/HNF4a+ nuclei. There is a marginal but not statistically significant increase after CCH infusion. (B, C) Phosphorylated YAP+ nuclei and TAZ+ nuclei, respectively. No significant difference was observed in either marker. YAP and TAZ are both effectors in the hippo signaling pathway. Nuclear localization of these markers is driven by a complex regulatory network influenced by a variety of factors, liver regeneration and local tissue stiffness. (n=4 saline controls; n=6 CCH treated; p-value calculated with t-test)

throughout the liver. Our results show that gradual infusion of 100μL reaches the entire liver, despite only directly infusing the medial lobe. This may simply be due to the difference in volume administered, but it is also likely that the gradual infusion improves interstitial distribution. Interstitial fluid drains through terminal lymphatics in response to small changes in interstitial pressure[176, 177]. A bolus injection would cause a brief spike in local interstitial pressure around the injection site, allowing more of the injected material to drain away. An analogous effect has been reported in tumescent anesthesia, where gradual subcutaneous infusion of lidocaine dramatically reduces the plasma concentration[178]. The infusion protocol could further be refined in the future to be performed non-invasively under ultrasound guidance, rather than via laparotomy, to minimize impact on the recipient as well as enable investigation of multiple low-dose infusions over time. Repeated low-dose infusions may be clinically preferable so that the treatment can be titrated while monitoring liver function tests.

It is likely that there is also some distribution between lobes through the vasculature. The liver has a unique connection between intravascular and interstitial compartments due the fenestrated sinusoidal endothelium. This connection deteriorates in advanced disease through capillarization of sinusoids, where fenestrations are lost and matrix accumulates in the space of Disse[126]. It is unclear how much of the connection remains in this model, and whether the more severe liver scarring seen in human disease and rat models may affect the biodistribution. While in circulation, the structural collagen of the blood vessels would not typically be exposed to the CCH in the bloodstream due to the endothelial cell lining. In addition, early work with CCH demonstrated it is inhibited and cleared by alpha-2-macroglobulin, a large plasma protein that functions as a broad-spectrum protease inhibitor[179-181]. It is worth noting that alpha-2-macroglobulin is also produced by macrophages and hepatocytes, which may limit the activity of CCH within the liver[179, 182, 183].

There are several notable limitations of our dextran experiments. First, there is a relatively small difference in size between the fluorescent dextran (70kDa) and purified CCH (116kDa). Both of these sizes are large enough that the primary distribution mechanism is convection[184], so the short-term spread of these molecules is likely similar. The size differential is most relevant for the clearance through the kidneys. The fluorescent dextran is near the size threshold for glomerular filtration, though there is high variability based on shape and flexibility of the macromolecule[185, 186]. The increased size of CCH likely reduces elimination through the kidneys compared to the fluorescent dextran. Pharmacokinetics is a complicated field and there are many factors that can significantly influence clearance, e.g., charge of dextran derivatives alters rate of clearance in the liver[187]. In addition, the dextran experiments do not account for specific removal processes for proteases or bacterial proteins. Overall, the dextran experiments primarily provide useful data for the short-term biodistribution of a macromolecule delivered via interstitial infusion in the liver, rather than an indication of their clearance and how long they persist in the tissue.

Interstitial delivery offers several advantages over intravenous routes previously investigated. Direct intrahepatic delivery ensures the highest concentration of the enzyme is at the desired site of action rather than in the plasma. Furthermore, as described above, the capillarization of sinusoids in advanced disease would impair infiltration of an enzyme injected in the bloodstream; with interstitial delivery, this would serve to maintain the enzyme concentration within the liver and limit systemic spread. Recent work has also suggested rethinking many interstitial structures previously believed to be densely-packed matrix, including the extrahepatic and intrahepatic biliary tree, as open fluid-filled spaces, which may have important implications for the spread of a macromolecule delivered via interstitial infusion[188].

3.4.2 Toxicity

The results of our biodistribution and in vivo CCH experiments do not indicate any toxicity from the direct activity of the enzyme. The mild elevations in AST and ALT at 0.1mg/mL (matching elevations in saline controls), and the survival at concentrations as high as 1.25mg/mL when maintained under anesthesia suggest that the primary dose-limiting factor is not liver injury. Interestingly, it has been reported that certain anesthetic agents, including isoflurane, can be protective against sepsis and endotoxic shock. The mechanisms are not well understood, but isoflurane has been shown to enhance survival and delay systemic inflammation in murine models[189-193]. As we have shown a significant amount of the infused material enters the bloodstream, it is possible that the bacterial CCH initiates a shock response which is inhibited until the animals are taken off anesthesia. If systemic shock is occurring, it could be managed in the appropriate setting, e.g., through monitoring blood pressure and administering vasopressors. As there appears to be no liver or kidney injury from the action of the enzyme, identifying and managing this reaction could enable higher doses and further improve treatment efficacy.

3.4.3 Potential for Functional Improvement

The functional deficiencies associated with cirrhosis can be attributed to several factors. Vascular changes leading to reduced perfusion are an important component[124, 126-129]. However, there is also evidence to suggest scarring directly influences liver function. Hepatocytes in a stiff environment exhibit suppressed albumin production[12], downregulation of cytochrome p450[13] and HNF4α[14] (two markers of hepatocyte differentiation and liver-specific function), as well as changes in a range of genes associated with normal epithelial function[15]. Hepatocyte senescence is also thought to contribute to liver dysfunction in cirrhosis[16]. The cause of this senescence is typically attributed to repetitive injury[17]; however, there is some evidence in age-associated

senescence research demonstrating a link with tissue stiffness[18, 194], suggesting the local mechanical environment may also play a role in hepatocyte senescence. Therefore, improving the structural and mechanical aspects of cirrhosis may also be able to offer significant functional improvements. In addition, our work discussed in section 2.5.2 proposed a compartment syndrome like effect occurs in the cirrhotic liver. Compartment syndrome exerts a significant mechanical stress from the pressure within the compartment, leading to reduced perfusion[135]. Degradation of the septa can release this pressure, potentially improving circulation.

The two functional metrics investigated in this work were hepatocyte proliferation, indicative of liver regeneration, and nuclear localization of the transcriptional co-activators YAP and TAZ. Hepatocyte proliferation has previously been linked to matrix degrading enzymes, either directly through cell-matrix mechanotransduction or through the release of growth factors bound to the matrix [165, 195-197]. YAP and TAZ are key effectors in the hippo pathway. Prior work has demonstrated that this pathway is a key component of mechanoregulation, and reductions in stiffness result in reduced nuclear localization of YAP/TAZ [198, 199]. However, this master regulatory network has been implicated in a wide variety of liver processes, including fibrosis, response to acute injury and regeneration[200-202]. It is likely that at the 5d timepoint there are a variety of conflicting factors regulating these proteins.

3.4.4 Future Directions

Experimental models with moderate fibrosis (such as the mouse model used here) will naturally remodel and degrade the septa in the weeks after cessation of injury[203]. Longer term studies are needed to determine the functional consequences of the fibrosis reversal we have demonstrated; however, this is complicated by this spontaneous reversal. Rat models may be the more appropriate platform for the next stage of development. The rat

liver develops thicker collagen septa more similar to the human disease, and studies have shown long-term persistence of the septa after cessation of injury[108, 204].

Cirrhosis in humans consists of much thicker and more stable fibrous septa than is present in this mouse model. In addition, research with the bile duct ligation model of fibrosis in rats showed that while spontaneous recovery was possible, it required at least three times longer than it took to establish fibrosis[205]. This, coupled with the rat model findings described above, suggests that highly aggressive collagen degradation will likely be required for successful treatment of cirrhosis in humans. Confirmation of efficacy in the rat model of cirrhosis is an important next step.

The shock hypothesis will also be investigated in future work. Experiments will determine changes in inflammatory markers of systemic shock (such as TNFα and IL-6[190, 206]) and hypoperfusion (such as blood lactate[207, 208]) after varying doses of CCH infusion.

Rheometry for measurements of liver stiffness are not reliable with mouse tissue due to the small size of the tissue and low stiffness. These measurements can however be performed with the rat model[209], which has a much larger liver and higher stiffness due to the greater degree of scarring. Performing this analysis will provide a better understanding of the effect of CCH infusion on the mechanical properties of the tissue.

3.4.5 Summary

We have described the biodistribution of a macromolecule delivered via interstitial infusion in the liver, and used these results to design an infusion protocol that covers the entire liver with minimal off-target exposure. We also used a mouse model of cirrhosis to show that purified CCH can rapidly reduce collagen content in the cirrhotic liver with only mild liver injury of the same level as saline infusion. Future work will investigate the long-term functional consequences of this treatment and investigate the mechanism of toxicity with a view to determining whether higher doses are feasible and beneficial.

Development of a minimally invasive interstitial infusion procedure, potentially under ultrasound guidance, will also be investigated to determine the effect of multiple low-dose infusions over time.

Chapter 4

Mechanical Perturbation via Extracorporeal Shockwave Treatment

4.1 Introduction

Many years ago, it was observed that pulsed-dye lasers could be used to induce vasodilation[210]. While investigating this as a potential treatment for cerebral vasospasm, it was shown that constricted vessels do not re-constrict after treatment[211] and become insensitive to vasoconstricting agents[212]. Kaoutzanis *et al*, 1995[213] concluded that the mechanism is based on laser-generated shockwaves that mechanically disrupt the contracted cytoskeleton of smooth muscle cells in the vessel wall. Importantly, it was also shown that dilated vessels are seemingly unaffected by the laser – there was no significant

change in diameter and they remained sensitive to vasoconstricting agents after treatment[212], indicating that a relaxed cytoskeleton is not disrupted. These results show that the shockwave disruption possesses a selectivity by stiffness. This feature is very appealing in a prospective treatment for cirrhosis, where stiff scar is distributed amongst liver parenchyma. These results suggest that a shockwave could be used to disrupt the fibrous septa while leaving the functional tissue unharmed.

Acoustic energy has been used clinically to cause mechanical perturbations for many years, most notably for lithotripsy where shockwaves are used to break apart kidney stones[214]. Low-energy shockwave treatment has also attracted interest for it's more subtle effects in tissue. This approach uses shockwaves at a much lower energy than in lithotripsy so that there is no mechanical disruption. Low-energy shockwaves have been reported to induce angiogenesis[215], induce stem cell proliferation[216, 217], and suppress inflammation[218]. Low-energy shockwave treatment has even been investigated as a therapy for cirrhosis. Ujiie et al, 2020[219] investigated the use of shockwaves as a treatment for cirrhosis based on the findings that shockwaves can induce VEGF expression[220] and suppress TGFβ[221]. The only timepoint presented in this study was 4 days after shockwave treatment. They reported significant histological improvements, reduced serum AST, and downregulation of TGFβ. The authors proposed that the primary mechanism for these effects was shockwave-induced angiogenesis.

Recently, a shockwave device was successfully developed as a treatment for cellulite[222, 223]. Cellulite is a skin condition consisting of fibrous septa surrounded by adipose tissue which produces a dimpled appearance. The shockwave treatment was shown to selectively break apart the fibrous septa and significantly improve the appearance of the skin. A follow-up pilot study also demonstrated success for inducing the remodeling of hypertrophic skin scars[224].

In this study we aimed to determine whether this device could induce a similar mechanical perturbation in the cirrhotic liver. The experiments were performed in collaboration with AbbVie, the company that developed the RAP shockwave device.

To support higher throughput toxicity testing of the shockwave device than could be achieved with animal models, we looked to the precision-cut liver slice (PCLS) model. There are many well established in vitro models for rapid testing of pharmaceuticals, but these techniques are not applicable to treatments aimed at influencing tissue structure. The PCLS model addresses these issues by using thin slices of liver tissue, which maintains cells in their in vivo matrix. However, there is no consensus on appropriate culture conditions for cirrhotic PCLS. Therefore, we first compared various culture conditions to determine an optimal methodology to be used in the shockwave experiments.

4.1.1 Ex Vivo Models of Cirrhosis for Therapeutic Development

Conventional cell culture systems lack the complexity of tissues, particularly the interactions between cells and the matrix which are a crucial component of cirrhosis. Organ or tissue culture methods preserve complexity while allowing assays similar to those performed in cell cultures. PCLS is an ex vivo tissue culture model that is gaining popularity for the study of liver fibrosis. In this model, thin slices of liver tissue are maintained in standard culture incubators. This preserves the extracellular matrix and resident liver cell populations, providing a more accurate representation of the in vivo interactions between different cell types, and between cells and the matrix. PCLS enable more easily controlled experiments than in vivo models as well as higher throughput as dozens of slices can be obtained from each animal. The primary drawbacks of PCLS are the limited time they can be cultured – typically a few days – as well as changes in expression that occur during culture.

PCLS have particularly attracted interest as a platform to test anti-fibrotic therapies. Many previous experiments have used healthy PCLS treated with pro-fibrotic stimuli, such as TGFβ and PDGF, to induce fibrosis ex vivo[225-233], or have relied on the spontaneous fibrosis activated in PCLS in culture[234-240]. Such experiments are useful to study the earliest onset of liver fibrosis but do not capture many of the effects of chronic liver disease in clinically relevant liver fibrosis. Chronic liver injury induces senescence of a variety of liver cell populations[16, 17], and the long-term deposition of collagen and associated increase in tissue stiffness can suppress hepatocellular function through HNF4a and cytochrome P450[12-14]. There is also a critical positive feedback loop between fibrosis and matrix stiffness[31, 241-243], which could significantly influence the effects of prospective anti-fibrotic therapies.

For a more clinically relevant model, PCLS can be collected from patient biopsies or from animal models after liver fibrosis or cirrhosis is induced in vivo. A variety of fibrosis etiologies have been investigated with this approach, including alcohol[244], hepatitis infection[245], non-alcoholic steatohepatitis (NASH)[244, 246], cholestasis[247-251], and chemical hepatotoxins[244, 252, 253].

The performance of PCLS from cirrhotic animals in culture has not been well characterized. Consequently, prior work with fibrotic and cirrhotic slices often references the methods of experiments performed with slices from healthy animals, which may not be applicable given the significant differences between the healthy and cirrhotic liver. There is also no consensus on appropriate culture conditions, most notably whether to include insulin and dexamethasone in the culture media. A direct comparison of the effect of culture conditions on viability, function, and gene expression has not previously been performed.

To validate the use of this model in our shockwave experiments, we determined the optimal methods for collection and culture of PCLS from cirrhotic rats. We compare the

effect of culture media and rocking on PCLS viability and albumin production, as well as characterize changes in expression of key genes over time and when cultured with and without insulin and dexamethasone. We also compare three methods for the isolation of RNA from cirrhotic PCLS and report a method capable of obtaining RNA with higher yield and purity than the standard RNeasy and TRIzol protocols.

4.1.2 Mechanical Disruption of Tissue with High Frequency Shockwave Treatment

A shockwave is an acoustic wave propagating faster than the speed of sound in the medium. It is characterized by a very short rise time (on the order of nanoseconds) to a high peak compressive pressure, followed by a longer, shallow tensile component.

The Rapid Acoustic Pulse (RAP) device was developed by AbbVie as a treatment for cellulite. It consists of an electrohydraulic shockwave generator with a reflector to produce a planar wave. The reflector uses a freeform design to reduce shadow from the electrode in the path of the shockwave. The device also incorporates rapid cutoff of the electrode voltage after discharge to minimize the tensile component of the wave. This helps prevent cavitation bubbles from forming in the tissue. The RAP device produces a shockwave with very short pulse duration (~1.2μs) and is run at a frequency of 50-100Hz.

The RAP device achieves mechanical disruption through shear. This mechanism relies on the acoustic heterogeneity of the tissue. As the shockwave propagates through the tissue, differences in local tissue properties (e.g., stiffness) cause changes in the shape and speed of the wave front. This creates a gradient in the shock front which results in a shearing effect, as different regions are deforming at a different rate[254-256]. The faster the rise time and the shorter the pulse duration, the finer the resolution of tissue deformation and therefore the greater the shear caused by local heterogeneity. Delivering repeated pulses at a rate such that the tissue does not recover from the previous wave before the next

arrives results in shear accumulation[257]. Rapid pulsing also induces stiffening due to the dependency of stiffness on loading rate in viscoelastic materials. This contributes to disruption because of the greater susceptibility of stiff materials.

This mechanism works well in cellulite because the stiff septa are surrounded by soft adipose tissue[222, 223]. The cirrhotic liver is in a similar state, where stiff fibrous septa encircle the parenchyma. The septa in cirrhosis are substantially tougher than in cellulite, which should make them more difficult to disrupt. However, the RAP device has also been tested in a pilot study with hypertrophic scarring, which revealed significant reductions in scar height and volume 12 weeks after treatment[224]. This suggests shockwave treatment can successfully disrupt thick, highly crosslinked scar.

4.2 Methods

4.2.1 Animals

All animal work was approved by the Massachusetts General Hospital Institutional Animal Care and Use Committee. All experiments were performed in accordance with relevant guidelines and regulations. For the cirrhotic experiments, 2 month old male Wistar rats were purchased from Charles River Laboratories. After a 1 week acclimatization period, cirrhosis was induced with biweekly intraperitoneal injections of thioacetamide at 200mg/kg for 12 weeks followed by a 1 week wash out period. 5 month old male Wistar rats were used for healthy comparisons. Animals were housed in a controlled environment with food and water ad libitum.

4.2.2 PCLS Collection

Animals were euthanized via cardiac puncture under sterile conditions. The whole liver was harvested and 8mm biopsy punches were used to obtain tissue columns. Columns

were collected from the thickest portions of the medial and left lobe. The columns were immediately placed in chilled sterile Krebs Henseleit buffer (KHB; Sigma Aldrich, USA).

Columns were cut in half with a scalpel to obtain 2 shorter columns (**Figure 4-1 A**). These columns were mounted to the platform of a 7000smz-2 vibratome (Campden Instruments Limited, UK) with cyanoacrylate glue and the cutting tray of the vibratome was filled with chilled sterile KHB (**Figure 4-1 B**). The vibratome was fitted with a ceramic blade (Campden Instruments Limited) and run at 50Hz frequency, 2.5mm amplitude, 0.15cm/s advance speed, 250μm slice thickness (**Figure 4-1 C**). The first few slices were discarded to ensure a flat tissue surface. After cutting, slices were transferred to a sterile dish with chilled sterile KHB. A 6mm biopsy punch was used to trim the final PCLS. This step ensures all PCLS are uniform in size, as the initial columns are often irregularly shaped (**Figure 4-1 D**). With such small samples, these irregular edges can result in significant differences in the total amount of tissue. This step also removes any tissue that may have come into contact with glue. The trimmed PCLS were then transferred to a 24 well plate with chilled sterile KHB. The total time from harvesting of the liver to the end of collecting PCLS was around 1 hour. Approximately 20 uniform, viable slices were obtained per animal.

4.2.3 PCLS Culture

PCLS were placed on an 8μm-pore Transwell insert (Corning, USA) in a 12 well plate. All slices were cultured in 1mL Williams' Medium E (Sigma Aldrich) with 2% FBS, 1% pen-strep, and 1% L-glutamine (ThermoFisher, USA). Some slices were additionally cultured with 100nM dexamethasone (Sigma Aldrich) and 1X insulin-transferrin-selenium-

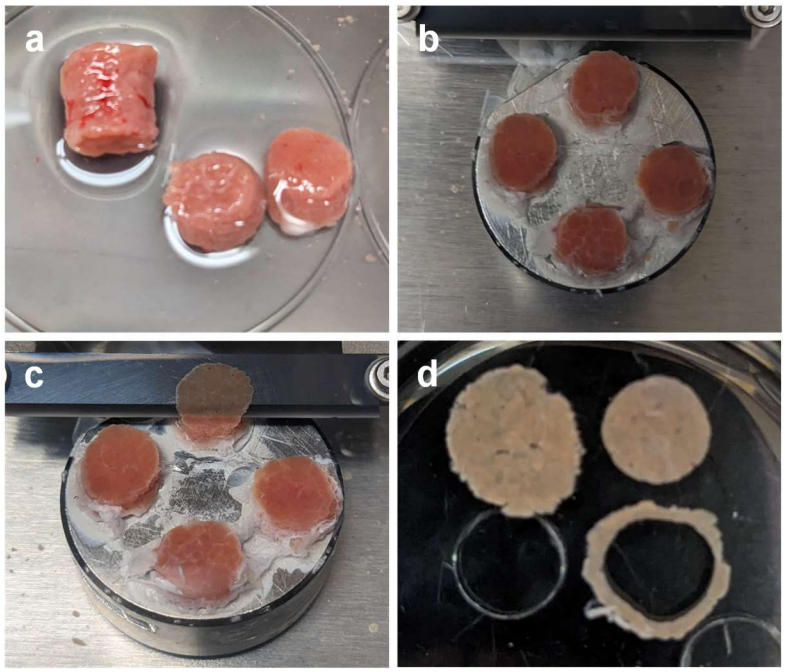

Figure 4-1: PCLS collection. (A) Tissue columns were harvested with an 8mm biopsy punch then cut into 2 shorter columns. (B) Columns were mounted to the vibratome platform with cyanoacrylate glue. (C) 250µm thick PCLS were cut at 50Hz, 2.5mm amplitude, 0.15cm/s. (D) PCLS were trimmed with a 6mm biopsy punch to ensure uniform slices.

ethanolamine (ThermoFisher). Plates were incubated under standard cell culture conditions either stationary or on a rocking platform. Media was changed every 24hrs.

4.2.4 PCLS Viability Assay

PCLS were placed in a 48 well plate with 400µL culture media and 80µL MTS reagent (Abcam, USA). The plates were incubated on a rocking platform under standard cell culture conditions for 1hr then the media was collected and absorbance was measured at 490nm. Measurements were normalized to the viability of fresh slices.

4.2.5 PCLS Albumin ELISA

Media collected from the culture plate was centrifuged at 4°C, 400g for 10min. The supernatant was then stored at -20°C until ready to use. Albumin concentration was measured with a rat albumin ELISA kit (Abcam) according to manufacturer instructions.

4.2.6 PCLS RNA Isolation & qPCR

3 methods of RNA isolation were compared. The first method used the RNeasy micro kit (Qiagen, Germany) according to manufacturer instructions. The second method used TRIzol (Invitrogen, USA) according to the manufacturer instructions. The final method was a protocol reported by Ziros et al. [258] for the isolation of RNA from mouse thyroid, a very small organ which requires high yield RNA extraction. Briefly, PCLS were homogenized in TRIzol and frozen at -80°C for at least 30min. Phase separation was performed with 1-bromo-3-chloropropane (Sigma Aldrich) and the aqueous phase was purified using RNeasy micro spin columns. For all methods, PCLS were homogenized with TissueLyser II (Qiagen).

RNA concentration and purity were measured with NanoDrop (ThermoFisher). RNA integrity was confirmed by gel electrophoresis on E-gel EX 2% agarose gels (Thermofisher).

cDNA was prepared from 1µg total RNA using the SuperScript VILO IV kit (Thermofisher) according to manufacturer instructions. qPCR was then performed with TaqMan Fast Advanced Master Mix (Thermofisher) and TaqMan fluorescent probes for *HNF4A* (Thermofisher; assay ID: Rn04339144_m1), *CYP1A2* (Rn00561082_m1), *LYVE1* (Rn01510421_m1), *TGFB1* (Rn00572010_m1), *COL1A1* (Rn01463848_m1), *ACTA2* (Rn01759928_m1), *CDKN1A* (Rn00589996_m1), and *MKI67* (Rn01451446_m1).

Stability analysis was performed with NormFinder[259] to determine appropriate reference genes. Fresh slices and PCLS after 4 days in culture were compared with TaqMan probes for *B2M* (Rn00560865_m1), *YWHAZ* (Rn00755072_m1), *HPRT1* (Rn01527840_m1), *HMBS* (Rn01421873_g1), *18S* (Hs99999901_s1), *SDHA* (Rn00590475_m1), and *UBC* (Rn01789812_g1). *HPRT1* and *HMBS* were found to be the best combination of reference genes, with a stability value of 0.063.

Student's t-test was performed to assess statistical significance with a p-value threshold of 0.05. The Benjamini-Hochberg procedure was used to correct for multiple comparisons. Yield and purity metrics are expressed as mean ± standard deviation.

4.2.7 PCLS Shockwave Treatment

PCLS were treated 1 day after collection. PCLS were placed in a small petri dish filled with PBS. The dish was placed on top of the shockwave transducer and held in place. Treatment settings tested were two voltage levels (2400V, 3000V), two frequencies (50Hz, 100Hz), and 3 durations (0.5min, 1min, 3min). This set up caused some cavitation during treatment due to proximity of the tissue to the device. The RAP device has a known issue of hot spots at the surface of the transducer. These even out over a short distance, so are

not a concern for in vivo treatment. Samples that were affected by cavitation are marked on the figures.

After treatment, PCLS were placed in fresh media and returned to the incubator. After 6 hours, viability was measured with the MTS assay and culture media was collected for albumin ELISA, as described above.

4.2.8 In vivo Shockwave Treatment

Animals were anesthetized with isoflurane and prepared for surgery by clipping fur on the abdomen and disinfecting with 10% povidone-iodine. The animal was placed on an adjustable platform which was set at an appropriate height to ensure the shockwave transducer was in full contact with the skin (**Figure 4-2**). Ultrasound gel was applied to the skin over the treatment area, followed by an acoustic coupling gel pad, then another layer of ultrasound gel. The shockwave transducer was positioned to be directly over the left lobe of the liver. The RAP device was run at 2400V, 50Hz for two periods of 4 minutes, with a brief break in between to monitor the animal for any signs of adverse effects.

After treatment, the ultrasound gel was removed and the abdomen was disinfected with 10% povidone-iodine. A laparotomy was performed under sterile conditions to confirm cirrhosis and check for any gross signs of liver damage. The muscle and skin were then closed with absorbable sutures. Animals were euthanized at 1 day, 30 days, and 60 days after treatment via cardiac puncture.

4.2.9 Histology

Tissue for histological analysis was collected at the time of euthanasia. Samples were fixed in 4% formaldehyde, embedded in paraffin blocks, and cut into 5μm sections. Slides were stained with picrosirius red (PSR) according to standard protocols. Slides were

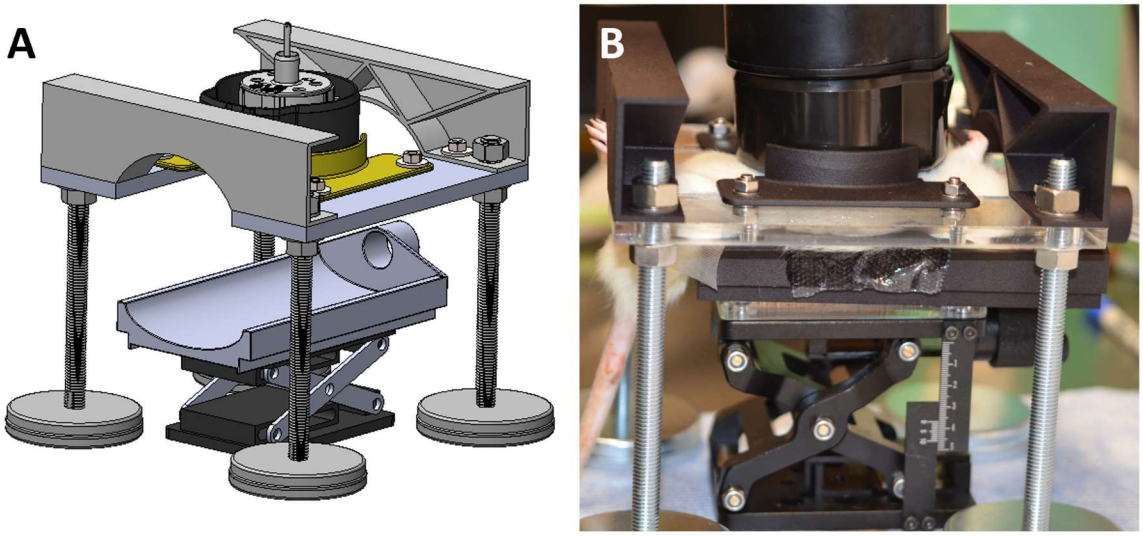

Figure 4-2: RAP Shockwave Experimental Set-up. (A) Model of set-up. The bed for the animal is mounted on an adjustable platform. The heigh is set so that the shockwave transducer rests in full contact with the skin over the treatment site. (B) Set-up in use.

imaged with a Nanozoomer 2.0 HT slide scanner (Hamamatsu, Hamamatsu City, Japan).

4.2.10 Image Quantification

Septum thickness was measured from the PSR stain in the Nanozoomer software. 20 randomly selected septa were selected from each slide, and the thickness was taken at the midpoint[204].

For collagen proportionate area (CPA) assessment, 5x magnification images across the entire section were exported from the PSR whole-slide scans captured with the Nanozoomer. All image names were then masked and randomly ordered with the Blind Analysis tool in ImageJ. CPA was calculated in ImageJ[170, 171].

4.2.11 RNAseq

At the time of euthanasia, two roughly 25mg samples were collected from each animal – one from the left lobe which had been under the shockwave transducer and one from the medial lobe to be used as a paired untreated control – and placed in RNA*later* (Thermo Fisher Scientific). Samples were stored at 4°C overnight and then at -20°C until use. RNA extraction was performed using the RNeasy midi kit with proteinase K digestion and on-column DNase digestion according to the manufacturer's instructions (Qiagen). The samples were then sent to Admera Health for quality control, library preparation, and sequencing. Libraries were prepared using NEBNext Ultra II (New England Biolabs) with poly(A) selection and sequenced on a NovaSeq 6000 (Illumina) with 40M 150bp paired-end reads per sample.

Sequencing data quality was assessed with FastQC[113] and trimmed with Cutadapt[114]. Transcript abundance was quantified with the Salmon quasi-mapping tool[115]. Differential expression analysis was performed using DESeq2 in R[116]. The differential expression model accounted for sample pairing (i.e., treated and untreated control samples taken

from the same animal). Fold change was calculated using the apeglm method for log fold change shrinkage[118]. Over-representation analysis (ORA) for gene ontology gene sets was performed with the clusterProfiler package[117]. Gene sets were enriched if FDR<0.05 with Benjamini-Hochberg correction. ORA figures were generated with the enrichplot package[119].

4.3 Results

Subsections 4.3.1 through 4.3.4 cover the cirrhotic PCLS model development and comparison of culture techniques. Subsections 4.3.5 through 4.3.8 cover the results of the shockwave treatment study.

4.3.1 Effect of Culture Conditions on Cirrhotic PCLS Viability and Function

Two parameters were evaluated for their effect on cirrhotic PCLS viability and function: media supplements (insulin-transferrin-selenium-ethanolamine and dexamethasone) and incubation on a rocking platform. PCLS cultured with these supplements had no significant difference in overall viability after 4 days in culture (**Figure 4-3 A**) but the supplemented media significantly increased PCLS function at all timepoints (**Figure 4-3 B**). Similarly, incubation on a rocking platform did not have an effect on the overall viability (**Figure 4-3 C**) but preserved PCLS function at later timepoints (**Figure 4-3 D**).

Interestingly, we also found that cirrhotic PCLS maintained higher viability in culture than PCLS from healthy animals until day 4 (**Figure 4-3 E**). This may be related to the poor perfusion and hypoxic environment of the cirrhotic liver in vivo [124-127]. Survival in culture is heavily dependent on oxygen delivery to the tissue, so it is possible that adaptation to hypoxia in vivo enables better survival ex vivo.

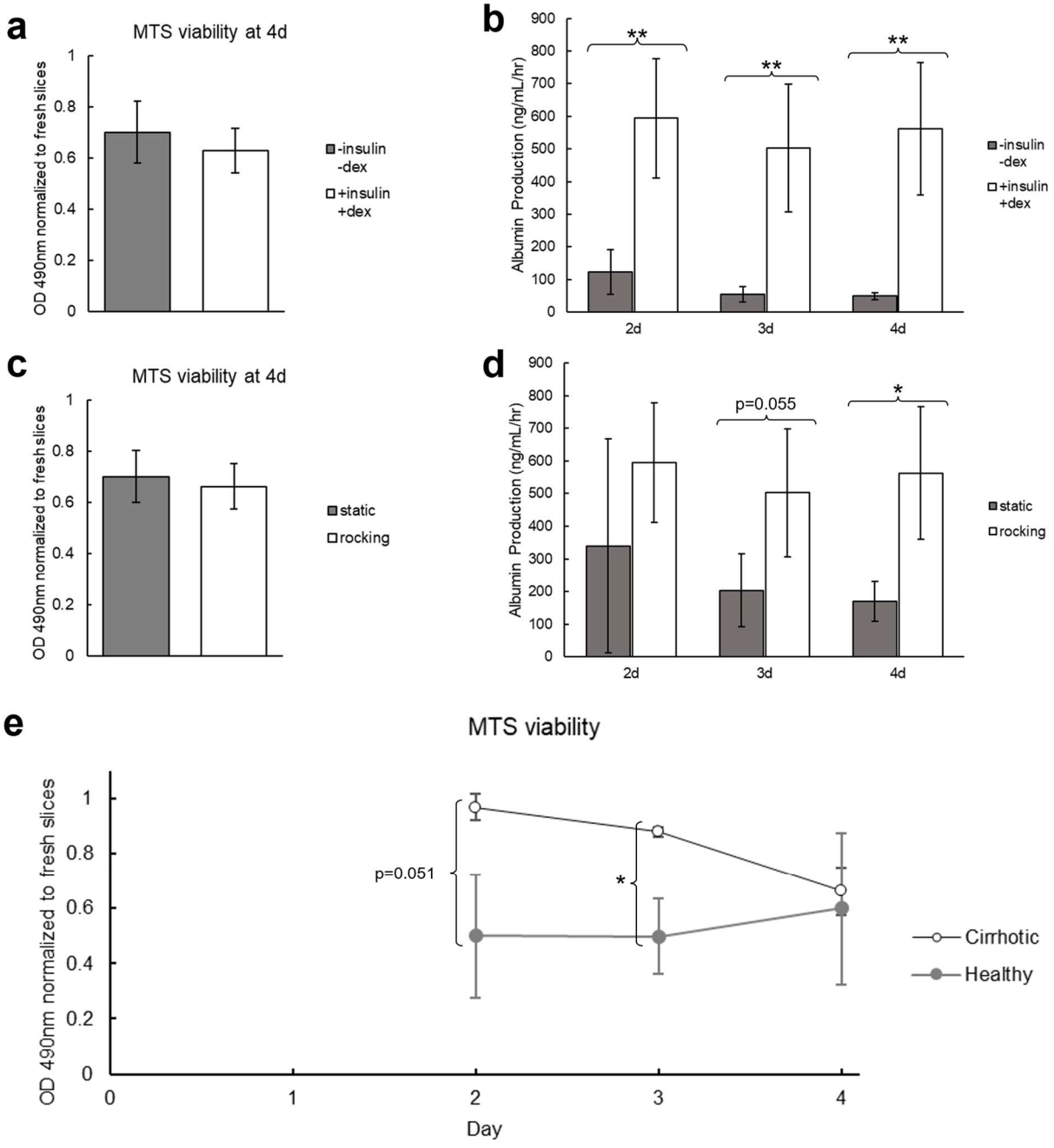
a
MTS viability at 4d
OD 490nm normalized to fresh slices
-insulin -dex
+insulin +dex
b
Albumin Production (ng/mL/hr)
**
**
**
2d
3d
4d
-insulin -dex
+insulin +dex
c
MTS viability at 4d
OD 490nm normalized to fresh slices
static
rocking
d
Albumin Production (ng/mL/hr)
p=0.055
*
2d
3d
4d
static
rocking
e
MTS viability
OD 490nm normalized to fresh slices
p=0.051
*
Day
Cirrhotic
Healthy

Figure 4-3: Comparison of culture conditions for cirrhotic PCLS viability and function. (A&B) Cirrhotic PCLS viability and function when cultured with and without insulin-transferrin-selenium-ethanolamine and dexamethasone. Both groups were incubated on a rocking platform. (A) Viability measured by MTS assay after 4 days in culture normalized to the viability of fresh PCLS. There is no significant difference in slice viability. (B) ELISA for albumin secreted into the media over 4 days in culture. Culturing with insulin-transferrin-selenium-ethanolamine and dexamethasone significantly increases PCLS function at all timepoints. (C&D) Cirrhotic PCLS viability and function when incubated on a rocking platform or static. Both groups were cultured with insulin-transferrin-selenium-ethanolamine and dexamethasone. (C) Viability measured by MTS assay after 4 days in culture. There is no significant difference in slice viability. (D) ELISA for albumin secreted into the media over 4 days in culture. Culturing on a rocking platform significantly increased PCLS function at the 4 day timepoint. (E) Viability of healthy and cirrhotic PCLS measured by MTS assay over 4 days in culture normalized to viability of fresh healthy and cirrhotic PCLS, respectively. The cirrhotic slices maintain higher viability until day 4. (n=3 per timepoint; p-value calculated with t-test; *$p<0.05$, **$p<0.01$)

4.3.2 Comparison of RNA isolation methods for cirrhotic PCLS

RNA yield and purity for three isolation methods – Qiagen RNeasy kit, standard TRIzol protocol, and the small tissue RNA isolation protocol described by Ziros et al. for the isolation of high-quality RNA from mouse thyroid – were compared with cirrhotic PCLS after 4 days in culture (**Table 4-1**). The RNeasy protocol produced high purity RNA, but with very low yield. Conversely, the TRIzol protocol gave higher yield but with poor purity. The protocol described by Ziros et al. gave the highest yield and purity of all 3 protocols. To determine whether the difference in purity would significantly alter expression measurements, RNA isolated by the TRIzol and Ziros et al. protocols were compared with qPCR. Of the 8 genes measured, 1 was found to have a statistically significant difference in expression after multiple hypothesis correction (**Appendix**

Figure C-1). We also found that there is a significant decrease in RNA yield from PCLS in culture compared to fresh slices in addition to a small but statistically significant decrease in $A^{260}/_{280}$ (**Table C-1**).

4.3.3 Effect of Culture Media on Expression in Cirrhotic PCLS

Expression of 8 key genes related to liver function and fibrosis were evaluated by qPCR for cirrhotic slices cultured for 4 days with and without insulin-transferrin-selenium-ethanolamine and dexamethasone (**Figure 4-4**). In all cases with statistically significant differences, culturing with these supplements resulted in expression more similar to fresh slices. *HNF4A* and *CYP1A2*, markers of hepatocyte function and differentiation, were increased with the supplemented media. *TGFB1*, a key gene associated with the spontaneous ex vivo fibrosis response, was reduced with the supplemented media, as well as *MKI67*, a marker of proliferation. There were no statistically significant differences in expression of *LYVE1*, a marker of liver sinusoidal endothelium, *COL1A1* and *ACTA2*, markers of fibrosis, or *CDKN1A* (p21), a marker of senescence.

4.3.4 Time Course of Expression Changes in Cirrhotic PCLS

Expression of these 8 genes were measured at the 2 day and 4 day timepoints to characterize how expression changes over time in culture (**Figure 4-5**). For these results, all slices were cultured with insulin-transferrin-selenium-ethanolamine and dexamethasone, and were incubated on a rocking platform. We found that despite stable viability and function, there are already significant differences in many genes by the 2 day timepoint. *HNF4A* and *CYP1A2* are significantly downregulated compared to fresh slices by day 2, and expression further decreases by day 4. *LYVE1* expression is only significantly decreased at the 4 day timepoint. Significantly elevated expression of *TGFB1*, *COL1A1*, and *ACTA2* is not observed until the 4 day timepoint, indicating that the ex vivo spontaneous pro-fibrotic stimuli induce a relatively slow process in cirrhotic

RNA Isolation Protocol	Yield (μg/mg tissue)	$A^{260}/_{280}$	$A^{260}/_{230}$
Qiagen RNeasy	0.2±0.1	2.01±0.03	1.7±0.4
TRIzol	1.5±0.1	1.89±0.03	0.6±0.1
Ziros *et al.*	2.3±0.9*	2.03±0.03†	1.9±0.4†

Table 4-1: Yield and purity metrics for three methods of RNA isolation from cirrhotic PCLS after 4 days in culture. The protocol described by Ziros et al. gives the highest yield and RNA purity. (n=13 Qiagen RNeasy, n=6 TRIzol, n=27 Ziros et al.; p-value calculated with t-test; *$p<0.05$ comparing Ziros et al. and Qiagen RNeasy protocols, †$p<0.05$ comparing Ziros et al. and Trizol)

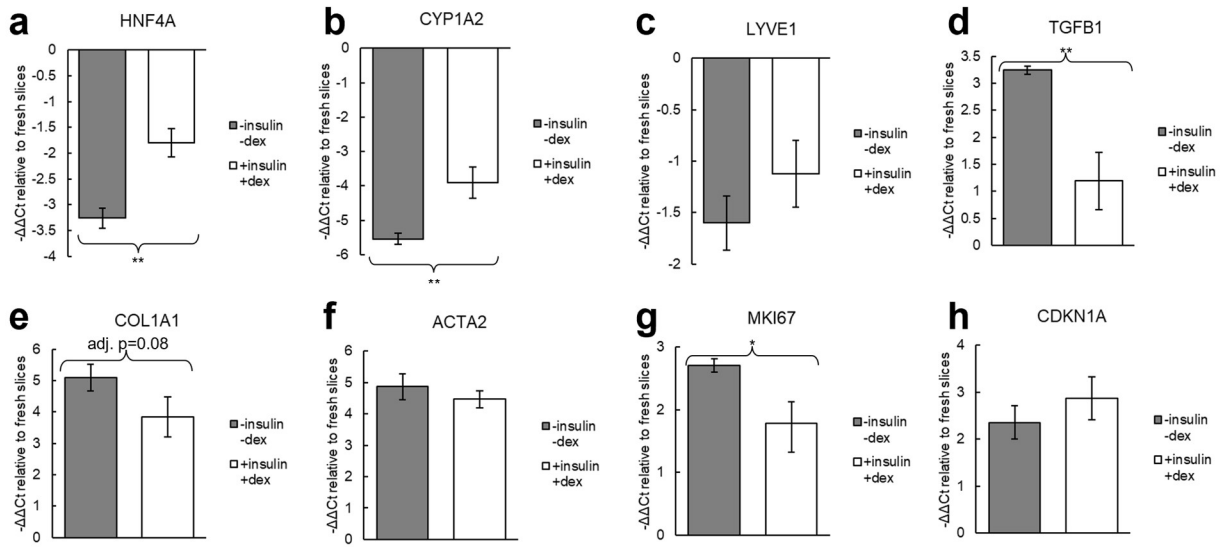

Figure 4-4: Expression changes in cirrhotic PCLS after 4 days in culture with and without insulin-transferrin-selenium-ethanolamine and dexamethasone. Both groups were incubated on a rocking platform. ΔΔCt values were calculated relative to fresh slices. For all genes with statistically significant differences, culturing with insulin-transferrin-selenium-ethanolamine and dexamethasone maintained expression closer to fresh slices. Statistical tests were performed on the ΔCt values. (n=3; p-value calculated with t-test and corrected with the Benjamini-Hochberg procedure; *p<0.05, **p<0.01)

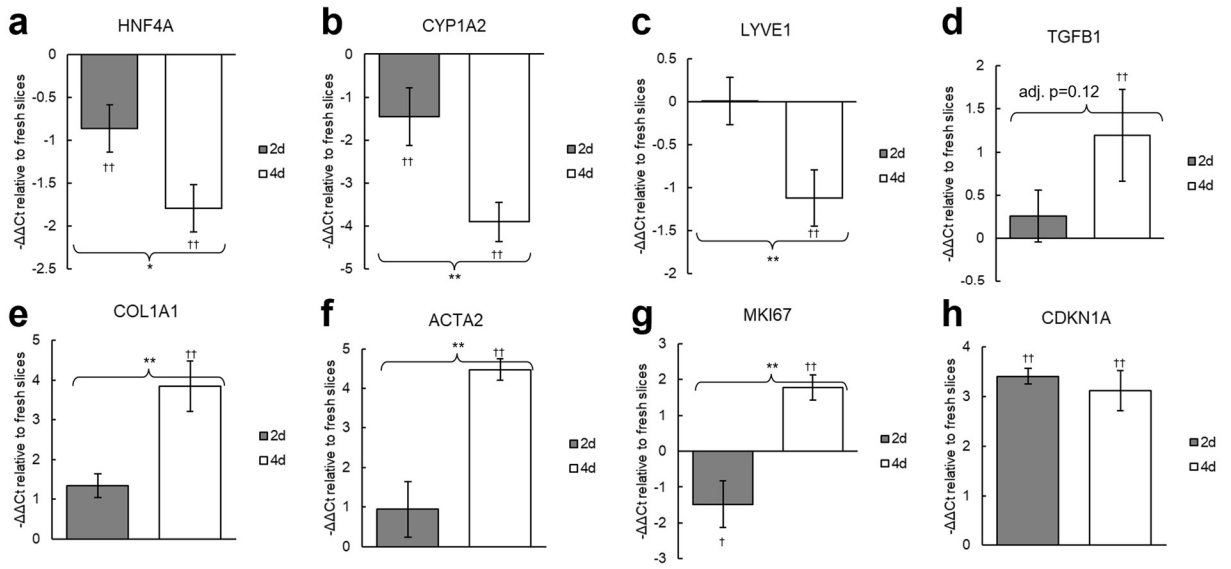

Figure 4-5: Expression changes in cirrhotic PCLS at 2 days and 4 days in culture. Slices were cultured with insulin-transferrin-selenium-ethanolamine and dexamethasone, and were incubated on a rocking platform. ΔΔCt values were calculated relative to fresh slices. Statistical tests were performed on the ΔCt values. (n=3; p-value calculated with t-test and corrected with the Benjamini-Hochberg procedure; *p<0.05, **p<0.01; †p<0.05 compared to fresh slices, ††p<0.01 compared to fresh slices.)

PCLS. *CDKN1A* expression is significantly elevated by day 2 and there is no significant difference in expression between the 2 day and 4 day timepoints. Interestingly, *MKI67* expression is decreased at the 2 day timepoint but increased by day 4.

4.3.5 PCLS Shockwave Treatment

The work described in sections 4.3.1 to 4.3.4 was performed to develop a cirrhotic PCLS culture methodology that would support the future development of therapies for cirrhosis. A model that maintains the resident liver cell populations in their in vivo matrix is particularly important for the direct structural perturbation approach under investigation in this thesis. Using this methodology, we next performed an ex vivo toxicity analysis for the shockwave treatment using cirrhotic PCLS.

PCLS were treated at 2 voltage levels (2400V and 3000V, increasing voltage increases peak pressure), 2 frequencies (50Hz and 100Hz), and 3 durations (0.5min, 1min, and 3min). PCLS viability 6hrs after treatment was compared to untreated control slices.

The results of this parameter sweep showed the shockwave treatment is well tolerated (**Figure 4-6**). During PCLS treatment some slices experienced cavitation tearing (marked in red on). This is an artifact caused by proximity to the shockwave transducer and would not be expected to be an issue during in vivo experiments. These slices tended to have lower viability than slices that were not affected by the cavitation. Despite this, there was no significant difference between viability of control slices and treatment slices at any of the tested intensities.

Since the treatment had minimal toxicity at all tested intensities, we elected to run the RAP device at 2400V, 50Hz for two sets of 4min during the in vivo tests. This decision was also based on treatment parameters used in prior experiments with the device for cellulite[223], hypertrophic scars[224], and unpublished data collected by AbbVie.

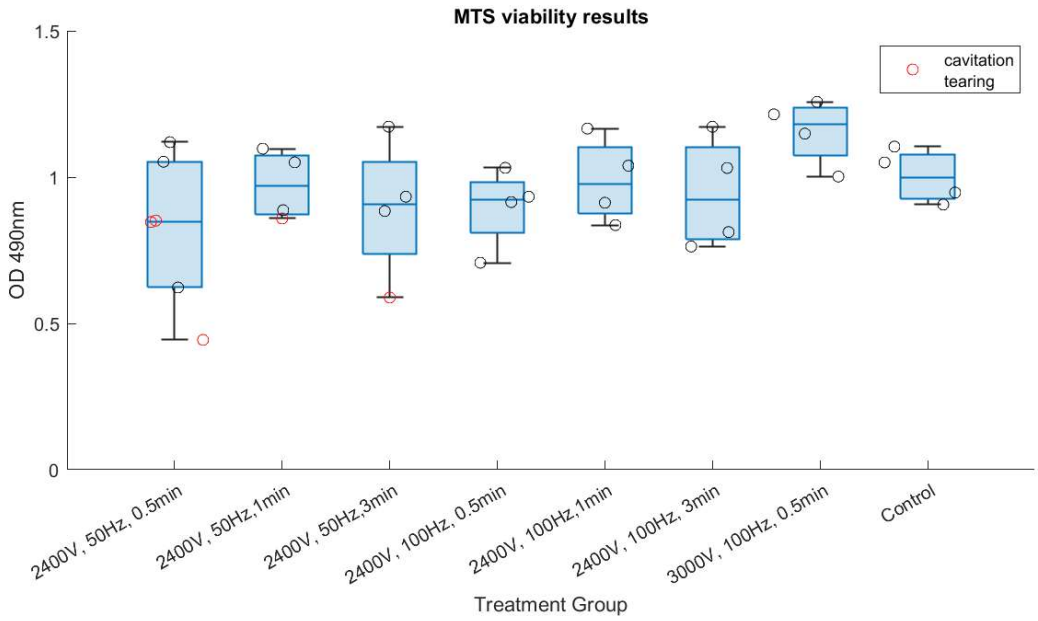

Figure 4-6: Viability of cirrhotic PCLS 6hr after shockwave treatment across a range of treatment intensities. Voltage correlates to the peak pressure of the shockwave. Samples marked in red experienced cavitation tearing due to the experimental set-up. As would be expected, these samples tended to have lower viability. Despite this, no treatment had a significant difference in viability compared to control PCLS. (p-value calculated with t-test)

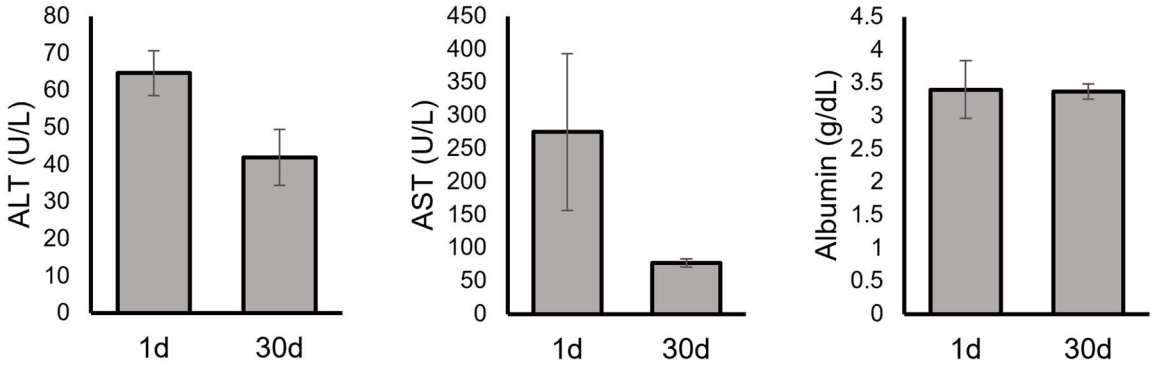

Figure 4-7: Serum markers of liver injury and function after in vivo shockwave treatment. Mild elevations in ALT and AST were observed 1d after treatment. As expected, ALT and AST are within normal range at the 30d timepoint. Shockwave treatment had no effect on serum albumin levels. (n=3 at 1d, n=4 at 30d)

4.3.6 In vivo Shockwave Toxicity

In vivo toxicity was assessed by serum liver enzymes (**Figure 4-7**). Mild elevations in ALT and AST were observed 1d after shockwave treatment, suggesting minor liver injury. The normal reference range for male Wistar rats is 24-49 U/L ALT and 50-96 U/L AST[260]. Some component of this can also be attributed to the anesthesia and laparotomy. Regardless, these small elevations in AST and ALT are not a major concern (for reference, AST/ALT elevations in humas are considered mild if <5 fold upper limit of normal, moderate 5-10, marked >10[261]). As would be expected so far after the procedure, AST and ALT were within normal range at 30d.

Serum albumin was measured as a marker of liver synthetic function. There was no change in albumin production after treatment.

4.3.7 In vivo Shockwave Efficacy

Efficacy of shockwave treatment was assessed by histology 30d and 60d after treatment. On analysis, we observed a difference in the response to treatment based on septum thickness. **Figure 4-8** shows the percent change in septum thickness $\left(\%\Delta t = {t_{untreated} - t_{treated}}/{t_{untreated}}\right)$ plotted against the septum thickness in the untreated lobe. There appears to be a significant distinction in the response to treatment above and below a septum thickness around 60μm. All animals below this threshold showed a marked reduction in septum thickness in the treated lobe compared to the paired untreated control, while all animals above had no difference. This may reflect a mechanical limitation of the shockwave treatment. Thick septa would be expected to be much tougher and therefore more resistant to disruption than thinner septa. This data suggests around 60μm the shockwave may be unable to affect the septa, at least at the intensity

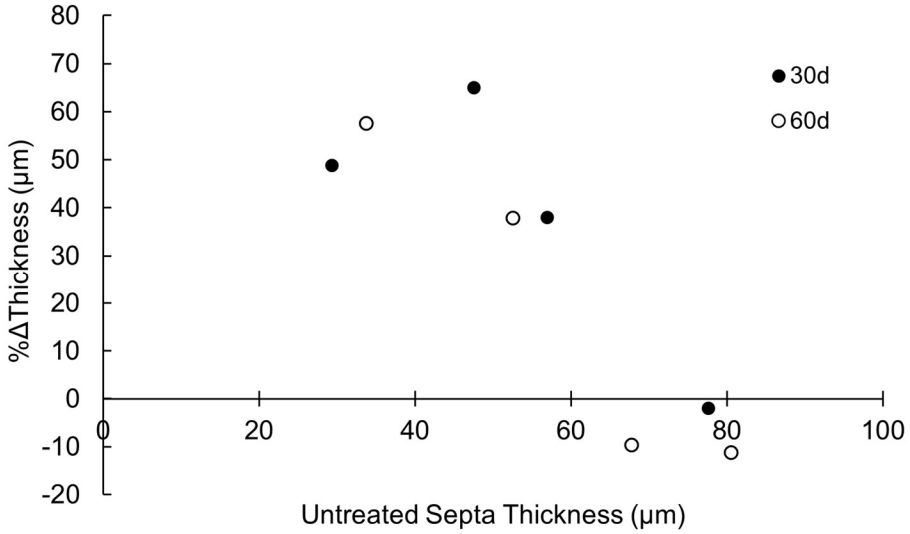

Figure 4-8: Percent difference in septa thickness between the treated and untreated lobe vs septa thickness in the untreated lobe. This was calculated using the formula: $\%\Delta t = {}^{t_{untreated} - t_{treated}}/_{t_{untreated}}$. There is a marked difference in the response to treatment for samples with septa less than 60µm thick and those with septa greater than 60µm. This may indicate a mechanical limitation of shockwave treatment, where thick septa are resistant to disruption.

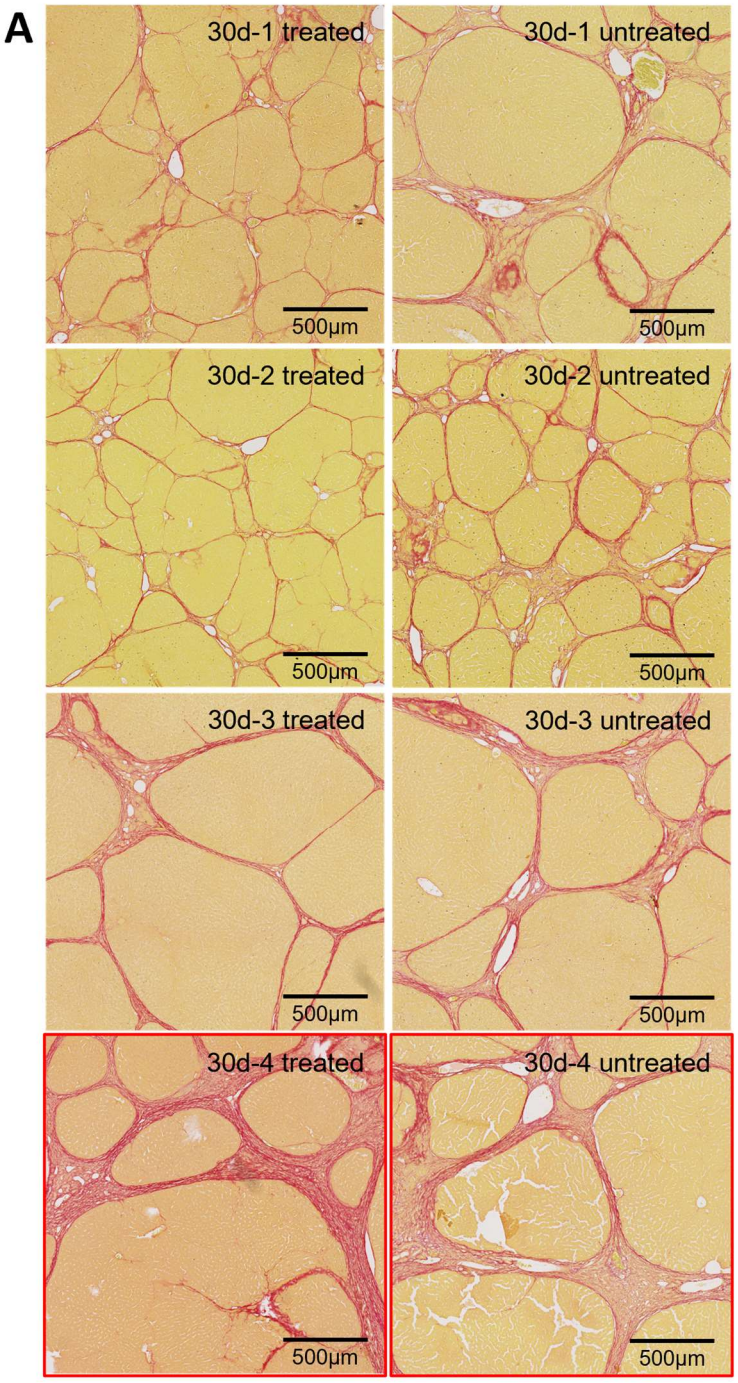

B Mean Septa Thickness (µm)

	Treated Lobe	Untreated Lobe
30d-1	17±8	48±33
30d-2	15±7	29±17
30d-3	35±21	57±35
30d-4	79±42	78±38

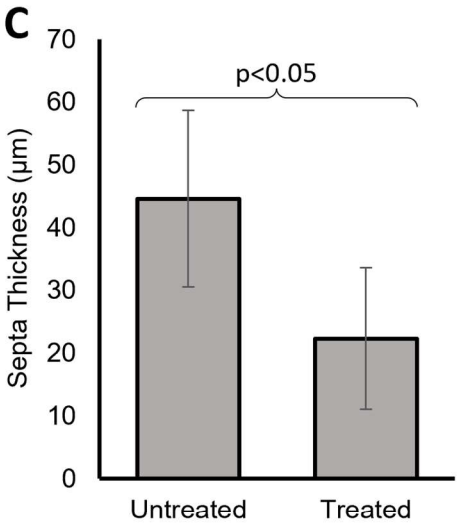

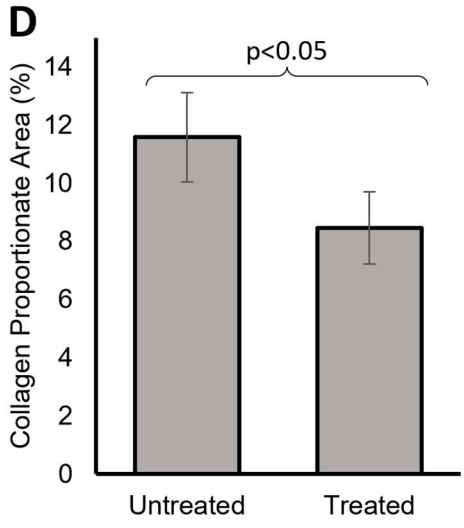

Figure 4-9: Histological results 30d after shockwave treatment. (A) Picrosirius red staining for the treated and untreated lobe. (B) Quantification of septa thickness. (C, D) Septa thickness and collagen proportionate area, respectively, in the treated and untreated lobes. The specimen highlighted in red was excluded from these graphs due to the hypothesized effect of septa thickness on the response to treatment. There was a statistically significant reduction in both these metrics in the treated lobe compared to the paired untreated control lobe. (p-value calculated with t-test)

used in this experiment. This interpretation is not strongly supported given the limited number of animals, but the difference in response of these two groups is striking.

Figure 4-9 summarizes the results for the 30d timepoint. 3 out of the 4 animals at this timepoint showed reduced septa thickness in the treated lobe. The 4th animal had a mean septa thickness of 78μm in the untreated lobe and 79μm in the treated lobe. Excluding this animal, there was a statistically significant reduction in septum thickness and collagen proportionate area in the treated lobe compared to the paired untreated controls.

The results for the 60d timepoint are consistent with the findings at 30d, though 2 out of the 4 animals were above the 60μm septa thickness threshold (**Figure 4-10**).

4.3.8 Shockwave RNAseq Analysis

RNAseq analysis was performed with samples from the 30d timepoint, excluding animal 30d-4 due to the septa thickness discussed above. The analysis returned a short list of only 42 differentially expressed genes (DEGs) with adjusted p-value < 0.05. However, there was a clear trend in the genes identified. 30 of the 42 DEGs (71%) are associated with matrix remodeling. A heatmap of these genes showing the $\log_2$(fold change) between the treated lobe and paired untreated control lobe is shown in **Figure 4-11 A**. Over-representation analysis similarly returned many gene sets related to matrix remodeling, including 'extracellular matrix organization', 'collagen fibril organization',

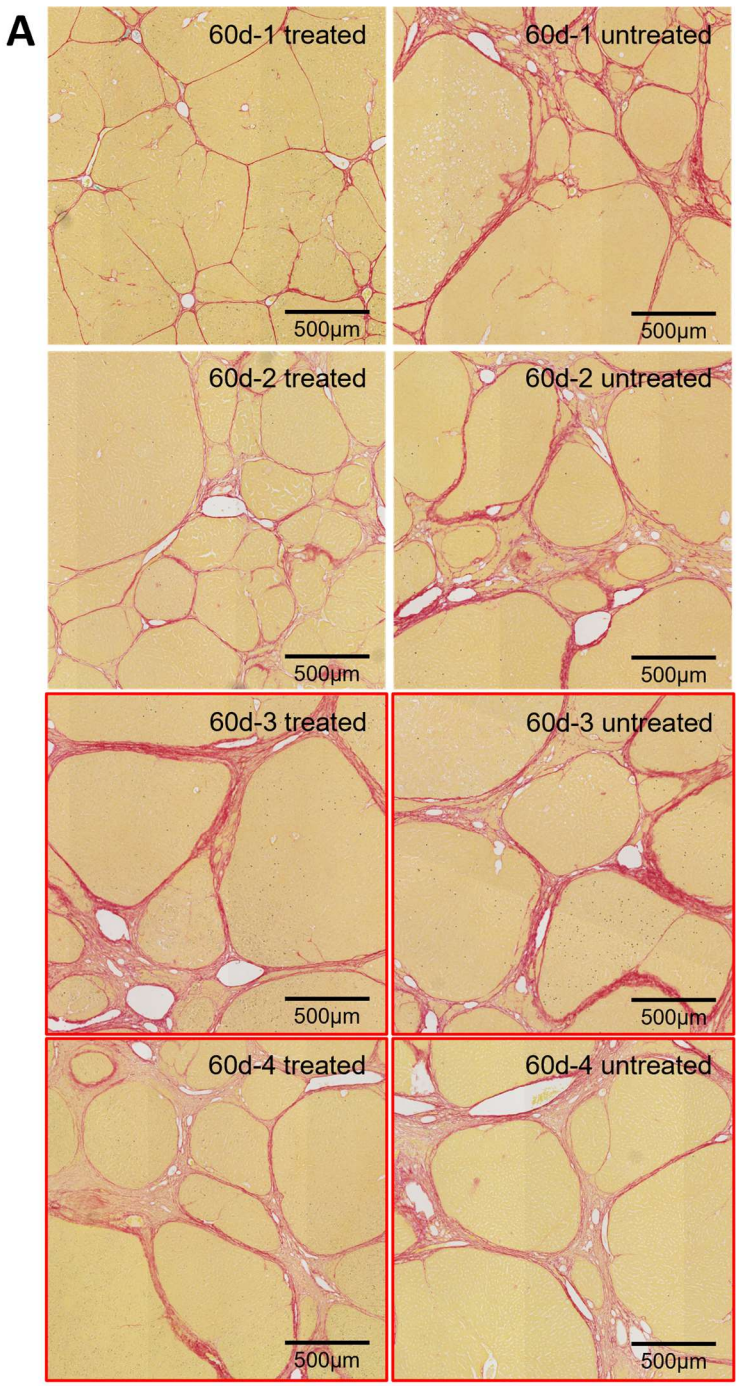

B Mean Septa Thickness (µm)

	Treated Lobe	Untreated Lobe
60d-1	14±8	34±19
60d-2	33±15	53±38
60d-3	74±43	68±58
60d-4	90±51	81±46

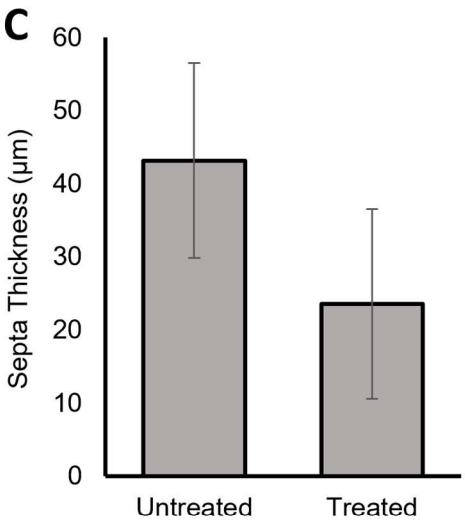

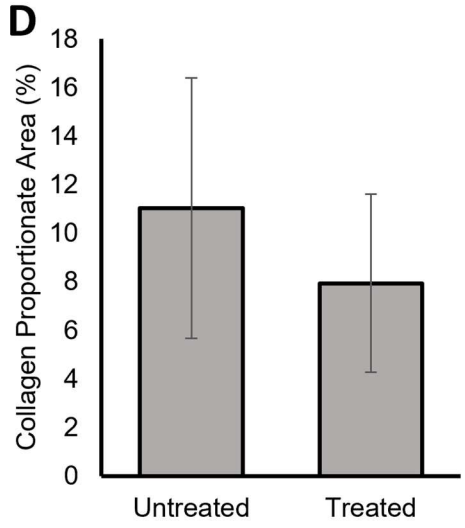

Figure 4-10: Histological results 60d after shockwave treatment. (A) Picrosirius red staining for the treated and untreated lobe. (B) Quantification of septa thickness. (C, D) Septa thickness and collagen proportionate area, respectively, in the treated and untreated lobes. The specimens highlighted in red were excluded from these graphs due to the hypothesized effect of septa thickness on the response to treatment. (p-value calculated with t-test)

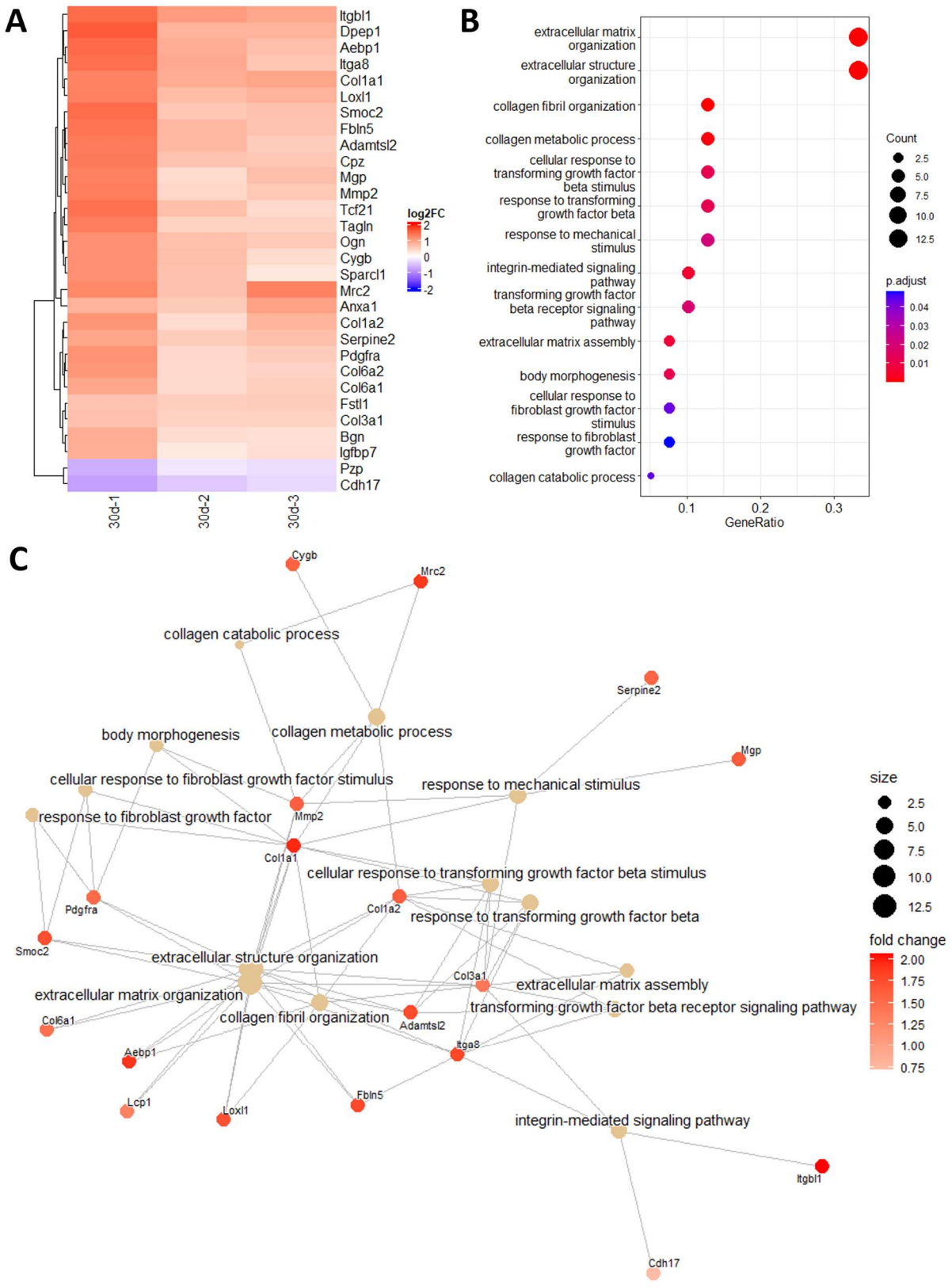
A
Itgbl1
Dpep1
Aebp1
Itga8
Col1a1
Loxl1
Smoc2
Fbln5
Adamtsl2
Cpz
Mgp
Mmp2
Tcf21
Tagln
Ogn
Cygb
Sparcl1
Mrc2
Anxa1
Col1a2
Serpine2
Pdgfra
Col6a2
Col6a1
Fstl1
Col3a1
Bgn
Igfbp7
Pzp
Cdh17
log2FC
2
1
0
-1
-2
30d-1
30d-2
30d-3
B
extracellular matrix organization
extracellular structure organization
collagen fibril organization
collagen metabolic process
cellular response to transforming growth factor beta stimulus
response to transforming growth factor beta
response to mechanical stimulus
integrin-mediated signaling pathway
transforming growth factor beta receptor signaling pathway
extracellular matrix assembly
body morphogenesis
cellular response to fibroblast growth factor stimulus
response to fibroblast growth factor
collagen catabolic process
0.1
0.2
0.3
GeneRatio
Count
2.5
5.0
7.5
10.0
12.5
p.adjust
0.04
0.03
0.02
0.01
C
Cygb
Mrc2
collagen catabolic process
Serpine2
body morphogenesis
collagen metabolic process
Mgp
cellular response to fibroblast growth factor stimulus
response to mechanical stimulus
response to fibroblast growth factor
Mmp2
Col1a1
cellular response to transforming growth factor beta stimulus
Pdgfra
Col1a2
response to transforming growth factor beta
Smoc2
extracellular structure organization
Col3a1
extracellular matrix assembly
extracellular matrix organization
transforming growth factor beta receptor signaling pathway
Col6a1
collagen fibril organization
Adamtsl2
Aebp1
Itga8
Lcp1
Loxl1
Fbln5
integrin-mediated signaling pathway
Itgbl1
Cdh17
size
2.5
5.0
7.5
10.0
12.5
fold change
2.00
1.75
1.50
1.25
1.00
0.75

Figure 4-11: RNAseq analysis 30d after shockwave treatment. (A) Heatmap of differentially expressed genes (DEGs) associated with matrix remodeling. (B) Dotplot of selected enriched gene sets related to matrix remodeling. (C) Concept network plot showing the DEGs contributing to enrichment of matrix remodeling gene sets and the interconnectedness of these sets. (n=3)

'collagen metabolic process', 'response to transforming growth factor beta', 'integrin-mediated signaling pathway', and 'extracellular matrix assembly' (**Figure 4-11 B**). These gene sets are highly interconnected (**Figure 4-11 C**) and overall point to an ongoing broad matrix remodeling process.

The only liver function related gene in the list of DEGs was *Alb* (albumin), which had a 1.25-fold downregulation in the treated lobe. This result is difficult to interpret, as we would expect albumin expression to increase with the observed reduction in fibrosis[262, 263]. However, the serum albumin concentration was unaffected (**Figure 4-7**).

4.4 Discussion

4.4.1 Performance of Cirrhotic PCLS in Culture

In this work we characterized the performance of cirrhotic PCLS in culture and clarified the effect of different commonly used culture conditions. We describe a method for the collection and culture of cirrhotic PCLS that are viable with stable function for up to 4 days. Our results show that there is a clear benefit to culturing with insulin and dexamethasone as well as incubating on a rocking platform. This method significantly improved albumin production and maintained expression of *HNF4A*, *CYP1A2*, *TGFB1*, and *MKI67* closer to the level in fresh slices. We would recommend using these methods unless they are contraindicated by the specific hypothesis under investigation (e.g., insulin interfering with a signaling pathway of interest).

Viability and albumin production are the most commonly used methods in prior work to characterize the performance of PCLS in culture. However, we also investigated changes in expression of key liver genes and found several important changes that are not reflected by these assays. Despite high albumin production throughout the time in culture, there was progressive decline in expression of *HNF4A* and *CYP1A2*, two key regulators of hepatocellular function. This is possibly due to the same process of dedifferentiation that is commonly observed with primary hepatocytes in culture[264-268]. We also found that the senescence marker *CDKN1A* is upregulated at both day 2 and 4. Hepatocyte senescence is associated with a pro-inflammatory secretory state, declining function, and suppressed proliferation[17, 269]. Interestingly, we observed that the proliferation marker *MKI67* is downregulated at the 2 day timepoint, but becomes upregulated by day 4. This biphasic response may indicate differing proliferative states for different cell populations. It is possible that hepatocyte senescence drives *MKI67* expression down at day 2, while a delayed fibrotic response – demonstrated by upregulation of *TGFB1*, *COL1A1*, and *ACTA2* – activates proliferation of stellate cells at the 4 day timepoint. We also found that *LYVE1* is downregulated at day 4. *LYVE1* is a marker of liver sinusoidal endothelial cells, and its downregulation is associated with capillarization of sinusoids[270, 271]. This may indicate some damage or dedifferentiation is occurring to the sinusoidal endothelium in culture.

These results demonstrate that different metrics provide different results for the stability of PCLS in culture. Viability and albumin production remain high up to 4 days in culture. However, when compared to fresh slices there are significant changes in expression of key genes as early as day 2. It is difficult to reconcile these data to produce a single number for the time cirrhotic PCLS can be cultured. An appropriate timeline needs to be determined on a case-by-case basis depending on the specific hypothesis and metrics under investigation.

4.4.2 RNA Isolation from PCLS

We have also reported a protocol for RNA isolation with higher yield and purity than the standard RNeasy and TRIzol protocols. High yield is necessary to extract sufficient RNA for quality control and downstream assays from small tissue samples, while high purity is required to prevent contaminants from interfering in expression measurements. The general guideline for pure RNA is $A^{260}/_{280}$ around 2.0 and $A^{260}/_{230}$ between 1.8-2.2[272]. With the protocol described by Ziros et al., we were able to obtain RNA with $A^{260}/_{280}$ of 2.03±0.03 and $A^{260}/_{230}$ of 1.9±0.4 (Table 1). It should be noted that these ratios depend on the concentration of both RNA and contaminants – so trace amounts of a contaminant could significantly skew the purity ratio if the RNA concentration is also low. Typical contaminants that absorb at 230nm are phenol and guanidine thiocyanate found in lysis buffers. In high quantities these contaminants can inhibit PCR and give misleading expression results.

4.4.3 PCLS from Cirrhotic vs Healthy Animals

We also showed that cirrhotic slices remain viable in culture longer than slices from healthy animals. This may be due to adaptation in vivo to the hypoxic and poorly perfused cirrhotic liver[124-127]. This enhanced survival ex vivo adds to the benefits of PCLS from cirrhotic or fibrotic animals as a more appropriate model to test anti-fibrotic therapies than PCLS from healthy animals. Though some previous studies have used healthy PCLS to test antifibrotic therapies, this approach likely has limited application to clinically relevant liver fibrosis. The collagen deposition and increasing tissue stiffness in chronic liver fibrosis have a variety of effects on the liver. There is a crucial positive feedback loop between matrix stiffness and collagen deposition – increasing stiffness causes pro-fibrotic signaling, leading to collagen deposition and further increasing stiffness[31, 241-243] – which would not be established in PCLS from healthy animals. For this

reason, treatments that can suppress fibrosis in soft tissues may be less effective in stiff tissues. Matrix stiffness also influences hepatocyte phenotype, with a stiffer matrix leading to loss of hepatocyte-specific functions [12-14]. This would be important for functional outcome metrics and toxicology. These aspects are unlikely to sufficiently develop in healthy slices over just a few days in culture but can be captured with fibrosis induced in vivo.

4.4.4 PCLS Summary

PCLS are a promising platform for the future of antifibrotic therapy development. The interactions between different cell populations as well as interactions with their microenvironment is a crucial part of the response to disease, injury, and treatment. Especially in the setting of fibrosis, cell-matrix biomechanics plays an important regulatory role. Other methods that attempt to address this include organoids and 3D co-culture platforms that mimic parts of the in vivo liver[273-275]. PCLS is a relatively simple technique that directly captures all liver cell populations in their native architecture. PCLS also has the benefit of being able to be used with human liver biopsies – enabling new compounds to be tested on human tissue and potentially opening the possibility of personalized medicine applications.

Cirrhotic PCLS also offer several advantages over in vivo models. Cirrhosis takes several months to develop in mice and rats. With the PCLS model, each cirrhotic animal can provide dozens of PCLS which can be divided between many different experimental groups. This enables higher throughput testing of new therapies, while also reducing the number of required animals. Where appropriate, PCLS also provide the opportunity for highly controlled experiments as nearly identical serial slices can be tested under multiple conditions. Ultimately PCLS are not a replacement for in vivo testing – given the lack of circulating immune cells and inability to identify potential toxicity outside the liver,

among other drawbacks – but they enable faster and easier screening of compounds in a realistic and meaningful ex vivo platform which can substantially reduce the number of animals required for therapeutic development. This model is particularly useful for rapid testing of treatments that aim to exert a direct effect on tissue structure.

4.4.5 Clinical Implications of Histological Findings after Shockwave Treatment

The most commonly used staging systems for clinical liver fibrosis, such as METAVIR and Ishak, group all cirrhosis patients into a single category (e.g., in the METAVIR system, F0 = no fibrosis, F1 = portal fibrosis without septa, F2 = portal fibrosis with rare septa, F3 = numerous septa without cirrhosis, F4 = cirrhosis[276]). However, this does not accurately reflect the clinical reality of cirrhosis, which can vary greatly in severity and prognosis. To address this, the Laennec system for subclassifying cirrhosis was introduced[277]. This is a qualitative grading system that stratifies cirrhosis into 3 subcategories based primarily on septa thickness: 4A = thin septa, 4B = broad septa, 4C = very broad septa or at least half of the biopsy is composed of micronodules. Several studies have reported differences in clinical metrics and outcomes across these subcategories. Krawczyk et al, 2017 and Kim et al 2012 reported liver stiffness measured by transient elastography increases with Laennec stage[278, 279]. Kim et al, 2012 also found greater risk of liver-related events (defined as hepatic decompensation, hepatocellular carcinoma, and liver-related death) as Laennec stage increased[279]. Kim et al, 2011 found hepatic venous pressure gradient (a quantitative measure of portal hypertension severity) significantly increased with Laennec stage: 8.1±2.6mmHg in 4A, 12.4±3.3mmHg in 4B, and 16.3±4.0mmHg in 4C[280]. They also reported increasing severity and extent of varices, and frequency of esophageal variceal bleeding. Nagula et al, 2005 looked specifically at the effect of septa thickness

and reported a significant correlation between septa thickness and hepatic venous pressure gradient[281].

These data point to a correlation between septa thickness and disease severity, rather than a causal relationship. The septa will thicken with increasing severity and duration of chronic liver injury, which has other effects in the liver (and beyond) besides scar accumulation such as vascular remodeling and hepatocyte senescence. This also does not address whether reversing stages will lower risk, or if the risk remains once that stage has been reached regardless of the current state. However, it is reasonable to believe that the scar itself has some contribution to these findings of increased severity with higher Laennec stages. Hepatocytes in a stiff environment exhibit suppressed albumin production[12], downregulation of cytochrome p450[13] and HNF4α[14] (two markers of hepatocyte differentiation and liver-specific function), as well as changes in a range of genes associated with normal epithelial function[15]. Portal hypertension is the result of both intrahepatic and extrahepatic vascular changes, though increased intrahepatic vascular resistance is the primary cause[282]. Fibrosis and tissue stiffness are believed to directly contribute to the increased resistance by distorting the microvasculature[283, 284]. Activated hepatic stellates cells also increase vascular resistance by contracting around sinusoids[282]. Hepatic stellate cell activation is also influenced by tissue stiffness, due to the fibrosis-stiffness mechanotransduction feedback loop[285, 286]. Taken together, these findings suggest reducing septa thickness likely does have some clinical benefit.

4.4.6 Expression After Shockwave Treatment Suggests Ongoing Remodeling Process

5 of the DEGs correspond to collagen types I (*COL1A1, COL1A2)*, III (*COL3A1*), and VI (*COL6A1, COL6A2)*. There were also several well known genes that have been studied extensively in the setting of fibrosis and tissue remodeling: *MMP2* is a key factor in matrix

degradation[287], *LOXL1* regulates matrix crosslinking[288], and *PDGFRA* encodes a receptor in the PDGF pathway which is broadly involved in fibrosis and repair[289]. Two of the DEGs were related to integrins (*ITGA8*, *ITGBL1*), which are key mediators of cell-matrix signaling involved in matrix remodeling[290, 291]. 20 of the remaining 31 DEGs have also been associated with matrix production (*AEBP1*[292], *SMOC2*[293], *SERPINE2*[294], *SPARCL1*[295], *FBLN5*[296]), matrix degradation (*DPEP1*[297, 298], *MRC2*[299, 300], *CDH17*[301]), or matrix remodeling more broadly (*ADAMTSL2*[302, 303], *CPZ*[304], *TCF21*[305], *OGN*[306], *MGP*[307], *ANXA1*[308], *TGLN*[309, 310], *CYGP*[311], *FSTL1*[312], *IGFBP7*[313], *PZP*[181], *BGN*[314]). All of these DEGs were upregulated in the treated tissue except for *CDH17* and *PZP*, demonstrating activation of both matrix production and degradation processes. Overall, although the RNAseq analysis returned a short list of DEGs, there is a clear theme of ongoing matrix remodeling.

Downregulating expression of collagen genes is a common preclinical metric for anti-fibrotic drugs for liver fibrosis. The progression of liver fibrosis is driven by activation of hepatic stellate cells to a phenotype characterized by high expression of fibrogenic genes, such as *COL1A1*. Studies of innate regression of liver fibrosis have shown that activated hepatic stellate cells either undergo apoptosis or downregulate fibrogenic genes to adopt a phenotype similar to the quiescent state[315]. Therefore, many therapies aim to exert a protective effect and facilitate innate regression by inducing this expression profile[316]. However, collagens are an essential component of normal tissue as well, and their expression is necessary for normal tissue remodeling, repair, and morphogenesis. Research into the stimulated remodeling of skin scars after structural perturbation, such as with the fractional laser, report long-term upregulation of collagen expression after treatment[56, 57, 83, 84]. These expression changes enable the gradual but long-lasting remodeling of scars towards a more normal architecture. The results of the RNAseq analysis coupled with the observed reduction in septa thickness suggest that shockwave treatment stimulates a similar remodeling process.

4.4.7 Shockwave Summary & Future Directions

This data comprises a pilot study demonstrating that shockwave treatment is well tolerated and induces a remodeling response that significantly reduces thickness of the septa. The primary limitation of this study is the small number of animals, particularly with the proposed exclusion of animals based on septa thickness. Our recommendation to AbbVie, the company that developed the RAP device and collaborated with us on this study, was that the next step should be to confirm these results with a much larger cohort.

Multiple treatments could also be investigated to improve efficacy. In this pilot study we investigated a single treatment session due to practical considerations. However, multiple treatments over time would likely achieve a greater effect. The procedure is non-invasive and would not require general anesthesia in humans, so it would be straightforward to perform the treatment at regular intervals and monitor the patient response with liver function panels and elastography.

The current RAP device would likely need to be altered to be effective as a treatment for cirrhosis in humans. The planar wave produced by the device attenuates significantly over a relatively short distance in tissue. This is not a major concern with the small size of rats, but would need to be addressed to achieve sufficient depth in humans. Changing the reflector geometry to focus the shockwave can easily reach any portion of the human liver. The redesigned device would involve scanning the shockwave focus throughout the liver to cover a sufficient treatment volume.

Chapter 5

Conclusions

5.1 Summary of Findings

This thesis was centered around the idea that methods of directly perturbing tissue structure had been under-explored in the search for a treatment for cirrhosis. Our goal was to demonstrate that such approaches are viable and encourage future research to consider similar direct approaches capable of exerting a brief but potent impact on tissue architecture.

In Chapter 2 we discussed microinjury perturbation using the fractional laser, a technique that has shown dramatic success for inducing remodeling of skin scars. This approach was the least successful treatment of the three described here, but it revealed a novel finding about the cirrhotic liver and its susceptibility to injury. We first showed that the healthy liver tolerates the treatment well, but microinjuries in the cirrhotic liver devolve into enlarged and heterogeneous zones of cell death. Using RNAseq analysis, hyperspectral imaging, and tomato lectin perfusion we demonstrated that these exacerbated injuries result from disrupted perfusion of the cirrhotic nodule microvasculature. This is a novel ischemic susceptibility related to the microvascular network architecture and compartmentalization, distinct from the previously described susceptibility due to capillarization and hypoperfusion.

In Chapter 3 we reported that interstitial infusion of purified collagenase clostridium histolyticum (CCH) can rapidly achieve significant histological improvements with minimal toxicity from the activity of the enzyme. This approach was based on the success of direct injection of purified CCH into the dense, highly crosslinked collagenous cord that causes Dupuytren's Contracture. We first described the biodistribution of a macromolecule delivered via interstitial infusion in the liver, and used these results to design an infusion protocol that covers the entire liver with minimal off-target exposure. We then showed that purified CCH reduces collagen proportionate area by 33% while metrics of liver injury were maintained at the same level as infusion of saline.

Finally, in chapter 4 we demonstrated the efficacy of mechanical perturbation from shockwave treatment. We showed that the shockwave had no effect on ex vivo tissue viability and caused only mild liver enzyme elevations in vivo. We then showed the response to the shockwave appeared to have two distinct groups. When the mean septa thickness was below 60μm in the paired untreated lobe, the treated lobe had a significant decrease in septum thickness and collagen proportionate area. Above this threshold,

there was no difference between the treated and untreated lobes. We hypothesized that this represented a ceiling for shockwave efficacy, whereby very thick septa were resistant to shockwave disruption. As part of this study, we also investigated optimal culture methods for cirrhotic precision-cut liver slices, an ex vivo model that maintains resident liver cell populations in their in vivo matrix. This model will be an important tool to support the future development of therapies aimed at exerting structural changes.

5.2 Future Directions

In this thesis we've presented several promising candidate treatments for cirrhosis. However, there is still much work to be done to translate these findings into a treatment that can make a meaningful clinical impact.

The exacerbated injuries limit the applicability of the current fractional laser tool for inducing scar remodeling in cirrhosis. However, alterations to the fractional laser tool could help avoid this issue. Femtosecond lasers can create extremely small injuries, potentially on the size of a single cell. Such a laser would have limited treatment depth, but repetitive pulse stacking with precise targeting may provide sufficient treatment volume. A similar effect could be achieved by focusing the laser to a smaller spot size. A balance would have to be struck between creating small enough injuries to avoid significantly disrupting the microvascular network while still eliciting a sufficiently strong response to drive scar remodeling.

The greatest potential for microinjury perturbation may exist outside of the liver. There are numerous fibrotic conditions occurring throughout the body that would not have the same limitations we discovered here. For example, a fractional laser tool combined with an endoscope may be a promising option for the treatment of gastrointestinal strictures – fibrous bands that can progressively contract over time and cause blockages. Another potential use case is pulmonary fibrosis. Similar to cirrhosis, transplantation is the only

curative treatment option for pulmonary fibrosis. It may be possible to combine a fractional laser with a bronchoscope to perform minimally invasive microinjury treatment. There is a multitude of fibrotic conditions occurring throughout the body, many of which have high morbidity and limited treatment options. The remarkable results of microinjury treatment in the skin warrant further investigation for other applications.

For CCH infusion, the next stage of development will be to confirm efficacy in a rat model of cirrhosis. The rat model develops thicker and more stable fibrous septa, more similar to the disease in humans. Successfully degrading the septa in a rat model would be an encouraging sign that CCH can meaningfully improve scarring in the human liver as well. Future work will also investigate the hypothesis that the dose is currently limited by a shock response. Experiments will be performed to determine changes in inflammatory markers of systemic shock and hypoperfusion after varying doses of CCH infusion. If this hypothesis is confirmed then higher doses may be feasible, as shock can be monitored and mitigated with vasopressors.

The CCH infusion procedure will also need to be refined to be more practical for clinical use. In this work we performed a laparotomy to insert the needle in the liver, but the procedure can be made minimally invasive with ultrasound guidance. Reducing the invasiveness of the procedure will also support experiments to determine whether multiple infusions over time can further improve efficacy.

For the shockwave, the necessary next step is to confirm our findings in a larger cohort. The results we have demonstrated are very promising but limited by the small number of animals, particularly with the proposed exclusion based on septa thickness. This was our primary recommendation to AbbVie, the company that developed the RAP device and collaborated with us on this study. As with CCH infusion, future experiments will also determine whether multiple doses over time be used to improve efficacy.

The clinical application of shockwave treatment is relatively straightforward. The procedure is non-invasive and would not require general anesthesia in humans. Treatment could be performed at regular intervals while monitoring the patient response with liver function panels and elastography.

Throughout this work we focused primarily on achieving structural improvements. As has been discussed in detail in the preceding chapters, there is reason to believe that improving structure will confer significant functional benefits, but this question will need to be directly addressed in future work for these treatments to make it to the clinic.

Great research is being done for the development of antifibrotic drugs that may be effective for earlier stages of liver fibrosis. There is the potential for combining a pharmaceutical treatment with a direct perturbation approach to yield a synergistic effect. For example, drugs aimed at suppressing matrix production and upregulating degradation (e.g., PPAR agonists[317, 318]) may have reduced efficacy against the dense, crosslinked fibrous septa in cirrhosis that are resistant to degradation. However, a high dose CCH infusion or mechanical disruption of the septa via shockwaves may lower the resistance to such a treatment. Similarly, fractional laser treatment could be used to facilitate infiltration of engineered macrophages[319] into the septa. In this way, a one-time or infrequent potent perturbation treatment can synergize with a drug eliciting a more subtle but constant effect. It is also likely that there is some synergy between the treatments discussed in this work. Given the observed limited effect of shockwave treatment against very thick septa, mechanically weakening the scar tissue via CCH infusion may raise the ceiling for efficacy.

5.3 Concluding Remarks

The fundamental mechanisms of fibrosis are consistent wherever it occurs in the body. A treatment that is proven to be capable of inducing remodeling of scar in the skin warrants

investigation for other organs, especially when few current treatment options exist. Drugs are commonly tested across indications with similar mechanisms, but this has not extended to the type of treatments described in this thesis. Overall, the work presented here makes a strong case that direct perturbation approaches are viable for cirrhosis, and we believe that similar approaches should be investigated for other fibrotic conditions throughout the body.

Appendix A: Microinjury Perturbation Supplement

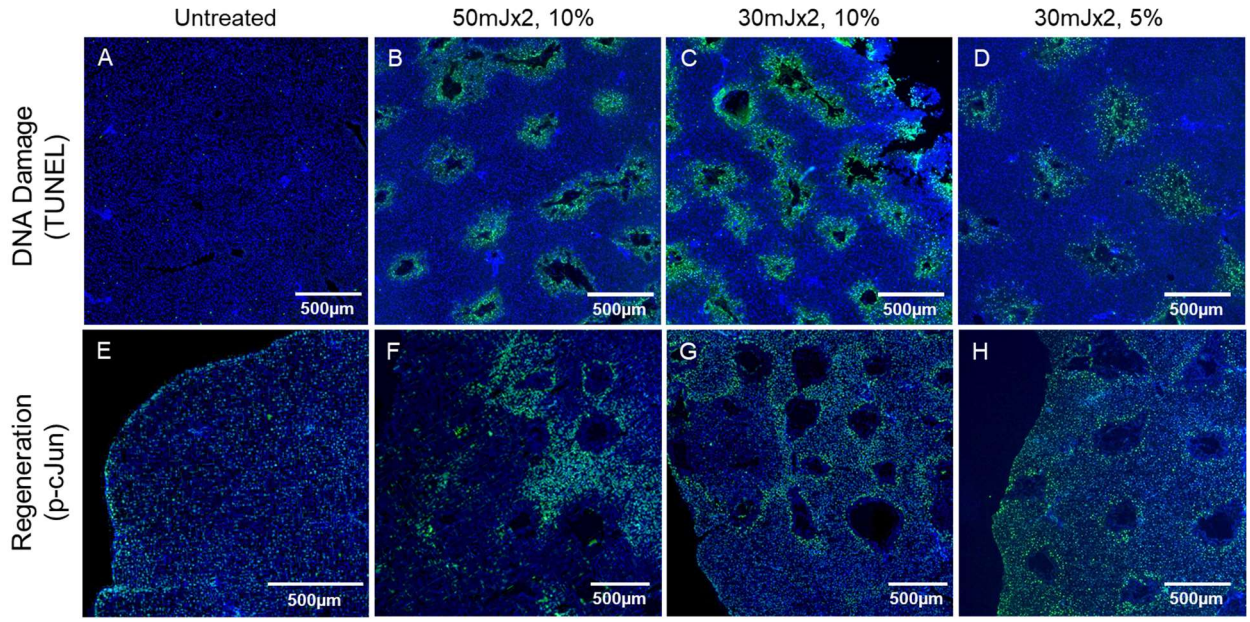

Appendix Figure A-1: Injury pattern at 2hrs after fractional laser ablation in the healthy liver for various treatment intensities. TUNEL stains DNA damage and shows cells directly injured by the laser. Phospho-cJun is an early marker of liver regeneration and should be expressed in hepatocytes surrounding an injury. The ideal pattern would have positive phospo-cJun staining bordering every individual microinjury (A,E) Untreated tissue has no positive TUNEL staining and homogenous phospho-cJun staining. (B,F) 2 pulses of 50mJ at 10% density. A few injury sites are isolated (clearly surrounded by positive phospho-cJun staining), but most are not, indicating coalescence of the microinjuries into a larger injury. (C,G) 2 pulses of 30mJ at 10% density. Most injuries are isolated but there is one region where several adjacent microinjuries coalesced into a larger injury. (D,H) 2 pulses of 30mJ at 5% density. Reducing the density of injury sites created a clear pattern of isolated microinjuries. 15mJx2, 5% density was then chosen for the remaining experiments to be comfortably below this threshold while still maintaining the desired minimum treatment depth. (n=3 per group)

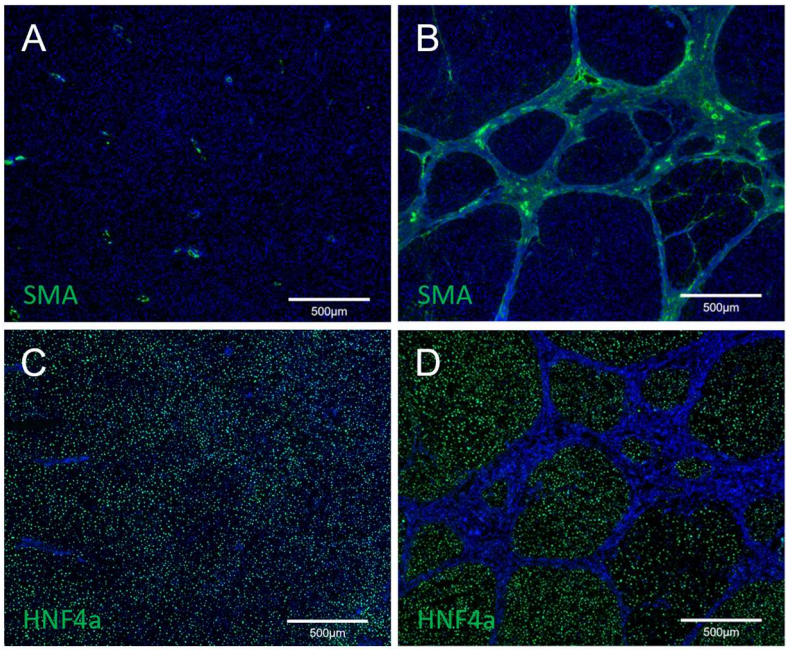

Appendix Figure A-2: Representative untreated immunofluorescence reference images for the healthy and cirrhotic liver. (A) SMA stain of healthy liver. (B) SMA stain of cirrhotic liver. (C) HNF4a stain of healthy liver. (D) HNF4a stain of cirrhotic liver.

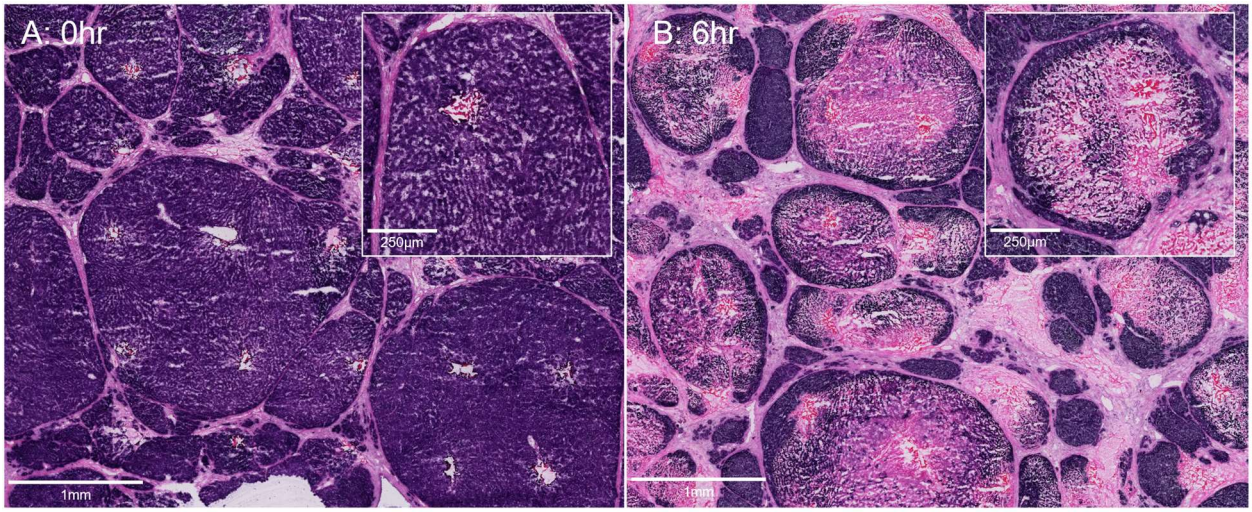

Appendix Figure A-3: Representative NBTC viability stain in the cirrhotic liver (A) immediately and (B) 6hrs after fractional laser treatment. Viable cells are stained purple. Regions without viable cells are stained pink by the eosin counterstain. (A) Immediately after treatment only the few cells directly ablated by the laser are dead. (B) By 6hr, enlarged and heterogeneous zones of cell death have developed with few viable cells. There is a band of viable cells around the edge of the nodule near the septa. (n=3)

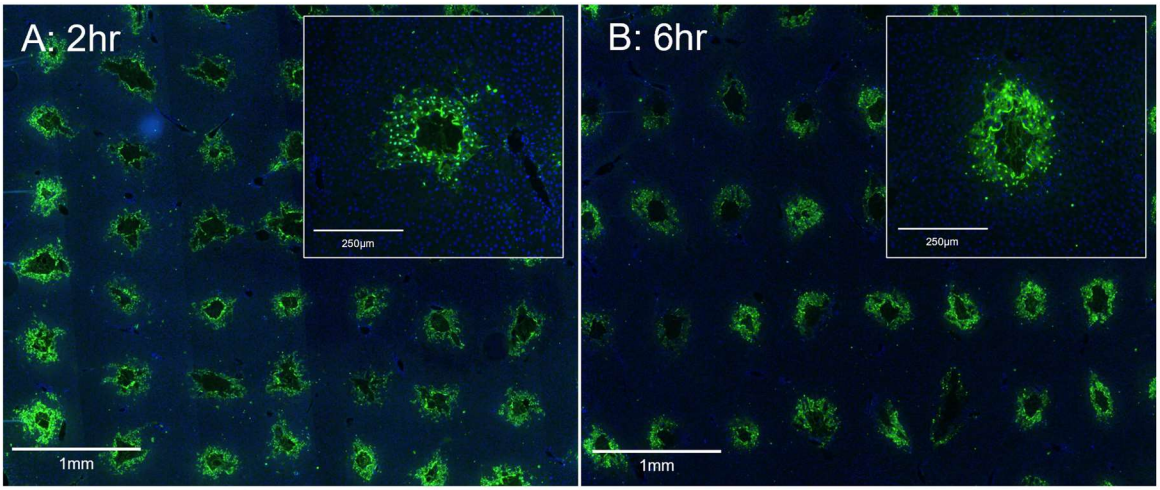

Appendix Figure A-4: Representative TUNEL stain in the healthy liver (A) 2hr and (B) 6hrs after fractional laser treatment. Cell death is limited to the region immediately surrounding the laser ablation site and there is no change in the injury pattern from 2 to 6hrs. (n=3 per timepoint)

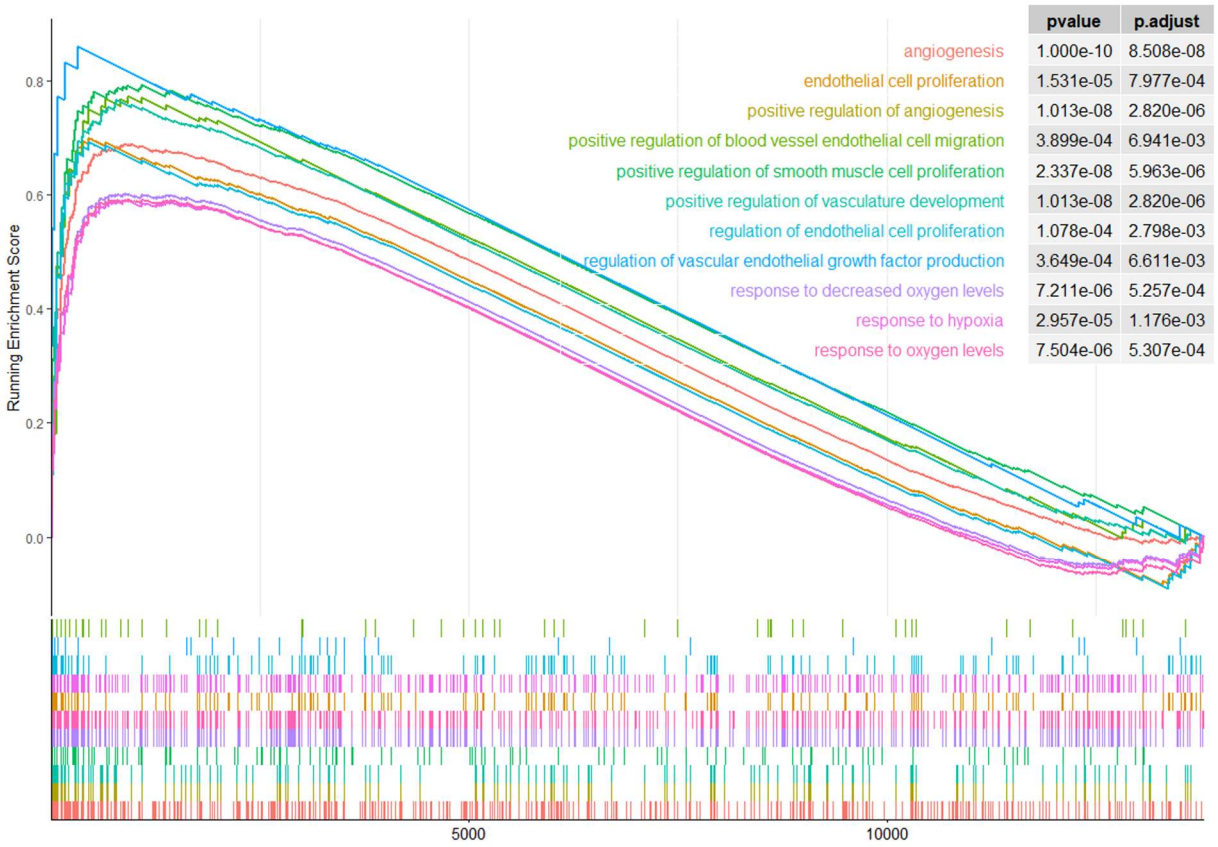

Appendix Figure A-5: Gene Set Enrichment Analysis (GSEA) of RNAseq results comparing healthy and cirrhotic liver at 4hrs after fractional laser ablation. 4 healthy and 4 cirrhotic animals were used for this analysis, with a laser-treated and untreated control sample taken from each animal. The running enrichment score and adjusted p-value are shown for selected gene sets related to hypoxia and angiogenesis. (n=4)

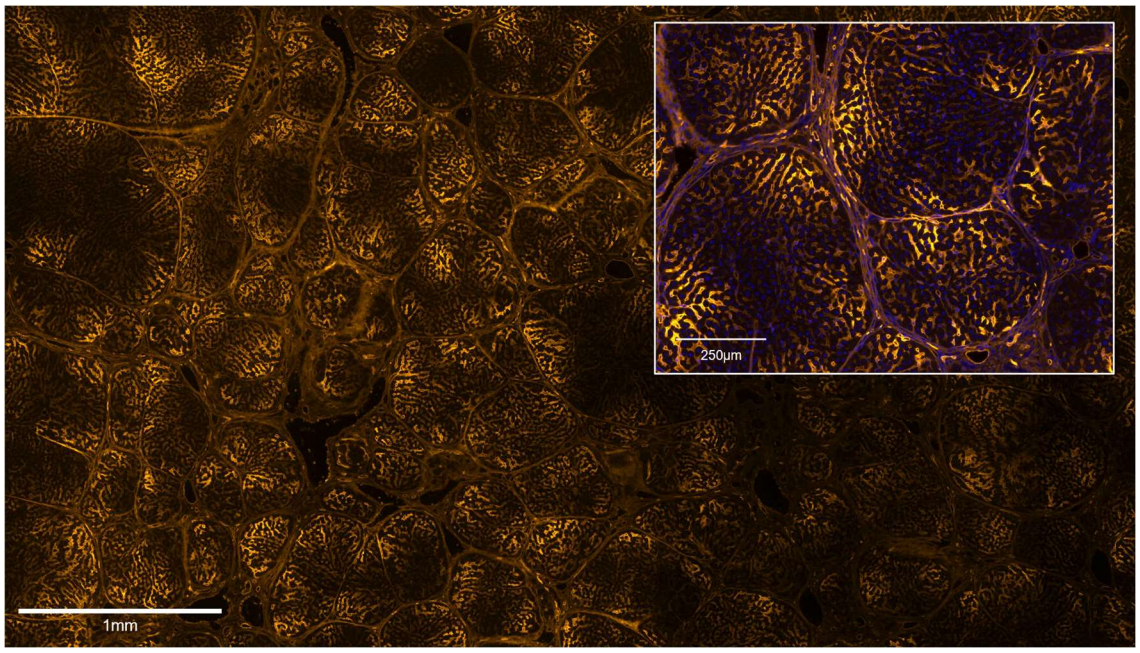

Appendix Figure A-6: Representative tomato lectin reference stain of untreated cirrhotic liver. The inset image is also stained with DAPI. (n=3)

Appendix B: Lytic Perturbation Supplement

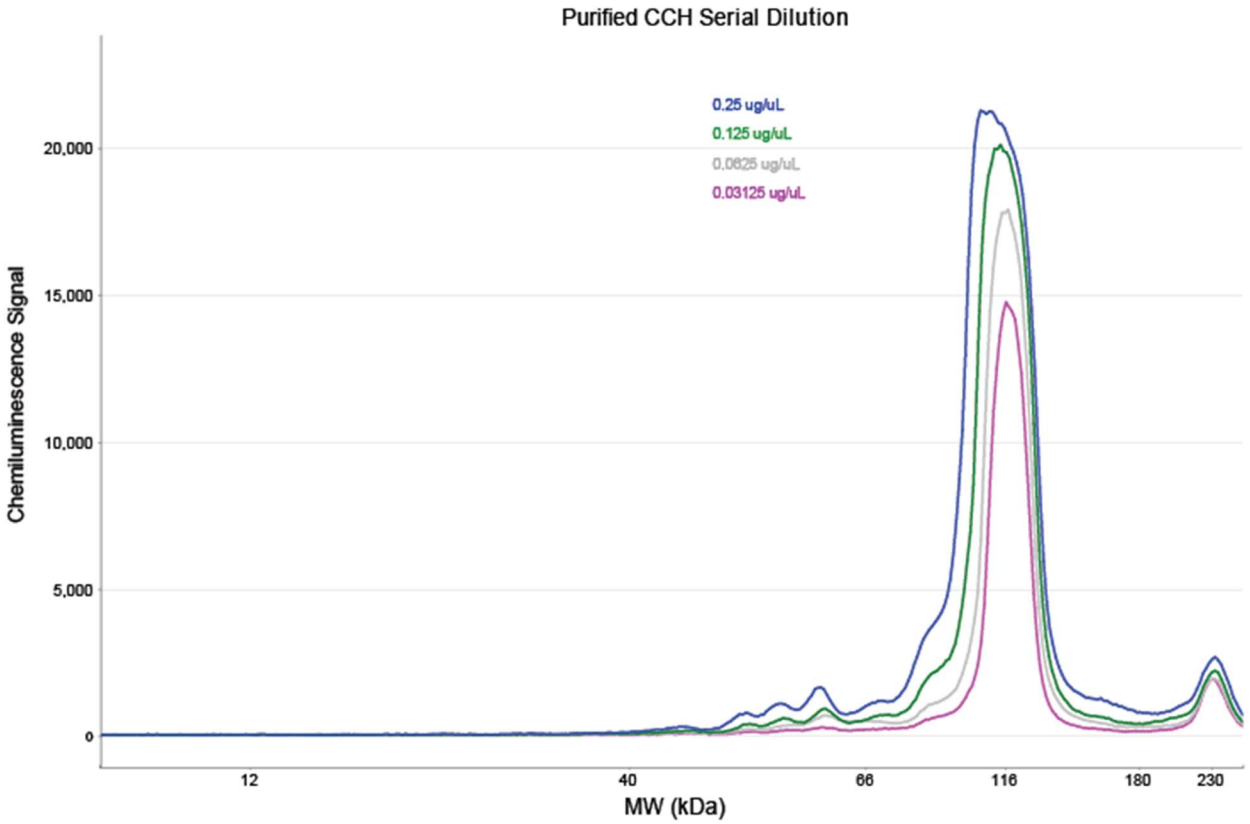

Appendix Figure B-1: Molecular Weight Analysis for Serial Dilution of Purified CCH. The small peak at 230kDa remains relatively consistent across the dilutions, indicating it is a loading artifact rather than a component of the CCH.

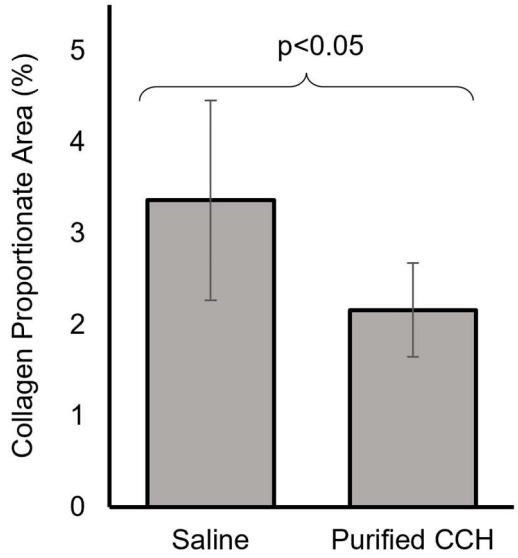

Appendix Figure B-2: Changes in fibrosis in the non-infused (left) lobe 5d after interstitial infusion of purified CCH in the cirrhotic liver. Quantification of collagen in saline and CCH infused samples. Purified CCH caused a significant decrease in collagen proportionate area. (n=4 saline control; n=6 CCH treated)

Appendix C: Mechanical Perturbation Supplement

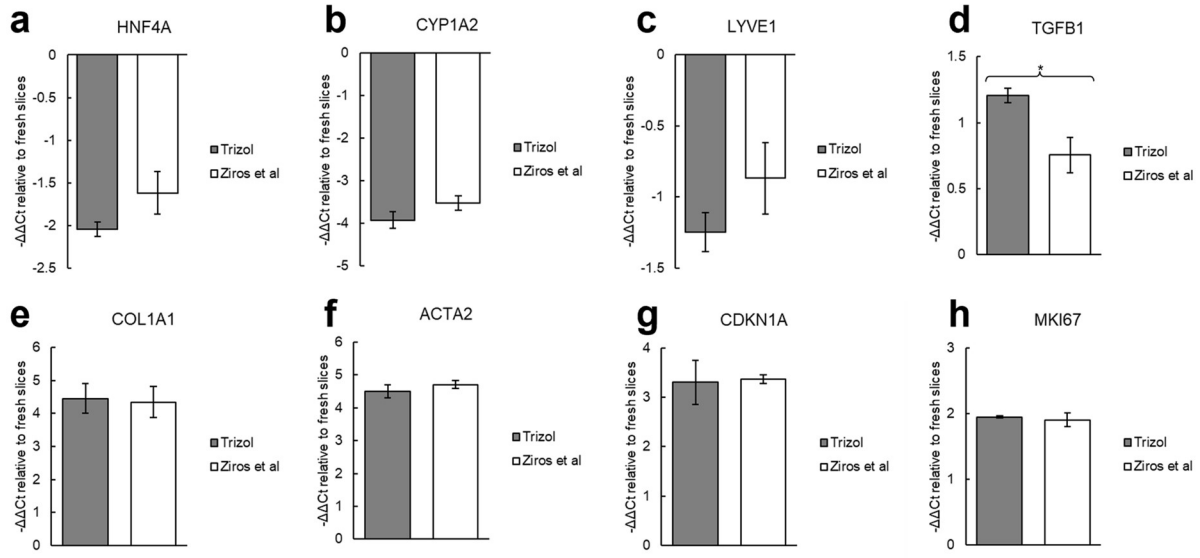

Appendix Figure C-1: PCR results for RNA isolated with TRIzol protocol or Ziros et al. protocol from cirrhotic PCLS after 4 days in culture. (n=3; p-value calculated with t-test and corrected with the Benjamini-Hochberg procedure; *p<0.05)

Time in Culture	Yield (µg/mg tissue)	$A^{260}/_{280}$	$A^{260}/_{230}$
Fresh Slices	6.3±1.8	2.08±0.02	2.1±0.1
4d	2.3±0.9*	2.03±0.03*	1.9±0.4

Table C-1: Yield and purity metrics for RNA isolated from fresh cirrhotic PCLS and after 4 days in culture. RNA was isolated with the protocol described by Ziros et al. (n=6; p-value calculated with t-test, *p<0.05)

References

1. Global Health Estimates 2020: Disease burden by Cause, Age, Sex, by Country and by Region, 2000-2019: World Health Organization, 2020.

2. Global Health Estimates 2020: Deaths by Cause, Age, Sex, by Country and by Region, 2000-2019: World Health Organization, 2020.

3. Mokdad A, Lopez A, Shahraz S, et al. Liver cirrhosis mortality in 187 countries between 1980 and 2010: a systematic analysis. BMC Medicine 2014;12:145.

4. Kumar V, Abbas A, Aster J. Pathologic Basis of Disease: Elsevier Saunders, 2015.

5. Barr RG, Ferraioli G, Palmeri ML, et al. Elastography Assessment of Liver Fibrosis: Society of Radiologists in Ultrasound Consensus Conference Statement. Radiology 2015;276:845-61.

6. Fernandez M, Semela D, Bruix J, et al. Angiogenesis in liver disease. J Hepatol 2009;50:604-620.

7. Tsochatzis E, Bosch J, Burroughs A. Liver cirrhosis. The Lancet 2014;383:17-23.

8. Mori T, Okanoue T, Sawa Y, et al. Defenestration of the sinusoidal endothelial cell in a rat model of cirrhosis. Hepatology 1993;17:891-7.

9. Schuppan D, Afdhal NH. Liver cirrhosis. Lancet 2008;371:838-51.

10. Desmet V, Roskams T. Cirrhosis reversal: a duel between dogma and myth. J Hepatol 2004;40:860-867.

11. Pellicoro A, Ramachandran P, Iredale J, et al. Liver fibrosis and repair: immune regulation of wound healing in a solid organ. Nat Rev Immunol 2014;14:181-194.

12. Semler EJ, Ranucci CS, Moghe PV. Mechanochemical manipulation of hepatocyte aggregation can selectively induce or repress liver-specific function. Biotechnol Bioeng 2000;69:359-69.

13. Semler EJ, Lancin PA, Dasgupta A, et al. Engineering hepatocellular morphogenesis and function via ligand-presenting hydrogels with graded mechanical compliance. Biotechnol Bioeng 2005;89:296-307.

14. Desai SS, Tung JC, Zhou VX, et al. Physiological ranges of matrix rigidity modulate primary mouse hepatocyte function in part through hepatocyte nuclear factor 4 alpha. Hepatology 2016;64:261-75.

15. Xia T, Zhao R, Feng F, et al. Gene expression profiling of human hepatocytes grown on differing substrate stiffness. Biotechnol Lett 2018;40:809-818.

16. Aravinthan AD, Alexander GJM. Senescence in chronic liver disease: Is the future in aging? J Hepatol 2016;65:825-834.

17. Huda N, Liu G, Hong H, et al. Hepatic senescence, the good and the bad. World J Gastroenterol 2019;25:5069-5081.

18. Blokland KEC, Pouwels SD, Schuliga M, et al. Regulation of cellular senescence by extracellular matrix during chronic fibrotic diseases. Clin Sci (Lond) 2020;134:2681-2706.

19. Regnault V, Challande P, Pinet F, et al. Cell senescence: basic mechanisms and the need for computational networks in vascular ageing. Cardiovasc Res 2020.

20. Hove C, Williams E, Rodgers B. Z-plasty: a concise review. Facial Plast Surg 2001;17:289-294.

21. Boyce S, Kagan R, Greenhalgh D, et al. Cultured skin substitutes reduce requirements for harvesting of skin autograft for closure of excised, full-thickness burns. J Trauma 2006;60:821-829.

22. Anderson R, Donelan M, Hivnor C, et al. Laser treatment of traumatic scars with an emphasis on ablative fractional laser resurfacing: consensus report. JAMA Dermatol 2014;150:187-93.

23. Stumpp O, Bedi V, Wyatt D, et al. In vivo confocal imaging of epidermal cell migration and dermal changes post nonablative fractional resurfacing: study of the wound healing process with corroborated histopathologic evidence. J Biomed Opt 2009;14:024018.

24. Beachofsky T, Henning J, Hivnor C. Induction of de novo hair regeneration in scars after fractionated carbon dioxide laser therapy in three patients. Dermatol Surg 2011;37:1365-1368.

25. Neiner J, Whittemore D, Hivnor C. Buried alive: functional eccrine coils buried under scar tissue? J Am Acad Dermatol 2011;65:661-663.

26. Shumaker P, Kwan J, Landers J, et al. Functional improvements in traumatic scars and scar contractures using an ablative fractional laser protocol. J Trauma Acute Care Surg 2012;73:S116-21.

27. Issler-Fisher AC, Fisher OM, Smialkowski AO, et al. Ablative fractional CO2 laser for burn scar reconstruction: An extensive subjective and objective short-term outcome analysis of a prospective treatment cohort. Burns 2017;43:573-582.

28. Hultman CS, Friedstat JS, Edkins RE, et al. Laser resurfacing and remodeling of hypertrophic burn scars: the results of a large, prospective, before-after cohort study, with long-term follow-up. Ann Surg 2014;260:519-29; discussion 529-32.

29. El-Zawahry BM, Sobhi RM, Bassiouny DA, et al. Ablative CO2 fractional resurfacing in treatment of thermal burn scars: an open label controlled clinical and histopathological study. J Cosmet Dermatol 2015;14:324-331.

30. Eckersley JR, Dudley HA. Wounds and wound healing. Br Med Bull 1988;44:423-436.

31. Liu F, Mih JD, Shea BS, et al. Feedback amplification of fibrosis through matrix stiffening and COX-2 suppression. J Cell Biol 2010;190:693-706.

32. Qu L, Liu A, Zhou L, et al. Clinical and molecular effects on mature burn scars after treatment with a fractional CO2 laser. Lasers Surg Med 2012;44:517-524.

33. Reilly MJ, Cohen M, Hokugo A, et al. Molecular effects of fractional carbon dioxide laser resurfacing on photodamaged human skin. Arch Facial Plast Surg 2010;12:321-325.

34. Orringer JS, Rittié L, Baker D, et al. Molecular mechanisms of nonablative fractionated laser resurfacing. Br J Dermatol 2010;163:757-768.

35. Schumaker PR, Kwan JM, Landers JT, et al. Functional improvements in traumatic scars and scar contractures using an ablative fractional laser protocol. J Trauma ACute Care Surg 2012;73:S116-21.

36. Moore AL, Marshall CD, Barnes LA, et al. Scarless wound healing: Transitioning from fetal research to regenerative healing. Wiley Interdiscip Rev Dev Biol 2018;7.

37. Laubach HJ, Tannous Z, Anderson RR, et al. Skin responses to fractional photothermolysis. Lasers Surg Med 2006;38:142-9.

38. Carniol PJ, Hamilton MM, Carniol ET. Current Status of Fractional Laser Resurfacing. JAMA Facial Plast Surg 2015;17:360-6.

39. Manstein D, Herron GS, Sink RK, et al. Fractional photothermolysis: a new concept for cutaneous remodeling using microscopic patterns of thermal injury. Lasers Surg Med 2004;34:426-38.

40. Sadick NS, Smoller B. A study examining the safety and efficacy of a fractional laser in the treatment of photodamage on the hands. J Cosmet Laser Ther 2009;11:29-33.

41. Spandau DF, Lewis DA, Somani AK, et al. Fractionated laser resurfacing corrects the inappropriate UVB response in geriatric skin. J Invest Dermatol 2012;132:1591-6.

42. Connolly KL, Chaffins M, Ozog D. Vascular patterns in mature hypertrophic burn scars treated with fractional CO2 laser. Lasers Surg Med 2014;46:597-600.

43. Alster T, Tanzi E, Lazarus M. The use of fractional photothermolysis for the treatment of atrophic scars. Dermatol Surg 2007;33:295-299.

44. Schumaker P, Kwan J, Landers J, et al. Functional improvements in traumatic scars and scar contractures using an ablative fractional laser protocol. J Trauma ACute Care Surg 2012;73:S116-21.

45. Beachkofsky TM, Henning JS, Hivnor CM. Induction of de novo hair regeneration in scars after fractionated carbon dioxide laser therapy in three patients. Dermatol Surg 2011;37:1365-8.

46. Ozog DM, Liu A, Chaffins ML, et al. Evaluation of clinical results, histological architecture, and collagen expression following treatment of mature burn scars with a fractional carbon dioxide laser. JAMA Dermatol 2013;149:50-7.

47. Makboul M, Makboul R, Abdelhafez A, et al. Evaluation of the effect of fractional CO2 laser on histopathological picture and TGF-β1 expression in hypertrophic scar. J Cosmet Dermatol 2014;13:169-179.

48. Magnani L, Schweiger E. Fractional CO2 lasers for the treatment of atrophic acne scars: a review of the literature. J Cosmet Laser Ther 2014;16:48-56.

49. Xu X, Luo Y, Wu Y, et al. Immunohistological evaluation of skin responses after treatment using a fractional ultrapulse carbon dioxide laser on back skin. Dermatol Surg 2011;37:1141-1149.

50. Baca M, Neaman K, Rapp D, et al. Reduction of post-surgical scarring with the use of ablative fractional CO2 lasers: a pilot study using a porcine model. Lasers Surg Med 2017;49:122-128.

51. Douglas H. TGF-β in wound healing: a review. J Wound Care 2010;19:403-406.

52. Hinz B. The extracellular matrix and transforming growth factor-β1: Tale of a strained relationship. Matrix Biol 2015:54-65.

53. Lichtman M, Otero-Vina M, Falanga V. Transforming growth factor beta (TGF-β) isoforms in wound healing and fibrosis. Wound Repair and Regeneration 2016;24:215-222.

54. Ramirez H, Patel SB, Pastar I. The Role of TGFbeta Signaling in Wound Epithelialization. Adv Wound Care (New Rochelle) 2014;3:482-491.

55. Prignano F, Campolmi P, Bonan P, et al. Fractional CO2 laser: a novel therapeutic device upon photobiomodulation of tissue remodeling and cytokine pathway of tissue repair. Dermatol Ther 2009;22:S8-15.

56. DeBruler D, Blackstone B, Baumann B, et al. Inflammatory responses, matrix remodelling, and re-epithelialization after fractional CO2 laser treatment of scars. Lasers Surg Med 2017;49:675-685.

57. Qu L, Liu A, Zhou L, et al. Clinical and molecular effects on mature burn scars after treatment with a fractional CO2 laser. Lasers Surg Med 2012;44:517-524.

58. Shah M, Foreman D, Ferguson M. Neutralisation of TGF-β1 and TGF-β2 or exogenous addition of TGF-β3 to cutaneous rat wounds reduces scarring. J Cell Sci 1995:985-1002.

59. Feder M, Hofmann G. Heat-shock proteins, molecular chaperones, and the stress response: evolutionary and ecological physiology. Annu Rev Physiol 1999;61:243-82.

60. Saibil H. Chaperone machines for protein folding, unfolding and disaggregation. Nat Rev Mol Cell Biol 2015;14:630-642.

61. Atalay M, Oksala N, Lappalainen J, et al. Heat shock proteins in diabetes and wound healing. Curr Protein Pept Sci 2009;10:85-95.

62. Bellaye PS, Burgy O, Causse S, et al. Heat shock proteins in fibrosis and wound healing: good or evil? Pharmacol Ther 2014;143:119-132.

63. Wrighton KH, Lin X, Feng XH. Critical regulation of TGFbeta signaling by Hsp90. Proc Natl Acad Sci U S A 2008;105:9244-9249.

64. Yun CH, Yoon SY, Nguyen TT, et al. Geldanamycin inhibits TGF-beta signalinng through induction of Hsp70. Arch Biochem Biophys 2010;495:8-13.

65. Sakai G, Tokuda H, Fujita K, et al. Heat shock protein 70 negatively regulates TGF-beta stimulated VEGF synthesis via p38 MAP kinase in osteoblasts. Cell Physiol Biochem 2017;44:1133-1145.

66. Shang Y, Xu X, Duan X, et al. Hsp70 and Hsp90 oppositely regulate TGF-beta signaling through CHIP/Stub1. Biochem Biophys Res Commun 2014;446:387-392.

67. Abu-Elsaad NM, Serrya MS, El-Karef AM, et al. The heat shock protein 90 inhibitor, 17-AAG, attenuates thioacetamide induced liver fibrosis in mice. Pharmacol Rep 2016;68:275-282.

68. Noh H, Kim HJ, Yu MR, et al. Heat shock protein 90 inhibitor attenuates renal fibrosis through degradtaion of transforming growth factor beta type II receptor. Lab Invest 2012;92:1583-1596.

69. He W, Zhuang Y, Wang L, et al. Geranylgeranylacetone attenuates hepatic fibrosis by increasing the expression of heat shock protein 70. Mol Med Rep 2015;12:4895-4900.

70. Tanaka K, Tanaka Y, Namba T, et al. Heat shock protien 70 protects against bleomycin-induced pulmonary fibrosis in mice. Biochem Pharmacol 2010;80:920-931.

71. Nagata K. Expression and function of heat shock protein 47: a collagen-specific molecular chaperone in the endoplasmic reticulum. Matrix Biol 1998;16:379-386.

72. Helbig D, Bodenforf M, Grunewald S, et al. Immunohistochemical investigation of wound healing in response to fractional photothermolysis. J Biomed Opt 2009;14:06044.

73. Orringer J, Rittié L, Baker D, et al. Molecular mechanisms of nonablative fractionated laser resurfacing. Br J Dermatol 2010;163:757-768.

74. Laubach H, Tannous Z, Anderson R, et al. Skin responses to fractional photothermolysis. Lasers Surg Med 2006;38:142-149.

75. Hantash B, Bedi V, Struck S, et al. Immunohistochemical evaluation of the heat shock response to nonablative fractional resurfacing. J Biomed Opt 2010;15:068002.

76. Helbig D, Mobius A, Simon JC, et al. Heat shock protein 70 expression patterns in dermal explants in response to ablative fractional phothothermolysis, microneedle, or scalpel wounding. Wounds 2011;23:59-67.

77. Manuskiatti W, Pattanaprichakul P, Inthasotti S, et al. Thermal Response of In Vivo Human Skin to Fractional Radiofrequency Microneedle Device. Biomed Res Int 2016;2016:6939018.

78. Oberringer M, Baum HP, Jung V, et al. Differential expression of heat shock protein 70 in well healing and chronic human wound tissue. Biochem Biophys Res Commun 1995;214:1009-14.

79. McMurty A, Cho K, Young L, et al. Expression of HSP70 in healing wounds of diabetic and nondiabetic mice. J Surg Res 1999;86:36-41.

80. Cox TR, Erler JT. Remodeling and homeostasis of the extracellular matrix: implications for fibrotic diseases and cancer. Dis Model Mech 2011;4:165-178.

81. Kupai K, Szucs G, Cseh S, et al. Matrix metalloproteinase activity assays: Importance of zymography. J Pharmacol Toxicol Methods 2010;61:205-209.

82. Reilly M, Cohen M, Hokugo A, et al. Molecular effects of fractional carbon dioxide laser resurfacing on photodamaged human skin. Arch Facial Plast Surg 2010;12:321-325.

83. Orringer J, Kang S, Johnson T, et al. Connective tissue remodeling induced by carbon dioxide laser resurfacing of photodamaged human skin. JAMA 2004;140:1326-1332.

84. Jiang X, Ge H, Zhou C, et al. The role of vascular endothelial growth factor in fractonal laser resurfacing with the carbon dioxide laser. Lasers Med Sci 2012;27:599-606.

85. Broughton GI, Janis JE, Attinger CE. The basic science of wound healing. Plast Reconstr Surg 2006;117:12S-34S.

86. Perez-Garijo A, Steller H. Spreading the word: non-autonomous effects of apoptosis during development, regeneration and disease. Development 2015;142:3253-62.

87. Bergmann A, Steller H. Apoptosis, stem cells, and tissue regeneration. Sci Signal 2010;3:re8.

88. Vriz S, Reiter S, Galliot B. Cell death: a program to regenerate. Curr Top Dev Biol 2014;108:121-51.

89. Prignano F, Ricceri F, Bonan P, et al. Induction of apoptosis by fractional CO2 laser treatment. J Cosmet Laser Ther 2012;14:267-71.

90. Farkas JP, Richardson JA, Burrus CF, et al. In vivo histopathologic comparison of the acute injury following treatment with five fractional ablative laser devices. Aesthet Surg J 2010;30:457-64.

91. Ciani L, Krylova O, Smalley MJ, et al. A divergent canonical WNT-signaling pathway regulates microtubule dynamics: dishevelled signals locally to stabilize microtubules. J Cell Biol 2004;164:243-53.

92. Clevers H, Loh KM, Nusse R. Stem cell signaling. An integral program for tissue renewal and regeneration: Wnt signaling and stem cell control. Science 2014;346:1248012.

93. Fernandes JR, Samayoa JC, Broelsch GF, et al. Micro-mechanical fractional skin rejuvenation. Plast Reconstr Surg 2013;131:216-23.

94. Bao P, Kodra A, Tomic-Canic M, et al. The role of vascular endothelial growth factor in wound healing. J Surg Res 2009;153:347-58.

95. Johnson K, TA W. Vascular endothelial growth factor and angiogenesis in the regulation of cutaneous wound repair. Adv Wound Care (New Rochelle) 2014;3:647-661.

96. Dews M, Fox JL, Hultine S, et al. The myc-miR17~92 axis blunts TGFbeta signaling and production of multiple TGFbeta dependent antiangiogenic factors. Cancer Res 2010;70:8233-8246.

97. Dakhlallah D, Batte K, Wang Y, et al. Epigenetic regulation of miR-17~92 contributes to the pathogenesis of pulmonary fibrosis. Am J Respir Crit Care Med 2013;187:397-405.

98. Geng H, Guan J. MiR-18a-5p inhibits endothelial-mesenchymal transition and cardiac fibrosis through the Notch2 pathway. Biochem Biophys Res Commun 2017;491:329-336.

99. Kim J, Won C, Bak H, et al. Gene profiling analysis of the early effects of ablative fractional carbon dioxide laser treatment on human skin. Dermatol Surg 2013;39:1033-1043.

100. Doddaballapur S. Microneedling with Dermaroller. J Cutan Aesthet Surg 2009;2:110-111.

101. Hou A, Cohen B, Haimovic A, et al. Microneedling: A comprehensive review. Dermatol Surg 2017;43:321-339.

102. Liebl H, Kloth LC. Skin cell proliferation stimulated by microneedles. J Am Coll Clin Wound Spec 2012;4:2-6.

103. Alster TS, Graham PM. Microneedling: A review and practical guide. Dermatol Surg 2018;44:397-404.

104. Sadick N, Rothaus KO. Minimally invasive radiofrequency devices. Clin Plast Surg 2016;43:567-575.

105. Hantash BM, Ubeid AA, Chang H, et al. Bipolar fractional radiofrequency treatment induces neoelastogenesis and neocollagenesis. Lasers Surg Med 2009;41:1-9.

106. Sun W, Zhang C, Zhao J, et al. Comparison of moderate and high energy of a nano-fractional radiofrequency treatment on a photoaging hairless mice model. Dermatol Surg 2018;44:569-575.

107. Vater CA, Harris EDJ, Siegel RC. Native cross-links in collagen fibrils induce resistance to human synovial collagenase. Biochem J 1979;181:639-645.

108. Issa R, Zhou X, Constandinou CM, et al. Spontaneous recovery from micronodular cirrhosis: evidence for incomplete resolution associated with matrix cross-linking. Gastroenterology 2004;126:1795-1808.

109. Nimni M. Collagen: structure, function, and metabolism in normal and fibrotic tissues. Semin Arthritis Rheum 1983;13:1-86.

110. Cohen I, Keiser H. Disruption of healed scars in scurvy -- the result of a disequilibrium in collagen metabolism. Plast Reconstr Surg 1976;57:213-215.

111. Eckersley J, Dudley H. Wounds and wound healing. Br Med Bull 1988;44:423-436.

112. Fausto N. Liver regeneration. J Hepatol 2000;32:19-31.

113. Andrews S. FastQC: a quality control tool for high throughput sequence data. Available online at: http://www.bioinformatics.babraham.ac.uk/projects/fastqc, 2010.

114. Martin M. Cutadapt removes adapter sequences from high-throughput sequencing reads. EMBnet J 2011;17:3.

115. Patro R, Duggal G, Love MI, et al. Salmon provides fast and bias-aware quantification of transcript expression. Nat Methods 2017;14:417-419.

116. Love MI, Huber W, Anders S. Moderated estimation of fold change and dispersion for RNA-seq data with DESeq2. Genome Biol 2014;15:550.

117. Wu T, Hu E, Xu S, et al. clusterProfiler 4.0: A universal enrichment tool for interpreting omics data. Innovation (Camb) 2021;2:100141.

118. Zhu A, Ibrahim JG, Love MI. Heavy-tailed prior distributions for sequence count data: removing the noise and preserving large differences. Bioinformatics 2019;35:2084-2092.

119. Yu G. enrichplot: Visualization of Functional Enrichment Result. R package version 1.12.2 ed, 2021.

120. Lu G, Fei B. Medical hyperspectral imaging: a review. J Biomed Opt 2014;19:10901.

121. Wanless IR, Wong F, Blendis LM, et al. Hepatic and portal vein thrombosis in cirrhosis: possible role in development of parenchymal extinction and portal hypertension. Hepatology 1995;21:1238-47.

122. Haratake J, Hisaoka M, Yamamoto O, et al. Morphological changes of hepatic microcirculation in experimental rat cirrhosis: a scanning electron microscopic study. Hepatology 1991;13:952-6.

123. Yamamoto T, Kobayashi T, Phillips MJ. Perinodular arteriolar plexus in liver cirrhosis. Scanning electron microscopy of microvascular casts. Liver 1984;4:50-4.

124. Sherman IA, Pappas SC, Fisher MM. Hepatic microvascular changes associated with development of liver fibrosis and cirrhosis. Am J Physiol 1990;258:H460-5.

125. Vollmar B, Siegmund S, Menger MD. An intravital fluorescence microscopic study of hepatic microvascular and cellular derangements in developing cirrhosis in rats. Hepatology 1998;27:1544-53.

126. Iwakiri Y, Groszmann RJ. Vascular endothelial dysfunction in cirrhosis. J Hepatol 2007;46:927-34.

127. Cai J, Hu M, Chen Z, et al. The roles and mechanisms of hypoxia in liver fibrosis. J Transl Med 2021;19:186.

128. Poisson J, Lemoinne S, Boulanger C, et al. Liver sinusoidal endothelial cells: Physiology and role in liver diseases. J Hepatol 2017;66:212-227.

129. Martinez-Hernandez A, Martinez J. The role of capillarization in hepatic failure: studies in carbon tetrachloride-induced cirrhosis. Hepatology 1991;14:864-74.

130. Waseem N, Chen PH. Hypoxic Hepatitis: A Review and Clinical Update. J Clin Transl Hepatol 2016;4:263-268.

131. Faber JE, Chilian WM, Deindl E, et al. A brief etymology of the collateral circulation. Arterioscler Thromb Vasc Biol 2014;34:1854-9.

132. Toriumi H, Tatarishvili J, Tomita M, et al. Dually supplied T-junctions in arteriolo-arteriolar anastomosis in mice: key to local hemodynamic homeostasis in normal and ischemic states? Stroke 2009;40:3378-83.

133. van Horssen P, Siebes M, Spaan JA, et al. Innate collateral segments are predominantly present in the subendocardium without preferential connectivity within the left ventricular wall. J Physiol 2014;592:1047-60.

134. Rappaport AM, MacPhee PJ, Fisher MM, et al. The scarring of the liver acini (Cirrhosis). Tridimensional and microcirculatory considerations. Virchows Arch A Pathol Anat Histopathol 1983;402:107-37.

135. Donaldson J, Haddad B, Khan WS. The pathophysiology, diagnosis and current management of acute compartment syndrome. Open Orthop J 2014;8:185-93.

136. Wanless IR. The Role of Vascular Injury and Congestion in the Pathogenesis of Cirrhosis: the Congestive Escalator and the Parenchymal Extinction Sequence. Current Hepatology Reports 2020;19:40-53.

137. van Riel WG, van Golen RF, Reiniers MJ, et al. How much ischemia can the liver tolerate during resection? Hepatobiliary Surg Nutr 2016;5:58-71.

138. Rubbia-Brandt L. Sinusoidal obstruction syndrome. Clin Liver Dis 2010;14:651-68.

139. Tripodi A, Mannucci PM. The coagulopathy of chronic liver disease. N Engl J Med 2011;365:147-56.

140. Reinisch L. Scatter-limited phototherapy: a model for laser treatment of skin. Lasers Surg Med 2002;30:381-8.

141. Dewhirst MW, Viglianti BL, Lora-Michiels M, et al. Basic principles of thermal dosimetry and thermal thresholds for tissue damage from hyperthermia. Int J Hyperthermia 2003;19:267-94.

142. van Rhoon GC, Samaras T, Yarmolenko PS, et al. CEM43°C thermal dose thresholds: a potential guide for magnetic resonance radiofrequency exposure levels? Eur Radiol 2013;23:2215-27.

143. Prionas SD, Taylor MA, Fajardo LF, et al. Thermal sensitivity to single and double heat treatments in normal canine liver. Cancer Res 1985;45:4791-7.

144. Yarmolenko PS, Moon EJ, Landon C, et al. Thresholds for thermal damage to normal tissues: an update. Int J Hyperthermia 2011;27:320-43.

145. Ledon JA, Savas J, Franca K, et al. Intralesional treatment for keloids and hypertrophic scars: a review. Dermatol Surg 2013;39:1745-57.

146. Jan SN, Bashir MM, Khan FA, et al. Unfiltered Nanofat Injections Rejuvenate Postburn Scars of Face. Ann Plast Surg 2019;82:28-33.

147. Klinger M, Marazzi M, Vigo D, et al. Fat Injection for Cases of Severe Burn Outcomes: A New Perspective of Scar Remodeling and Reduction. Aesthetic Plast Surg 2020;44:1278-82.

148. Zhang Q, Liu L, Yong Q, et al. Intralesional injection of adipose-derived stem cells reduces hypertrophic scarring in a rabbit ear model. Stem Cell Res Ther 2015;18:145.

149. Hurst LC, Badalamente MA, Hentz VR, et al. Injectable collagenase clostridium histolyticum for Dupuytren's contracture. N Engl J Med 2009;361:968-79.

150. Sayadi LR, Alhunayan D, Sarantopoulos N, et al. The Molecular Pathogenesis of Dupuytren Disease: Review of the Literature and Suggested New Approaches to Treatment. Ann Plast Surg 2019;83:594-600.

151. Zhang AY, Kargel JS. The Basic Science of Dupuytren Disease. Hand Clin 2018;34:301-305.

152. van Beuge MM, Ten Dam EJ, Werker PM, et al. Matrix and cell phenotype differences in Dupuytren's disease. Fibrogenesis Tissue Repair 2016;9:9.

153. Verhoekx JSN, Beckett KS, Bisson MA, et al. The mechanical environment in Dupuytren's contracture determines cell contractility and associated MMP-mediated matrix remodelling. J Orthop Res 2013;31:328-34.

154. Mella JR, Guo L, Hung V. Dupuytren's Contracture: An Evidence Based Review. Ann Plast Surg 2018;81:S97-101.

155. Peimer CA, Blazar P, Coleman S, et al. Dupuytren contracture recurrence following treatment with collagenase clostridium histolyticum (CORDLESS study): 3-year data. J Hand Surg Am 2013;38:12-22.

156. Traore EJ, Wang W, Yafi FA, et al. Collagenase Clostridium histolyticum in the management of Peyronie's disease: a review of the evidence. Ther Adv Urol 2016;8:192-202.

157. Tsambarlis P, Levine LA. Nonsurgical management of Peyronie's disease. Nat Rev Urol 2019;16:172-186.

158. Xiaflex Highlights of Prescribing Information. US Food and Drug Adminstration Website. Revised June 2018. Accessed September 28 2023.

159. Lam WL, Rawlins JM, Karoo RO, et al. Re-visiting Luck's classification: a histological analysis of Dupuytren's disease. J Hand Surg Eur Vol 2010;35:312-7.

160. Rojkind M, Giambrone MA, Biempica L. Collagen types in normal and cirrhotic liver. Gastroenterology 1979;76:710-9.

161. Vater CA, Harris ED, Jr., Siegel RC. Native cross-links in collagen fibrils induce resistance to human synovial collagenase. Biochem J 1979;181:639-645.

162. Iimuro Y, Nishio T, Morimoto T, et al. Delivery of matrix metalloproteinase-1 attenuates established liver fibrosis in the rat. Gastroenterology 2003;124:445-58.

163. Siller-López F, Sandoval A, Salgado S, et al. Treatment with human metalloproteinase-8 gene delivery ameliorates experimental rat liver cirrhosis. Gastroenterology 2004;126:1122-33; discussion 949.

164. Endo H, Niioka M, Sugioka Y, et al. Matrix metalloproteinase-13 promotes recovery from experimental liver cirrhosis in rats. Pathobiology 2011;78:239-52.

165. Iimuro Y, Brenner DA. Matrix metalloproteinase gene delivery for liver fibrosis. Pharm Res 2008;25:249-58.

166. Jin B, Alter HJ, Zhang ZC, et al. Reversibility of experimental rabbit liver cirrhosis by portal collagenase administration. Lab Invest 2005;85:992-1002.

167. El-Safy S, Tammam SN, Abdel-Halim M, et al. Collagenase loaded chitosan nanoparticles for digestion of the collagenous scar in liver fibrosis: The effect of chitosan intrinsic collagen binding on the success of targeting. Eur J Pharm Biopharm 2020;148:54-66.

168. Nguyen U, Squaglia N, Boge A, et al. The Simple Western™: a gel-free, blot-free, hands-free Western blotting reinvention. Nature Methods 2011;8:v-vi.

169. Popov Y, Sverdlov DY, Sharma AK, et al. Tissue transglutaminase does not affect fibrotic matrix stability or regression of liver fibrosis in mice. Gastroenterology 2011;140:1642-52.

170. Caravan P, Yang Y, Zachariah R, et al. Molecular magnetic resonance imaging of pulmonary fibrosis in mice. Am J Respir Cell Mol Biol 2013;49:1120-6.

171. Farrar CT, Gale EM, Kennan R, et al. CM-101: Type I Collagen-targeted MR Imaging Probe for Detection of Liver Fibrosis. Radiology 2018;287:581-589.

172. Otto GP, Rathkolb B, Oestereicher MA, et al. Clinical Chemistry Reference Intervals for C57BL/6J, C57BL/6N, and C3HeB/FeJ Mice (Mus musculus). J Am Assoc Lab Anim Sci 2016;55:375-86.

173. McVeigh LE, Wijetunga I, Ingram N, et al. Development of orthotopic tumour models using ultrasound-guided intrahepatic injection. Sci Rep 2019;9:9904.

174. Chamberlain J, Yamagami T, Colletti E, et al. Efficient generation of human hepatocytes by the intrahepatic delivery of clonal human mesenchymal stem cells in fetal sheep. Hepatology 2007;46:1935-45.

175. Berraondo P, Crettaz J, Ochoa L, et al. Intrahepatic injection of recombinant adeno-associated virus serotype 2 overcomes gender-related differences in liver transduction. Hum Gene Ther 2006;17:601-10.

176. Wiig H, Keskin D, Kalluri R. Interaction between the extracellular matrix and lymphatics: consequences for lymphangiogenesis and lymphatic function. Matrix Biol 2010;29:645-56.

177. Scallan J, Huxley VH, Korthuis RJ. Integrated Systems Physiology: from Molecule to Function to Disease. Capillary Fluid Exchange: Regulation, Functions, and Pathology. San Rafael (CA): Morgan & Claypool Life Sciences

178. Klein JA. Tumescent technique for regional anesthesia permits lidocaine doses of 35 mg/kg for liposuction. J Dermatol Surg Oncol 1990;16:248-63.

179. Vandooren J, Itoh Y. Alpha-2-Macroglobulin in Inflammation, Immunity and Infections. Front Immunol 2021;12:803244.

180. Werb Z, Burleigh MC, Barrett AJ, et al. The interaction of alpha2-macroglobulin with proteinases. Binding and inhibition of mammalian collagenases and other metal proteinases. Biochem J 1974;139:359-68.

181. Sottrup-Jensen L, Birkedal-Hansen H. Human fibroblast collagenase-alpha-macroglobulin interactions. Localization of cleavage sites in the bait regions of five mammalian alpha-macroglobulins. J Biol Chem 1989;264:393-401.

182. White R, Janoff A, Godfrey HP. Secretion of Alpha-2-macroglobulin by human alveolar macrophages. Lung 1980;158:9-14.

183. Munck Petersen C, Christiansen BS, Heickendorff L, et al. Synthesis and secretion of alpha 2-macroglobulin by human hepatocytes in culture. Eur J Clin Invest 1988;18:543-8.

184. Li Z, Shah DK. Two-pore physiologically based pharmacokinetic model with de novo derived parameters for predicting plasma PK of different size protein therapeutics. J Pharmacokinet Pharmacodyn 2019;46:305-318.

185. Rafidi H, Estevez A, Ferl GZ, et al. Imaging Reveals Importance of Shape and Flexibility for Glomerular Filtration of Biologics. Mol Cancer Ther 2021;20:2008-2015.

186. Ruggiero A, Villa CH, Bander E, et al. Paradoxical glomerular filtration of carbon nanotubes. Proc Natl Acad Sci U S A 2010;107:12369-74.

187. Tabata Y, Kawai T, Murakami Y, et al. Electric Charge Influence of Dextran Derivatives on their Tumor Accumulation After Intravenous Injection. Drug Delivery 1997;4:213-221.

188. Benias PC, Wells RG, Sackey-Aboagye B, et al. Structure and Distribution of an Unrecognized Interstitium in Human Tissues. Sci Rep 2018;8:4947.

189. Fuentes JM, Talamini MA, Fulton WB, et al. General anesthesia delays the inflammatory response and increases survival for mice with endotoxic shock. Clin Vaccine Immunol 2006;13:281-8.

190. Lewis AJ, Seymour CW, Rosengart MR. Current Murine Models of Sepsis. Surg Infect (Larchmt) 2016;17:385-93.

191. Lee HT, Emala CW, Joo JD, et al. Isoflurane improves survival and protects against renal and hepatic injury in murine septic peritonitis. Shock 2007;27:373-9.

192. Koutsogiannaki S, Okuno T, Kobayashi Y, et al. Isoflurane attenuates sepsis-associated lung injury. Biochem Biophys Res Commun 2022;599:127-133.

193. Yin N, Peng Z, Li B, et al. Isoflurane attenuates lipopolysaccharide-induced acute lung injury by inhibiting ROS-mediated NLRP3 inflammasome activation. Am J Transl Res 2016;8:2033-46.

194. Regnault V, Challande P, Pinet F, et al. Cell senescence: basic mechanisms and the need for computational networks in vascular ageing. Cardiovasc Res 2021;117:1841-1858.

195. Nishio T, Iimuro Y, Nitta T, et al. Increased expression of collagenase in the liver induces hepatocyte proliferation with cytoplasmic accumulation of beta-catenin in the rat. J Hepatol 2003;38:468-75.

196. Schuppan D, Schmid M, Somasundaram R, et al. Collagens in the liver extracellular matrix bind hepatocyte growth factor. Gastroenterology 1998;114:139-52.

197. Hansen LK, Wilhelm J, Fassett JT. Regulation of hepatocyte cell cycle progression and differentiation by type I collagen structure. Curr Top Dev Biol 2006;72:205-36.

198. Dupont S, Morsut L, Aragona M, et al. Role of YAP/TAZ in mechanotransduction. Nature 2011;474:179-83.

199. Liu F, Lagares D, Choi KM, et al. Mechanosignaling through YAP and TAZ drives fibroblast activation and fibrosis. Am J Physiol Lung Cell Mol Physiol 2015;308:L344-57.

200. Pibiri M, Simbula G. Role of the Hippo pathway in liver regeneration and repair: recent advances. Inflamm Regen 2022;42:59.

201. Liu Y, Lu T, Zhang C, et al. Activation of YAP attenuates hepatic damage and fibrosis in liver ischemia-reperfusion injury. J Hepatol 2019;71:719-730.

202. Lu L, Finegold MJ, Johnson RL. Hippo pathway coactivators Yap and Taz are required to coordinate mammalian liver regeneration. Exp Mol Med 2018;50:e423.

203. Duffield JS, Forbes SJ, Constandinou CM, et al. Selective depletion of macrophages reveals distinct, opposing roles during liver injury and repair. J Clin Invest 2005;115:56-65.

204. Patsenker E, Popov Y, Stickel F, et al. Pharmacological inhibition of integrin alphavbeta3 aggravates experimental liver fibrosis and suppresses hepatic angiogenesis. Hepatology 2009;50:1501-11.

205. Popov Y, Sverdlov DY, Bhaskar KR, et al. Macrophage-mediated phagocytosis of apoptotic cholangiocytes contributes to reversal of experimental biliary fibrosis. Am J Physiol Gastrointest Liver Physiol 2010;298:G323-34.

206. Li JL, Li G, Jing XZ, et al. Assessment of clinical sepsis-associated biomarkers in a septic mouse model. J Int Med Res 2018;46:2410-2422.

207. Lee SM, An WS. New clinical criteria for septic shock: serum lactate level as new emerging vital sign. J Thorac Dis 2016;8:1388-90.

208. Zhai X, Yang Z, Zheng G, et al. Lactate as a Potential Biomarker of Sepsis in a Rat Cecal Ligation and Puncture Model. Mediators Inflamm 2018;2018:8352727.

209. Georges PC, Hui JJ, Gombos Z, et al. Increased stiffness of the rat liver precedes matrix deposition: implications for fibrosis. Am J Physiol Gastrointest Liver Physiol 2007;293:G1147-54.

210. Steg PG, Rongione AJ, Gal D, et al. Pulsed ultraviolet laser irradiation produces endothelium-independent relaxation of vascular smooth muscle. Circulation 1989;80:189-97.

211. Teramura A, Macfarlane R, Owen CJ, et al. Application of the 1-microsecond pulsed-dye laser to the treatment of experimental cerebral vasospasm. J Neurosurg 1991;75:271-6.

212. Schwengel RH, Gregory KW, Hearne SE, et al. Characterization of pulsed-dye laser-mediated vasodilatation in a rabbit femoral artery model of vasoconstriction. Lasers Surg Med 1993;13:284-95.

213. Kaoutzanis MC, Peterson JW, Anderson RR, et al. Basic mechanism of in vitro pulsed-dye laser-induced vasodilation. J Neurosurg 1995;82:256-61.

214. Thiel M. Application of shock waves in medicine. Clin Orthop Relat Res 2001:18-21.

215. Ito K, Fukumoto Y, Shimokawa H. Extracorporeal shock wave therapy as a new and non-invasive angiogenic strategy. Tohoku J Exp Med 2009;219:1-9.

216. Schuh CM, Heher P, Weihs AM, et al. In vitro extracorporeal shock wave treatment enhances stemness and preserves multipotency of rat and human adipose-derived stem cells. Cytotherapy 2014;16:1666-78.

217. Priglinger E, Schuh C, Steffenhagen C, et al. Improvement of adipose tissue-derived cells by low-energy extracorporeal shock wave therapy. Cytotherapy 2017;19:1079-1095.

218. Davis TA, Stojadinovic A, Anam K, et al. Extracorporeal shock wave therapy suppresses the early proinflammatory immune response to a severe cutaneous burn injury. Int Wound J 2009;6:11-21.

219. Ujiie N, Nakano T, Yamada M, et al. Low-energy extracorporeal shock wave therapy for a model of liver cirrhosis ameliorates liver fibrosis and liver function. Sci Rep 2020;10:2405.

220. Ito K, Fukumoto Y, Shimokawa H. Extracorporeal shock wave therapy for ischemic cardiovascular disorders. Am J Cardiovasc Drugs 2011;11:295-302.

221. Abe Y, Ito K, Hao K, et al. Extracorporeal low-energy shock-wave therapy exerts anti-inflammatory effects in a rat model of acute myocardial infarction. Circ J 2014;78:2915-25.

222. Tanzi EL, Capelli CC, Robertson DW, et al. Improvement in the appearance of cellulite and skin laxity resulting from a single treatment with acoustic subcision: Findings from a multicenter pivotal clinical trial. Lasers Surg Med 2022;54:121-128.

223. Biesman BS, Capelli CC. Comparing safety and efficacy of acoustic subcision at two different rapid acoustic pulse rates to improve the appearance of cellulite. Lasers Surg Med 2023.

224. LaTowsky B, Robertson DW, Capelli CC. Long-term improvement in the appearance of hypertrophic scars following a single treatment with acoustic subcision-A single center proof-of-concept study. Lasers Surg Med 2022;54:1251-1260.

225. Sadasivan SK, Siddaraju N, Khan KM, et al. Developing an in vitro screening assay platform for evaluation of antifibrotic drugs using precision-cut liver slices. Fibrogenesis Tissue Repair 2015;8:1.

226. van de Bovenkamp M, Groothuis GM, Meijer DK, et al. Liver slices as a model to study fibrogenesis and test the effects of anti-fibrotic drugs on fibrogenic cells in human liver. Toxicol In Vitro 2008;22:771-8.

227. Guo Y, Wu XQ, Zhang C, et al. Protective effect of sodium ferulate on acetaldehyde-treated precision-cut rat liver slices. J Med Food 2012;15:557-62.

228. Westra IM, Oosterhuis D, Groothuis GM, et al. Precision-cut liver slices as a model for the early onset of liver fibrosis to test antifibrotic drugs. Toxicol Appl Pharmacol 2014;274:328-38.

229. Coombes JD, Choi SS, Swiderska-Syn M, et al. Osteopontin is a proximal effector of leptin-mediated non-alcoholic steatohepatitis (NASH) fibrosis. Biochim Biophys Acta 2016;1862:135-44.

230. De Chiara F, Thomsen KL, Habtesion A, et al. Ammonia Scavenging Prevents Progression of Fibrosis in Experimental Nonalcoholic Fatty Liver Disease. Hepatology 2020;71:874-892.

231. Wang K, Lin B, Brems JJ, et al. Hepatic apoptosis can modulate liver fibrosis through TIMP1 pathway. Apoptosis 2013;18:566-77.

232. Luangmonkong T, Suriguga S, Adhyatmika A, et al. In vitro and ex vivo anti-fibrotic effects of LY2109761, a small molecule inhibitor against TGF-β. Toxicol Appl Pharmacol 2018;355:127-137.

233. Barcena-Varela M, Paish H, Alvarez L, et al. Epigenetic mechanisms and metabolic reprogramming in fibrogenesis: dual targeting of G9a and DNMT1 for the inhibition of liver fibrosis. Gut 2021;70:388-400.

234. Gore E, Bigaeva E, Oldenburger A, et al. PI3K inhibition reduces murine and human liver fibrogenesis in precision-cut liver slices. Biochem Pharmacol 2019;169:113633.

235. Starokozhko V, Abza GB, Maessen HC, et al. Viability, function and morphological integrity of precision-cut liver slices during prolonged incubation: Effects of culture medium. Toxicol In Vitro 2015;30:288-99.

236. Bigaeva E, Gore E, Simon E, et al. Transcriptomic characterization of culture-associated changes in murine and human precision-cut tissue slices. Arch Toxicol 2019;93:3549-3583.

237. Westra IM, Mutsaers HA, Luangmonkong T, et al. Human precision-cut liver slices as a model to test antifibrotic drugs in the early onset of liver fibrosis. Toxicol In Vitro 2016;35:77-85.

238. Bigaeva E, Gore E, Mutsaers HAM, et al. Exploring organ-specific features of fibrogenesis using murine precision-cut tissue slices. Biochim Biophys Acta Mol Basis Dis 2020;1866:165582.

239. Stefanovic B, Manojlovic Z, Vied C, et al. Discovery and evaluation of inhibitor of LARP6 as specific antifibrotic compound. Sci Rep 2019;9:326.

240. Vilaseca M, García-Calderó H, Lafoz E, et al. Mitochondria-targeted antioxidant mitoquinone deactivates human and rat hepatic stellate cells and reduces portal hypertension in cirrhotic rats. Liver Int 2017;37:1002-1012.

241. Hinz B, Gabbiani G. Mechanisms of force generation and transmission by myofibroblasts. Curr Opin Biotechnol 2003;14:538-46.

242. Li Z, Dranoff JA, Chan EP, et al. Transforming growth factor-beta and substrate stiffness regulate portal fibroblast activation in culture. Hepatology 2007;46:1246-56.

243. Arora PD, Narani N, McCulloch CA. The compliance of collagen gels regulates transforming growth factor-beta induction of alpha-smooth muscle actin in fibroblasts. Am J Pathol 1999;154:871-82.

244. Guo Y, Wang H, Zhang C. Establishment of rat precision-cut fibrotic liver slice technique and its application in verapamil metabolism. Clin Exp Pharmacol Physiol 2007;34:406-13.

245. Wu X, Roberto JB, Knupp A, et al. Response of Human Liver Tissue to Innate Immune Stimuli. Front Immunol 2022;13:811551.

246. Gore E, Bigaeva E, Oldenburger A, et al. Investigating fibrosis and inflammation in an ex vivo NASH murine model. Am J Physiol Gastrointest Liver Physiol 2020;318:G336-g351.

247. Westra IM, Oosterhuis D, Groothuis GM, et al. The effect of antifibrotic drugs in rat precision-cut fibrotic liver slices. PLoS One 2014;9:e95462.

248. van de Bovenkamp M, Groothuis GM, Meijer DK, et al. Precision-cut fibrotic rat liver slices as a new model to test the effects of anti-fibrotic drugs in vitro. J Hepatol 2006;45:696-703.

249. Huang X, Cai H, Ammar R, et al. Molecular characterization of a precision-cut rat liver slice model for the evaluation of antifibrotic compounds. Am J Physiol Gastrointest Liver Physiol 2019;316:G15-g24.

250. Hagens WI, Olinga P, Meijer DK, et al. Gliotoxin non-selectively induces apoptosis in fibrotic and normal livers. Liver Int 2006;26:232-9.

251. Gonzalo T, Beljaars L, van de Bovenkamp M, et al. Local inhibition of liver fibrosis by specific delivery of a platelet-derived growth factor kinase inhibitor to hepatic stellate cells. J Pharmacol Exp Ther 2007;321:856-65.

252. Oldenburger A, Birk G, Schlepütz M, et al. Modulation of vascular contraction via soluble guanylate cyclase signaling in a novel ex vivo method using rat precision-cut liver slices. Pharmacol Res Perspect 2021;9:e00768.

253. Paish HL, Reed LH, Brown H, et al. A Bioreactor Technology for Modeling Fibrosis in Human and Rodent Precision-Cut Liver Slices. Hepatology 2019;70:1377-1391.

254. Howard D, Sturtevant B. In vitro study of the mechanical effects of shock-wave lithotripsy. Ultrasound Med Biol 1997;23:1107-22.

255. Lokhandwalla M, Sturtevant B. Mechanical haemolysis in shock wave lithotripsy (SWL): I. Analysis of cell deformation due to SWL flow-fields. Physics in Medicine & Biology 2001;46:413.

256. Lokhandwalla M, McAteer JA, Williams Jr JC, et al. Mechanical haemolysis in shock wave lithotripsy (SWL): II. In vitro cell lysis due to shear. Physics in Medicine & Biology 2001;46:1245.

257. Freund JB, Colonius T, Evan AP. A cumulative shear mechanism for tissue damage initiation in shock-wave lithotripsy. Ultrasound Med Biol 2007;33:1495-503.

258. Ziros PG, Chartoumpekis DV, Sykiotis GP. A Simple Protocol for High Efficiency Protein Isolation After RNA Isolation from Mouse Thyroid and Other Very Small Tissue Samples. Methods Mol Biol 2016;1449:383-93.

259. Andersen CL, Jensen JL, Ørntoft TF. Normalization of real-time quantitative reverse transcription-PCR data: a model-based variance estimation approach to identify genes suited for normalization, applied to bladder and colon cancer data sets. Cancer Res 2004;64:5245-50.

260. Boehm O, Zur B, Koch A, et al. Clinical chemistry reference database for Wistar rats and C57/BL6 mice. Biol Chem 2007;388:547-54.

261. Giannini EG, Testa R, Savarino V. Liver enzyme alteration: a guide for clinicians. Cmaj 2005;172:367-79.

262. You J, Park SA, Shin DS, et al. Characterizing the effects of heparin gel stiffness on function of primary hepatocytes. Tissue Eng Part A 2013;19:2655-63.

263. Xia T, Zhao R, Feng F, et al. The Effect of Matrix Stiffness on Human Hepatocyte Migration and Function-An In Vitro Research. Polymers (Basel) 2020;12.

264. Elaut G, Henkens T, Papeleu P, et al. Molecular mechanisms underlying the dedifferentiation process of isolated hepatocytes and their cultures. Curr Drug Metab 2006;7:629-60.

265. Heslop JA, Rowe C, Walsh J, et al. Mechanistic evaluation of primary human hepatocyte culture using global proteomic analysis reveals a selective dedifferentiation profile. Arch Toxicol 2017;91:439-452.

266. Kiamehr M, Heiskanen L, Laufer T, et al. Dedifferentiation of Primary Hepatocytes is Accompanied with Reorganization of Lipid Metabolism Indicated by Altered Molecular Lipid and miRNA Profiles. Int J Mol Sci 2019;20.

267. Irvine KM, Skoien R, Bokil NJ, et al. Senescent human hepatocytes express a unique secretory phenotype and promote macrophage migration. World J Gastroenterol 2014;20:17851-62.

268. Cieslak KP, Baur O, Verheij J, et al. Liver function declines with increased age. HPB (Oxford) 2016;18:691-6.

269. Bonnet L, Alexandersson I, Baboota RK, et al. Cellular senescence in hepatocytes contributes to metabolic disturbances in NASH. Front Endocrinol (Lausanne) 2022;13:957616.

270. Mouta Carreira C, Nasser SM, di Tomaso E, et al. LYVE-1 is not restricted to the lymph vessels: expression in normal liver blood sinusoids and down-regulation in human liver cancer and cirrhosis. Cancer Res 2001;61:8079-84.

271. Arimoto J, Ikura Y, Suekane T, et al. Expression of LYVE-1 in sinusoidal endothelium is reduced in chronically inflamed human livers. J Gastroenterol 2010;45:317-25.

272. Unger C, Lokmer N, Lehmann D, et al. Detection of phenol contamination in RNA samples and its impact on qRT-PCR results. Anal Biochem 2019;571:49-52.

273. Bao YL, Wang L, Pan HT, et al. Animal and Organoid Models of Liver Fibrosis. Front Physiol 2021;12:666138.

274. Ma Y, Hu L, Tang J, et al. Three-Dimensional Cell Co-Culture Liver Models and Their Applications in Pharmaceutical Research. Int J Mol Sci 2023;24.

275. Godoy P, Hewitt NJ, Albrecht U, et al. Recent advances in 2D and 3D in vitro systems using primary hepatocytes, alternative hepatocyte sources and non-parenchymal liver cells and their use in investigating mechanisms of hepatotoxicity, cell signaling and ADME. Arch Toxicol 2013;87:1315-530.

276. Bedossa P, Poynard T. An algorithm for the grading of activity in chronic hepatitis C. The METAVIR Cooperative Study Group. Hepatology 1996;24:289-93.

277. Kutami R, Girgrah N, Wanless IR, et al. The Laennec grading system for assessment of hepatic fibrosis Validation by correlation with wedged hepatic vein pressure and clinical features. Hepatology 2000;32:407.

278. Krawczyk M, Ligocka J, Ligocki M, et al. Does transient elastography correlate with liver fibrosis in patients with PSC? Laennec score-based analysis of explanted livers. Scand J Gastroenterol 2017;52:1407-1412.

279. Kim SU, Oh HJ, Wanless IR, et al. The Laennec staging system for histological sub-classification of cirrhosis is useful for stratification of prognosis in patients with liver cirrhosis. J Hepatol 2012;57:556-63.

280. Kim MY, Cho MY, Baik SK, et al. Histological subclassification of cirrhosis using the Laennec fibrosis scoring system correlates with clinical stage and grade of portal hypertension. J Hepatol 2011;55:1004-9.

281. Nagula S, Jain D, Groszmann RJ, et al. Histological-hemodynamic correlation in cirrhosis-a histological classification of the severity of cirrhosis. J Hepatol 2006;44:111-7.

282. Iwakiri Y. Pathophysiology of portal hypertension. Clin Liver Dis 2014;18:281-91.

283. Berzigotti A, Seijo S, Reverter E, et al. Assessing portal hypertension in liver diseases. Expert Review of Gastroenterology & Hepatology 2013;7:141-155.

284. Nielsen K, Clemmesen JO, Vassiliadis E, et al. Liver collagen in cirrhosis correlates with portal hypertension and liver dysfunction. Apmis 2014;122:1213-22.

285. Wells RG. The role of matrix stiffness in regulating cell behavior. Hepatology 2008;47:1394-400.

286. Zhao YQ, Deng XW, Xu GQ, et al. Mechanical homeostasis imbalance in hepatic stellate cells activation and hepatic fibrosis. Front Mol Biosci 2023;10:1183808.

287. Cabral-Pacheco GA, Garza-Veloz I, Castruita-De la Rosa C, et al. The Roles of Matrix Metalloproteinases and Their Inhibitors in Human Diseases. Int J Mol Sci 2020;21.

288. Chen W, Yang A, Jia J, et al. Lysyl Oxidase (LOX) Family Members: Rationale and Their Potential as Therapeutic Targets for Liver Fibrosis. Hepatology 2020;72:729-741.

289. Klinkhammer BM, Floege J, Boor P. PDGF in organ fibrosis. Mol Aspects Med 2018;62:44-62.

290. Larsen M, Artym VV, Green JA, et al. The matrix reorganized: extracellular matrix remodeling and integrin signaling. Curr Opin Cell Biol 2006;18:463-71.

291. Song EK, Jeon J, Jang DG, et al. ITGBL1 modulates integrin activity to promote cartilage formation and protect against arthritis. Sci Transl Med 2018;10.

292. Blackburn PR, Xu Z, Tumelty KE, et al. Bi-allelic Alterations in AEBP1 Lead to Defective Collagen Assembly and Connective Tissue Structure Resulting in a Variant of Ehlers-Danlos Syndrome. Am J Hum Genet 2018;102:696-705.

293. Gerarduzzi C, Kumar RK, Trivedi P, et al. Silencing SMOC2 ameliorates kidney fibrosis by inhibiting fibroblast to myofibroblast transformation. JCI Insight 2017;2.

294. Li X, Zhao D, Guo Z, et al. Overexpression of SerpinE2/protease nexin-1 Contribute to Pathological Cardiac Fibrosis via increasing Collagen Deposition. Sci Rep 2016;6:37635.

295. Sullivan MM, Barker TH, Funk SE, et al. Matricellular hevin regulates decorin production and collagen assembly. J Biol Chem 2006;281:27621-32.

296. Yanagisawa H, Schluterman MK, Brekken RA. Fibulin-5, an integrin-binding matricellular protein: its function in development and disease. J Cell Commun Signal 2009;3:337-47.

297. McIver CM, Lloyd JM, Hewett PJ, et al. Dipeptidase 1: a candidate tumor-specific molecular marker in colorectal carcinoma. Cancer Lett 2004;209:67-74.

298. Toiyama Y, Inoue Y, Yasuda H, et al. DPEP1, expressed in the early stages of colon carcinogenesis, affects cancer cell invasiveness. J Gastroenterol 2011;46:153-63.

299. Engelholm LH, Ingvarsen S, Jürgensen HJ, et al. The collagen receptor uPARAP/Endo180. Front Biosci (Landmark Ed) 2009;14:2103-14.

300. López-Guisa JM, Cai X, Collins SJ, et al. Mannose receptor 2 attenuates renal fibrosis. J Am Soc Nephrol 2012;23:236-51.

301. Jiang XJ, Lin J, Cai QH, et al. CDH17 alters MMP-2 expression via canonical NF-κB signalling in human gastric cancer. Gene 2019;682:92-100.

302. Le Goff C, Morice-Picard F, Dagoneau N, et al. ADAMTSL2 mutations in geleophysic dysplasia demonstrate a role for ADAMTS-like proteins in TGF-beta bioavailability regulation. Nat Genet 2008;40:1119-23.

303. Rypdal KB, Erusappan PM, Melleby AO, et al. The extracellular matrix glycoprotein ADAMTSL2 is increased in heart failure and inhibits TGFβ signalling in cardiac fibroblasts. Sci Rep 2021;11:19757.

304. Novikova EG, Reznik SE, Varlamov O, et al. Carboxypeptidase Z is present in the regulated secretory pathway and extracellular matrix in cultured cells and in human tissues. J Biol Chem 2000;275:4865-70.

305. Akama T, Chun TH. Transcription factor 21 (TCF21) promotes proinflammatory interleukin 6 expression and extracellular matrix remodeling in visceral adipose stem cells. J Biol Chem 2018;293:6603-6610.

306. Nulali J, Zhan M, Zhang K, et al. Osteoglycin: An ECM Factor Regulating Fibrosis and Tumorigenesis. Biomolecules 2022;12.

307. Murshed M, Schinke T, McKee MD, et al. Extracellular matrix mineralization is regulated locally; different roles of two gla-containing proteins. J Cell Biol 2004;165:625-30.

308. Yan Z, Cheng X, Wang T, et al. Therapeutic potential for targeting Annexin A1 in fibrotic diseases. Genes Dis 2022;9:1493-1505.

309. Nair RR, Solway J, Boyd DD. Expression cloning identifies transgelin (SM22) as a novel repressor of 92-kDa type IV collagenase (MMP-9) expression. J Biol Chem 2006;281:26424-36.

310. Yu H, Königshoff M, Jayachandran A, et al. Transgelin is a direct target of TGF-beta/Smad3-dependent epithelial cell migration in lung fibrosis. Faseb j 2008;22:1778-89.

311. Xu R, Harrison PM, Chen M, et al. Cytoglobin overexpression protects against damage-induced fibrosis. Mol Ther 2006;13:1093-100.

312. Li X, Fang Y, Jiang D, et al. Targeting FSTL1 for Multiple Fibrotic and Systemic Autoimmune Diseases. Mol Ther 2021;29:347-364.

313. Tang Y, Hong F, Ding S, et al. METTL3-mediated m(6)A modification of IGFBP7-OT promotes osteoarthritis progression by regulating the DNMT1/DNMT3a-IGFBP7 axis. Cell Rep 2023;42:112589.

314. Westermann D, Mersmann J, Melchior A, et al. Biglycan is required for adaptive remodeling after myocardial infarction. Circulation 2008;117:1269-76.

315. Kisseleva T, Cong M, Paik Y, et al. Myofibroblasts revert to an inactive phenotype during regression of liver fibrosis. Proc Natl Acad Sci U S A 2012;109:9448-53.

316. Chakraborty JB, Oakley F, Walsh MJ. Mechanisms and Biomarkers of Apoptosis in Liver Disease and Fibrosis. International Journal of Hepatology 2012;2012:648915.

317. Shan L, Wang F, Zhai D, et al. New Drugs for Hepatic Fibrosis. Front Pharmacol 2022;13:874408.

318. Ratziu V, Harrison SA, Francque S, et al. Elafibranor, an Agonist of the Peroxisome Proliferator-Activated Receptor-α and -δ, Induces Resolution of Nonalcoholic Steatohepatitis Without Fibrosis Worsening. Gastroenterology 2016;150:1147-1159.e5.

319. Moroni F, Dwyer BJ, Graham C, et al. Safety profile of autologous macrophage therapy for liver cirrhosis. Nat Med 2019;25:1560-1565.